MICROSTRUCTURAL EVOLUTION AND RADIATION EFFECTS OF

URANIUM-BEARING DIFFUSION COUPLES

A Dissertation

by

CHAO-CHEN WEI

Submitted to the Office of Graduate and Professional Studies of
Texas A&M University
in partial fulfillment of the requirements for the degree of

DOCTOR OF PHILOSOPHY

Chair of Committee,	Lin Shao
Committee Members,	Karl Hartwig
	Yassin Hassan
	Haiyan Wang
Head of Department,	Ibrahim Karaman

December 2014

Major Subject: Materials Science and Engineering

ABSTRACT

Metallic nuclear fuels, as potential candidates in advanced reactors development, have been extensively studied for over five decades. The main challenges are the fuel performance designed for higher burn-up and higher temperatures. Fuel-cladding chemical interaction, or FCCI, is one of the primary material problems during reactor operations. A series of tests using uranium-bearing fuel alloys and various cladding materials were performed to assess the diffusional interactions. However, the knowledge of thermally-activated multicomponent diffusion followed by irradiation tests is quite limited. , Combined both experimental and theoretical investigation are essential to predict the feasibility of fuel designs. The overall objective of this dissertation is to unravel the radiation effects in microstructural and kinetic data. In order to achieve this, two major diffusion systems are chosen.

For the first system, we start with two uranium-free diffusion couples to study microstructural evolution. Primary experiments assembled zirconium/molybdenum with iron. Zr and Mo are the major constituents in fuel alloys and Fe is the surrogate for ferritic cladding materials. Both diffusion couples were annealed at 850°C for 15 days and irradiated with 3.5MeV Fe^{++} at 600°C. Post irradiation examination involved scanning electron microscope (SEM) and transmission electron microscope (TEM). Through this work, we identified the phases formed in the interaction layers and showed enhanced diffusion in the ion bombarded regions. Additionally, the mechanism of intermetallics formation (e.g. Fe$_{23}$Zr$_6$) and radiation stability were discussed.

Second, a matrix of uranium-bearing couples is established. 1) Depleted uranium (DU) was bonded with polycrystalliine iron to form binary diffusion couples followed

by 2 MeV He$^+$ irradiation. Our intent is to understand microstructural information and thermokinetic data. 2) DU vs. single crystalline iron/nickel couples were assembled and annealed for various temperatures/time. Interdiffusion coefficients and activation energy are calculated for each phase formed in the interaction layers 3) In addition to solid-solid diffusion experiments, Fe/(Fe+Cr)/(Fe+Cr+Ni) were deposited on the DU substrates to form thin-film diffusion couples with concurrent 3.5MeV Fe^{++} ion irradiation. Rutherford backscattering spectrometry (RBS) was used to extrapolate interdiffusion profiles and intermetallic phase formation. These results provide strong evidence to support multiscale modeling of FCCI. In particular, goals of the modeling are to provide detailed analysis in fuel performance development.

DEDICATION

To my family and my wife, thank you for your endless encouragement.

ACKNOWLEDGEMENTS

I would like to acknowledge Dr. Shao for his guidance and support through my research life. Every time when I am lost, he helps me get back on track. When I am in doubt, he sheds the light for me. He is always there for me when I have to travel back for my ill mom. Words cannot express how I am grateful to be his student. I rally appreciate all of his help.

I would like thank my committee members, Dr. Hartwig, Dr. Hassan and Dr. Wang for their precious advice and support with lab resource.

I would also like to thank my group members and colleagues, Dr. Myers, Dr. Martin, Dr. Aitkaliveya, Dr. Luo, Dr. Lee, D. Chen, T. Chen, J. Wang, X. Wang, J. Wallace, and M. J. General for their help throughout the dissertation.

NOMENCLATURE

AFCI   Advanced Fuel Cycle Initiative

ANL   Argonne National Laboratory

BF   Bright Filed

BSE   Backscattered Electron

CBED   Convergent Beam Electron Diffraction

CCD   Charge-coupled Device

CVD   Chemical Vapor Depostion

DF   Dark Field

dpa   Displacement Per Atom

DU   Depleted Uranium

EBR   Experimental Breeder Reactor

EDS   Energy Dispersive X-ray Spectroscopy

EPMA   Electron Probe Microanalysis

FCC   Face Centered Cubic

FCCI   Fuel Cladding Chemical Interaction

FCRD   Fuel Cycle Research and Development

FIB   Focused Ion Beam

FMD   Freely Migrating Defects

FMS   Farretic/Martensitic Steel

GB   Grain Boundaries

GNEP   Global Nuclear Energy Partnership

HAADF	High-angle Annular Dark-field
IFR	Integral Fast Reactor
INL	Idaho National Laboratory
iQC	Icosahedral Quasicrystal
keV	Kilo Electron Volt
LMR	Liquid Metal Reactor
MeV	Mega Electron Volt
NRT	Norgett-Robinson-Torrens
PKA	Primary Knock-on Atom
PVD	Physical Vapor Deposition
RBS	Rutherford Backscattering Spectrometry
RED	Radiation Enhanced Diffusion
RERTR	Reduced Enrichment for Research and Test Reactors
RP	Projected Range
SAD	Selected Area Diffraction
SE	Secondary Electron
SEM	Scanning Electron Microscope
STEM	Scanning Trasmission Electron Microscope
TEM	Transmission Electron Microscope

TABLE OF CONTENTS

LIST OF FIGURES

LIST OF TABLES

1. INTRODUCTION

Fuel cladding chemical interaction, or FCCI, has a huge impact on fuel designs and cladding considerations. The advanced metallic fuel of fast reactors are developed for higher temperature and higher burnup. During reactor operation, energetic neutrons and fission products cause significant damage to both fuel itself and cladding materials. Strong interest exists for understanding radiation effects and interdiffusion mechanism. It is, however, difficult for long irradiation testing to achieve expected burnup level.

Various diffusion experiments have been tested earlier consisting uranium-plutonium alloys and cladding materials, the efforts contained in this dissertation focus on selected couples for intermetallic phase formation and diffusion kinetics data. The basic layout of this dissertation starts with a brief background on metallic fuel development and radiation effects (Section 2), a section on the experimental and characterization methods (Section 3), followed by two sections which discussed main diffusion couple (Section 4 and 5) systems performed. Sections 4 and 5 begin with objectives and research activities.

1.1 Dissertation scope

The aim of this dissertation is to provide experimental data and support computational modeling for FCCI and further fuel performance. In order to address FCCI, selected diffusion systems were annealed at elevated temperatures followed by ion irradiation. Scanning electron microscope (SEM) and transmission electron microscope (TEM) are employed for all solid-solid diffusion systems and Rutherford backscattering spectrometry (RBS) with high fidelity spectral simulations were used for all thin-film diffusion couples.

1

The two main objectives covered in this dissertation are :

1. The intermetallics formation plays a huge role in developing fuel alloys. With the help of multicomponent diffusion couples, thermokinetic data and microstructural information for binary, or ternary systems can be obtained. Therefore, interdiffusion coefficients and activation energies of each phase provide fundamental parameters to support the multiscale modeling of FCCI.

2. In the effort to understand radiation effects of FCCI during reactor operation, thermally-activated diffusion couples were irradiated with charged particles to expected damage level. Post-irradiation examination was performed to investigate the phase stability and related microstrual changes.

In addition, a very brief introduction of the two selected diffusion systems were provided in the following sub-sections. For clarity, the uranium-bearing system are presented separately, involving bulk and thin-film diffusion couples.

1.1.1   Uranium-free diffusion systems

The interaction between fuel alloys and cladding materials strongly depend on the composition. Consequently, fragile interfacial compounds with relatively low melting temperature are formed. The addition of zirconium and molybdenum have been proved to increase the high temperature stability. In order to study the possible phase formed in the reaction zone, ex-reactor experiments were performed at elevated temperature. Zr and Mo were assembled with iron, as the surrogate to ferrous cladding materials.

Despite numerous earlier studies, the intermetallics of Fe/Zr and Fe/Mo systems are not completely understood. Section 4 is dedicated to phase identification and microstructural changes after heavy ion irradiation.

1.1.2 Uranium-bearing diffusion systems

In this section, the uranium-based experiments are divided into two groups including 1) solid-solid diffusion couples and 2) thin-film diffusion couples. The objectives are to understand the diffusivities of each phase and properties with different alloy elements. Iron and nickel, major constituent in cladding materials, were bonded with depleted uranium to form binary diffusion couples followed by He ion irradiation.

However, relatively rough interaction zones are usually observed in uranium-bearing couples due to oxidation. The oxide layers result in delayed interdiffusion and large interface variations. In the present work, a setup of thin-film diffusion couples,involving iron, chromium and nickel, is constructed. Fe/(Fe+Cr)/(Fe+Cr+Ni) were deposited onto depleted uranium substrate followed by heave ion irradiation. Rutherford backscattering spectrometry (RBS) was performed to investigate interdiffusion profiles.

2.   BACKGROUND ON METALLIC FUEL DEVELOPMENT AND RADIATION EFFECTS

The present section summarizes the experience with earlier metallic fuel development, including fuel design and fuel performance. In addition, a brief overview is dedicated to the radiation effects during reactor operation. However, this area is very broad and covers a wide range of practical issues. Only the fundamentals which is necessary to the data interpretation in this dissertation will be discussed .

2.1   Overview of metallic fuel development

Metallic alloy fuels have been first developed and tested in the liquid metal reactors (LMR) since 1960s[54, 55, 116, 73]. Variety of uranium-based alloys were cast and used as driver fuels in Experimental Breeder Reactor-II (EBR-II), a test facility at Argonne National Laboratory-West in Idaho falls, Idaho. The results were unsuccessful with peak burnup of ~ 3 at% and failed due to cladding breach. At that time, strong interest turned and concentrated on ceramic fuels development before the potential of metallic fuels been fully recognized[5, 4].

Through the 1970s, however, the EBR-II continued using selected metallic fuels along with possible cladding materials and appreciable burnup were achieved. Efforts were focused on fuels composition and stronger cladding, including $\sim 35,000$ fuel pins test experiments[123, 120, 100, 84, 97, 131]. Uranium-fissium (U-5 wt% Fs) fuels was cast in the early 1970s, as known as Mark-IA. It had 85% smeared density and contained a small gas plenum. MK-II came out with improved smeared density 75% and better plenum-to fuel ratio. Figure 2.1 shows the evolution trends in burnup limit of EBR-II driver fuels[71, 8, 9, 10].

4
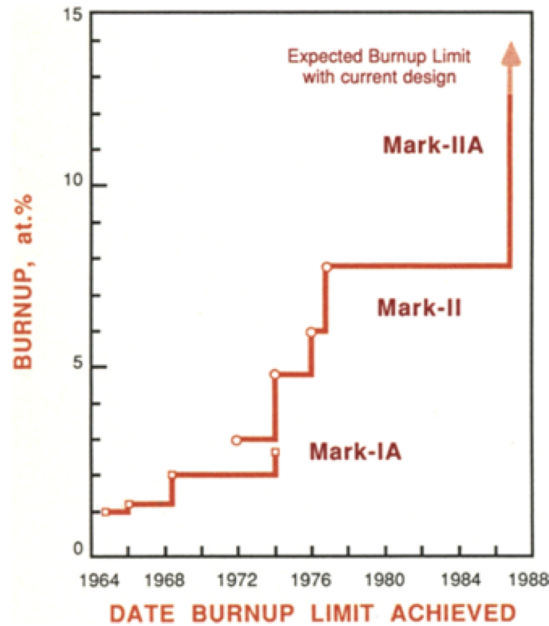
Figure 2.1: The evolution of burnup limit in EBR-II driver fuels.

US Integral Fast Reactor (IFR) program initiated in 1983, after extensive experience from the late 1960s and targeted to higher burnup capability. Argonne National Laboratory (ANL) proposed to use U-Pu-Zr alloys as driver fuels in EBR-II, clad with austenitic stainless steels (D9 or HT9) and modified smeared density of 75%, replacing the MK-IIA fuel design. For the test of U-Pu-Zr alloy cladding with D9, the burnup level reached 18.4 at%; and 17.5 at% was achieved with HT9 steels without cladding breach[139, 130, 112]. The basic schematic of fuel pin components is shown in Figure 2.2. Upon prior works, efforts were mainly made on modifying the space between fuel alloys and cladding materials, which allows excessive swelling before contact initiated[56, 39, 140].
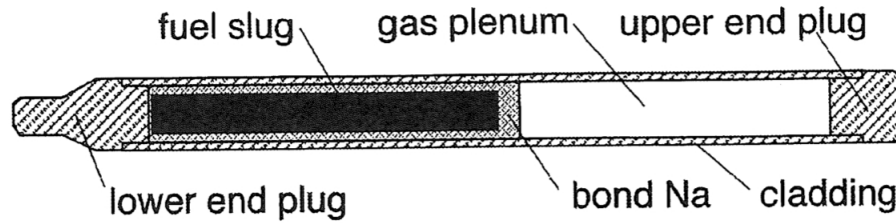
Figure 2.2: The schematic view of metallic fuel pin.

Among several advantages, such as good thermal conductivity, excellent neutron economy, simple reprocessing, and improved waste management, of metallic fuels , the Idaho National Laboratory (INL)and ANL share collaborative efforts in developing ultra-high burnup fuel alloys[132, 91, 92, 67]. As part of the Global Nuclear Energy Partnership (GNEP) program, the goal is to achieve 40 at%. burnup[114, 107, 7, 17, 3, 30, 136, 102, 96]. However, damage accumulation from energetic neutrons and fission gas will cause significant dimensional changes. The radiation effects will be discussed in the following section.

2.2   Radiation effects

During reactor operation, high energy neutrons and fission products will cause severe damage to the microstructures. The incident particle will collide and transfer energy to a lattice atom, called primary knock-on atom (PKA). The PKA will continue traveling and cause a series of atomic displacements. Figure 2.3 illustrates the atomic displacements of neutron collisions. Along the PKA trajectory, damage cascade is created and a vacancy rich core structures surrounded by interstitials is usually formed. Finally, the PKA will slow down via electronic and nuclear stopping without enough energy to create further displacement. The whole annihilation

6

process is around 10 picosecond.
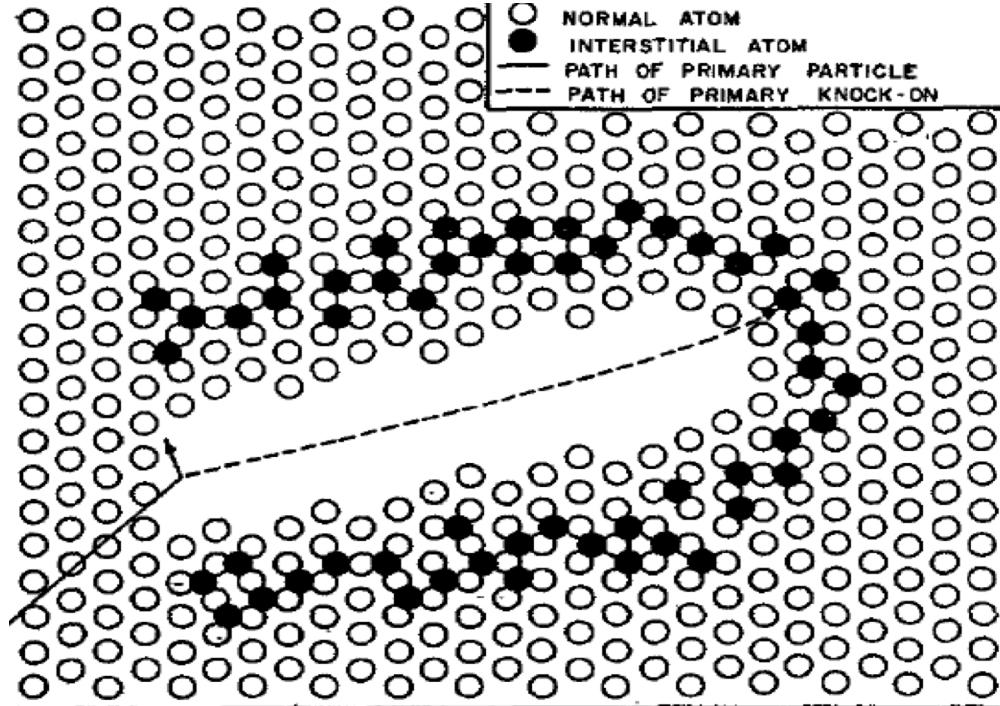
Figure 2.3: Damage cascade of neutron collisions.

According to Norgett-Robinson-Torrens (NRT) model, modified version of Kinchin and Pease, the numbers of Frenkel pairs (interstitial-vacancy pairs) created by PKA can be estimated by

$$\nu_{NRT}(T) = \frac{\kappa E_D(T)}{2E_d} \tag{2.1}$$

where $E_D(T)$ is denoted to damage energy, E_d is the energy needed to strike an atom out from its lattice position, or displacement energy. κ is usually taken as 0.8. More commonly, total number of displacement per atom (dpa) is used in irradiation damage measurement. The NRT dpa parameter is given by

7

$$dpa = \int \int \phi(E)\nu_{NRT}(T)\sigma(E,T) \; dt \qquad\qquad (2.2)$$

where $\phi(E)$ stands for neutron flux and $\sigma(E,T)$ is the probability of atom with energy E transfer energy T to the recoil particles. Most of the vacancies and interstitials will recombine in a very short time, only a fraction of point defects can escape from the cascade, called freely migrating defects (FMD). These FMD strongly influence the irradiated microstructures, and leads to vacancy cluster formation (voids) or interstitial cluster formation (dislocations).

In addition to FMD clusters, fission gas play the primary role in fuel/cladding deformations due to the internal pressure. Both FMD and fission gas accumulation lead to dimensional change, or swelling, and close the gap between fuel alloys and cladding materials. Figure 2.4 (a) shows a typical swelling behavior in the type 316 cladding after neutron irradiation, and Figure 2.4 (b) is the corresponding transmission electron microscope (TEM) image reveals the voids formation. The consequence is the fuel cladding chemical interaction, or FCCI, which is the major challenge in fuel performance and reactor safety.
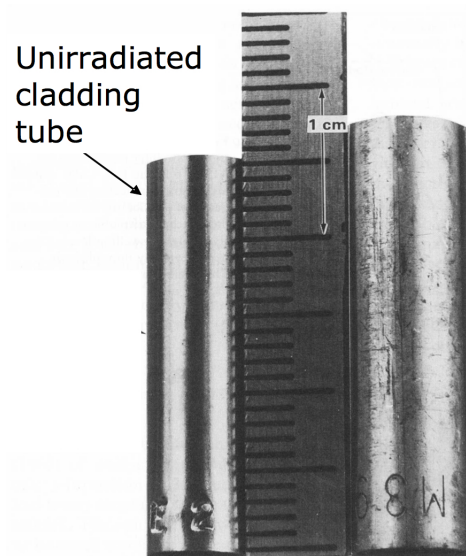
(a) Irradiated SS 316
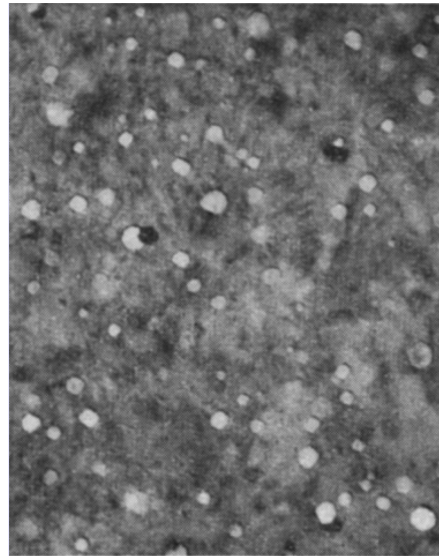
(b) Corresponding TEM image of voids

Figure 2.4: Radiation-induced microstructural change −− void swelling

2.3   Fuel cladding chemical interaction

Metallic fuel has been considered as a candidate for advanced nuclear reactors, which operates at higher temperature and requires longer lifetime. It is important to understand the microsctructural changes during reactor operation, particularly the chemical interaction between fuel alloys and cladding materials, and able to predict the irradiation behavior and fuel performance[38, 35, 126, 14, 88, 143, 40]. The original spacing between fuel alloys and cladding materials is closed due to excessive swelling and intermatellics start to form[145, 103, 124, 31]. Figure 2.5(a) shows the contact initiates after fuel/cladding deformation. These phases, with relatively low melting temperature, are usually mechanically fragile. The interdiffusion process consumes cladding materials and degrades the structural integrity. The possible failure mechanism is shown in Figure 2.5(b), coolant may penetrate into the reactor

core through the cracked fuel/cladding interface[32, 41, 117, 135, 15, 24, 104, 44].

(a) fuel/cladding swelling   (b) Fuel pin failiure
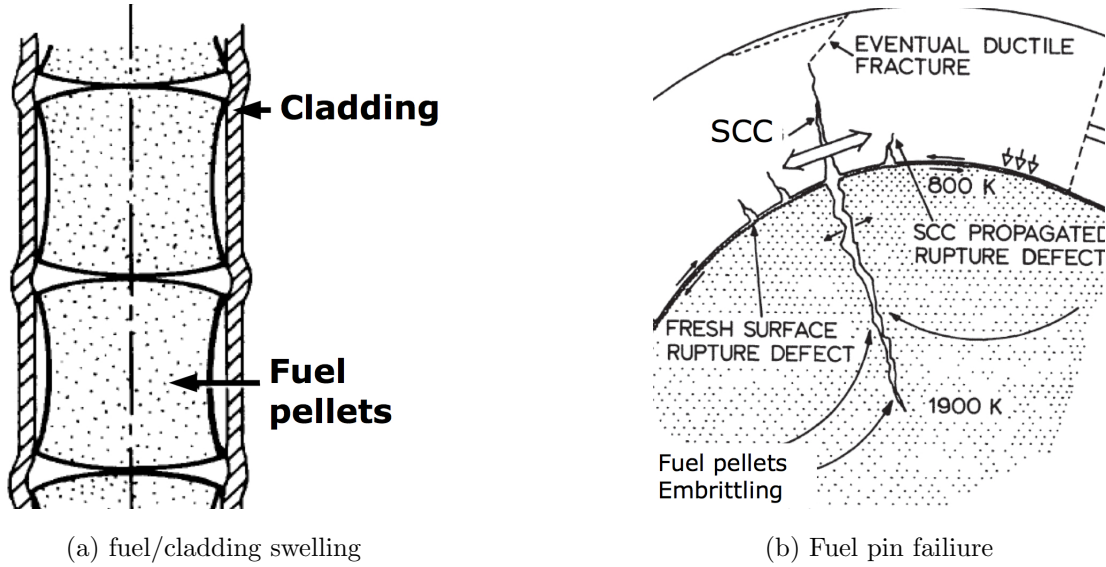
Figure 2.5: Fuel pellets-cladding interaction

Efforts have been made to study FCCI during EBR-II tests. Zirconium (Zr) and molybdenum (Mo) addition to fuel alloys were proven to increase the melting points which matched the anticipated operating temperature[74, 99, 33, 101, 6, 119, 23, 42, 57]. Cladding materials, such as HT9 and D9, were assembled with U-based metallic fuels up to 10 at% burnup. Possible diffusion barriers were tested to suppress the FCCI, including chromium coated layer and neodymium-added fuel alloys[12, 13, 20, 75, 141, 16, 85]. Ex-reactor experiments were conducted at elevated temperatures, mainly focused on metallic fuels bonded with stainless steels, which formed complex multi-component diffusion systems. In order to support atomic simulation and predict fuel performance, fundamental understanding is needed from simple binary diffusion system, involving initial microstructures of intermetallics and

diffusion kinetic data[146].

2.4 Diffusion couples technique: solid-solid interaction

In order to investigate thermokinetic data, solid-solid diffusion couple technique is used. This powerful tool provides comprehensive analysis to the phase formation at the annealing temperature, which can be used to validate phase diagrams. It does not restrict the formation of any phases allowed in the phase diagram, which is close to the practical reactor operations at elevated temperatures. It also deduces the complexity of testing a large alloying matrix with various compositions, which is often the case in traditional alloying approaches.

The formation of intermetallics or compounds, usually microscale in bulk system, are easily identified with microscopical tools, such as scanning electron microscope (SEM) and electron probe microanalysis (EPMA). The reaction zone is governed by Gibbs phase rule, shown in equation 2.3 ,

$$F = C - P + 2 \tag{2.3}$$

where F is the degrees of freedom, C is the number of components, and P is the number of phases. With given temperature and pressure, there is no additional freedom for composition changes, which leads to straight interface with fixed composition. The composition profile shows a step distribution with corresponding local phase equilibrium. It provides the understanding of microstructural information in thermally-activated multidiffusion system, in particular to study FCCI with possible constituents to verify phase equliibria. In addition, bulk diffusion systems have the advantage in mechanical properties test, such as nano-indentation for hardness measurement on each intermetallic. The oxidation, however, leads to poor bonding at delay the interdiffusion process. The rough interaction zone is often noticed

with large interface variations. In order to avoid oxidation, other techniques have also been tested using physical vapor deposition (PVD) or chemical vapor deposition (CVD). The deposition is highly uniform and not influenced by surface roughness on the substrate. Energetic argon is used to remove surface oxidation layers to form clean alloy interface.

2.5 Ion acceleration

The neutron experiments in nuclear reactor are usually costly and time consuming. With the help of accelerator technology, ion irradiation has been widely used to simulate neutron damages. Figure is the 1.7 MV tandem accelerator operated in the Ion Beam Laboratory at Texas A&M University. Incident ions are produced in the ion source and accelerated through acceleration column via electric potential. Desired ion specie is selected using magnetic filed based on mass to charge ratios and electrostatic lenses are used for beam optics.

Figure 2.6: A schematic of the 1.7 MV tandem accelerator at Texas A&M University. From right to left are the two ion sources, followed by a low-energy mass-selection magnets, T-shape tank with high voltage terminal, a quadrupole lens and a high-energy magnetic mass analyzer. Two major beam lines shown here: the implantation chamber with temperature control shown as second beam line and the analysis chamber shown as the third beam line.

The entire beam line and target chambers are held under vacuum, typically around 10^{-7} Torr to avoid ion-gas collision. The target chamber equipped with thermocouple for precise temperature control, and faraday cup is usually used to measure the beam intensity. Upon different charge state of incident ions, typical ion energy are of the range between keV (10^3 eV) to MeV (10^6 eV). Heavy ion (e.g. Fe) irradiation is often used to study radiation effects in materials, with relatively low cost and fast damage accumulation. Simultaneous annealing can be coupled with ion irradiation, which makes the experiments apply to practical reactor operations.

2.6 Interdiffusion coefficient Boltzmann Matano method

Scanning electron microscope (SEM) with energy dispersive X-ray spectroscopy (EDS) was employed to characterize intermetallics formation. The thickness can be measured throughout the interdiffusion zones. In addition, concentration profile of phase constituents provides thermokinetic data and microstructural information for diffusion studies.The diffusion coefficient in a multi-compound binary system can be determined using Matano-Boltzmann method with following equations:

$$\tilde{D}_i^{int} = \int_{N_i(x_1)}^{N_i(x_2)} \tilde{D}dN_i = -\int_{x_1}^{x_2} \tilde{J}dx \tag{2.4}$$

where $\tilde{D}$ is the integrated interdiffusion coefficient of a specific phase in (x_1, x_2) and ideally should be the same in all diffusion couples regardless experimental boundary condition. $\tilde{J}_i$ is the interdiffusion flux at position x as described in equation (2.5)

$$\tilde{J}_i(N_i^*) = \frac{1}{2t}\int_{N_i^{\pm\infty}}^{N_i^*}(x - x_0)dN_i \tag{2.5}$$

where x_0, known as the Matano plane, is the average position weighted on con-

centration N_i.

$$\int_{-\infty}^{+\infty} (x - x_0)dN_i = 0 \tag{2.6}$$

The obtained diffusion coefficients then can be applied in an Arrhenius equation, equation (2.7),to find activation energy Q and maximum diffusion coefficient D_0 for the specific phase. The diffusion coefficients and activation energy play a huge role in establishing advanced multiscale atomic modeling in metallic fuel development.

$$D = D_0 e^{-\frac{Q}{\kappa T}} \tag{2.7}$$

2.7 Motivation and objectives

The FCCI is one of the major materials challenges in metallic fuel development. However, the knowledge of thermally-activated multicomponent diffusion followed by irradiation tests is quite limited. , Combined both experimental and theoretical investigation are essen- tial to predict the feasibility of fuel designs. The overall objective of this dissertation is to unravel the radiation effects in microstructural and kinetic data.

3. EXPERIMENTAL AND CHARACTERIZATION METHODS

3.1 Fabrication of diffusion couples

There are two diffusion systems covered in this dissertation, the first system is the uranium-free diffusion couples. Specimen contains polycrystalline iron (99.99%), zirconium (99.2%), and molybdenum (99.2%). It was sectioned into 3 mm disks and mechanically polished through 0.5 μm alumina. Before assembly, the dilute nitric acid is used to remove oxidation layer from the polished surface. Prior to sealing, the quartz capsule was repeatedly vacuumed (10^{-6} Pa) and purged with Ar/H_2 gas mixture. Later, the binary diffusion couples were bonded and sealed into quartz capsule. Both Fe/Zr and Fe/Mo diffusion couples were annealed under vacuum at 850°C for 15 days. Table 3.1 lists the sample matrix for uranium-free systems.

Table 3.1: Uranium-free sample matrix

Sample name	Component	Temperature (°C)	Time (hours)
Fe/Zr	iron/zirconium	850	360
Fe/Mo	iron/molybdenum	850	360

The second system is uranium-bearing system. In order to avoid oxidation, specimen preparation was carried out under an argon (Ar) environment inside glove box. Depleted uranium (DU) was sectioned to 2mm in thickness and then polished with Buehler MiniMet 1000. Sectioned DU was polished with silicon carbide to grade 1200. Finished surface was etched with dilute nitric acid solution before assembly. Bonded diffusion couples were placed in a stainless steel clamp and wrapped with

tantalum foil. A quartz ampoule was used and evacuated to 4 x 10^{-6} pascal prior sealing . Fig 3.1 shows the closed system between glove box and furnace to avoid contamination.
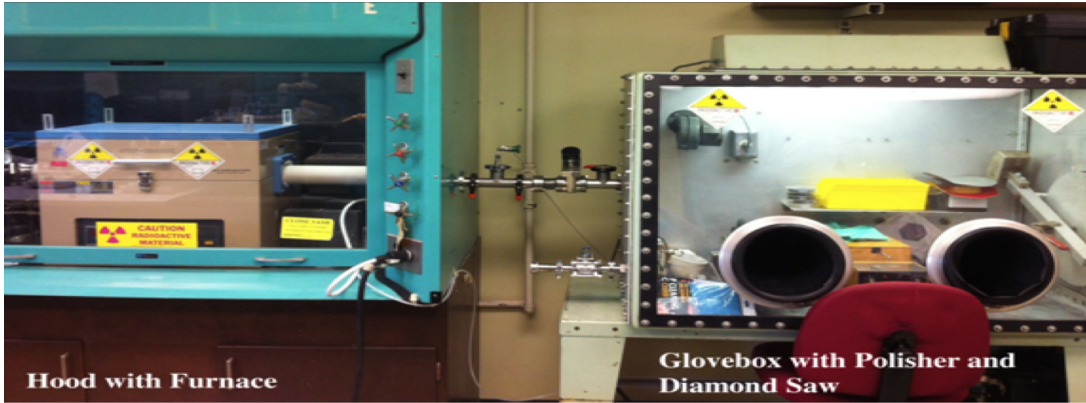
Figure 3.1: Closed system for specimens transportation

Two types of single crystal systems, nickel and iron, with different annealing condition are shown in the Table 3.2 and Table 3.3. In addition, combined with helium irradiation, the diffusion couple is assembled with polycrystalline iron to study microstructural evolution and listed in Table 3.4.

Table 3.2: Uranium-bearing sample matrix-single crystalline Fe

Sample name	Component	Temperature (°C)	Time (hours)
U/Fe A1	depleted uranium/iron	575	168
U/Fe A2	depleted uranium/iron	600	144
U/Fe A3	depleted uranium/iron	625	120

Table 3.3: Uranium-bearing sample matrix-single crystalline Ni

Sample name	Component	Temperature (°C)	Time (hours)
U/Ni B1	depleted uranium/nickel	675	360
U/Ni B2	depleted uranium/nickel	700	312
U/Ni B3	depleted uranium/nickel	725	264

Table 3.4: Uranium-bearing sample polycrystalline Fe

Sample name	Component	Temperature (°C)	Time (hours)
U/Fe C1	depleted uranium/iron	700	96

In parallel with bulk system, the thin-film diffusion couples were also studied. Metallic thin-films were deposited onto uranium substrate using AJA International A2800 6-gun physical vapor deposition system and alloy target were acquired from ACI Alloys Inc. The whole process was kept under 2.8 x 10^{-7} Torr. DU surface was pre-cleaned by using a radio frequency power of 50 Watt, roughly 240 volt Ar ion bombardment. The desired thickness of 1μm was achieved for time of 200 minutes, 20 standard cm^3 / sec and 200 Watt DC power on the target. Fe(99.9%) , Fe-20wt%Cr and Fe-20wt% Cr-20wt%Ni bonded with DU were prepared and characterized. Figure 3.2 shows the schematics for the as-deposited thin-film couples.
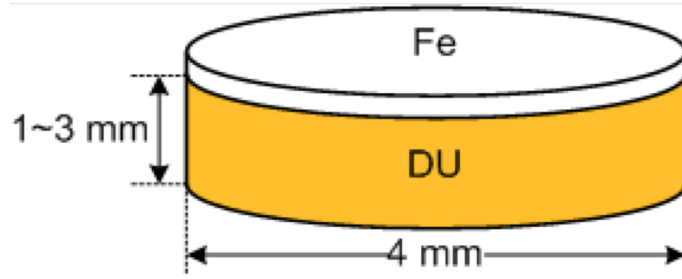
Figure 3.2: Schematic of as-deposited thin-film couples

3.2 Characterization methods

3.2.1 Electron microscopy

Scanning electron microscope (SEM) provides morphology information using focused energetic electrons. The interaction volume for incident electron is $\sim 1~\mu$ m deep. Secondary electrons (SE), backscattered electrons (BSE), and characteristic X-rays will be generated. SE mainly comes from the specimen surface with relatively good depth of focus. BSE has the better contrast regarding to atomic numbers (Z), which the higher the Z , the brighter contrast in BSE micographs. With equipped energy dispersive spectrometry (EDS), the chemical composition can be determined by analyzing characteristic x-rays. In this dissertation, SEM is employed to obtain following information 1) inter metallic phase identification through composition profiles mapping. 2) the thickness measurement for each phase formed for interdiffusion coefficient calculation.

Microstructural information play an important role of understanding FCCI. Therefore, transmission electron microscope (TEM) is intensively performed through this dissertation. The resolution limit for typical light microscope is ~ 300 nm. The lattice parameter of crystal structures, however, is on the scale of angstrom ($\overset{\circ}{A}$). Based on the de Broglie relation ,

19

$$mv = h/\lambda \tag{3.1}$$

$$D = \lambda d^2 \tag{3.2}$$

$$\lambda \propto C_V/C_V{}^* \tag{3.3}$$

where m represents mass, v is the velocity, and h stands for Planck's constant. The electron wavelength λ of 200 kV acceleration voltage is 0.025 $\mathring{A}$ which is sufficient for microstructural characterization.

Energetic electrons are generated from the gun tip, which is either filament or cold emission design, and focused through various lens to form images. The two major modes of operation in TEM are imaging mode and diffraction mode. The electrons pass through the specimen and project the images onto the fluorescent screen or CCD camera, called image mode. It is strongly dependent to the specimen composition and thickness. The other mode is diffraction mode, it reveals the microstructure by indexing the diffraction patterns.The images formed at the back focal plane is constructed by diffracted electrons and provides microstructural information. By using the following equation,

$$d = \frac{\lambda L}{R}, \tag{3.4}$$

where d represents the lattice spacing, R is the distance obtained from reciprocal space (usally a ring or point), L is the camera length, and λ is the electron wavelength.

In addition to conventional TEM, scanning TEM (STEM) focused the electron beam down to nanometer size and scanned across the specimen. Similar to the SEM,

20

chemical composition can be acquired via default point or line scanning packages with equipped EDS system. With the help of High-angle annular dark-field imaging (HAADF), the STEM provides the options with image contrast upon composition (Z). In HAADF images, the higher the atomic number, the brighter the contrast. Figure 3.3 explains the basic image formation mechanism between TEM and STEM.
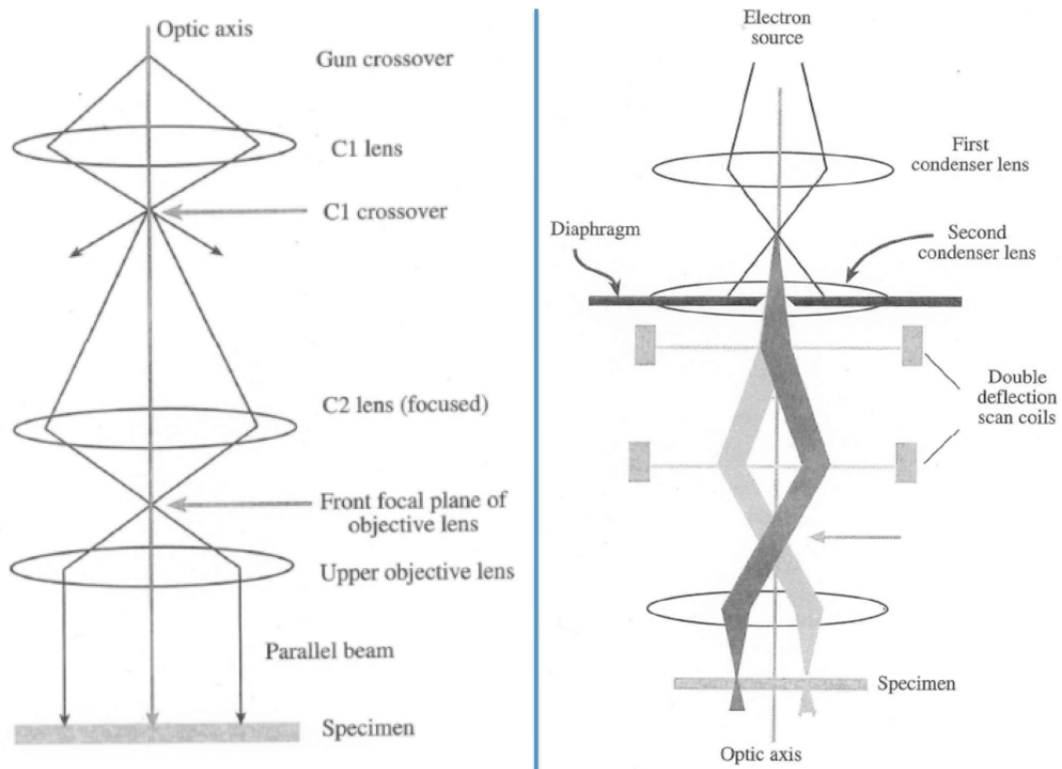
Figure 3.3: Illustration of the working principles for TEM and STEM

In order to achieve electron transparent thickness, cross-sectional specimens were prepared using focused ion beam (FIB) lift-out technique. The area of interest was covered by platinum(Pt) deposition as a protection layer. 30 keV gallium (Ga) ion was used to remove extra materials away from the lamellae. Lamellae was then lift

with nano-manipulator and transferred to TEM grid for further thinning process. Final thickness of less than 100 nm can be achieved for TEM characterization.

3.2.2 Rutherford backscattering spectrometry

Rutherford backscattering spectrometry (RBS) is a common ion beam analysis technique for element distribution and depth profile. Typically, 2 MeV helium (He) ion is used in RBS . A collimated He beam will bombard the specimen, after energy transfer and two-body collision, some He ions will be backscattered to the detector with partial energy remained. The basic configuration of RBS system is shown in Figure 3.4 with the detector set up at 165 degrees. The energy deposited on the detector from the backscattered He ions corresponds to the depth below the surface and target compositions. Calibration of the standard samples is needed for better interpretation, usually using silicon and gold as the reference targets. The spectrum obtained from RBS has to be compared and simulated via computational codes for analysis. SIMNRA was used to study the diffusion behavior in DU/thin-film system, and by changing the target composition, depth profile can be extrapolated.
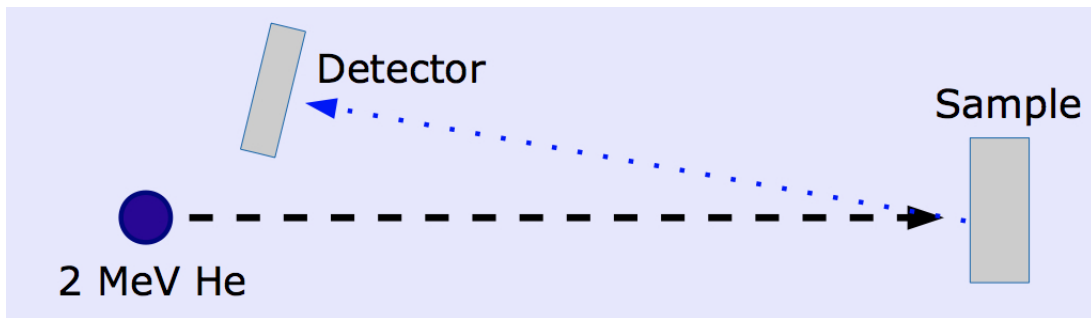
Figure 3.4: Typical arrangement for Rutherford backscattering spectrometry

4. URANIUM-FREE DIFFUSION SYSTEMS[*]

The present section consists of a background of the zirconium and molybdenum addition in metallic fuel application, followed by a series of interrelated experiments using Fe/Zr and Fe/Mo diffusion couples. Thermally-activated diffusion couples were annealed at 850°C for 15 days. SEM was employed to gather diffusion kinetics and composition profiles across the interaction layers. The specimens are both irradiated with energetic Fe ions up to 130 displacement per atom (dpa). After irradiation, cross sectional TEM specimen was prepared using focused ion beam and detailed microstructural analysis was performed.

4.1   Background of zirconium and molybdenum addition in metallic fuels

The major issues of utilizing metallic fuels to the integral Fast Reactor is fuel cladding chemical interaction (FCCI). Intermetallic phases with relatively low melting point formed at the reaction interface, which has poor mechanical properties and may lead to serious structural failure. The addition of zirconium into uranium-based fuels or uranium-plutonium-based fuels has been tested and developed since 1980s during EBR-II program[34, 1, 90, 26, 138, 83, 82]. Up to 10 weight percent (wt%) Zr addition is proven to effectively reduce the interdiffusion of iron and nickel from the cladding constituents, and increase the high temperature stability of U-Pu fuel alloys. Later in 1985, multiple fuel-cladding experiments were performed involving U-Pu-Zr alloys and varies austenitic steels. It has been found that the ZrO_x and ZrN were formed and acted as diffusion barriers. However, uranium and plutonium were

---

found enriched between the zirconium layer and cladding, and caused accelerated cladding consumption at elevated temperatures.[81, 122, 78, 89, 36, 25, 77, 111]

Researchers in the U.K and France started working on U-Pu-Mo since 1960s. It was unsuccessful due to the poor swelling resistance. Through the collaboration of Argonne National Laboratory (ANL) and Idaho National Laboratory (INL), efforts have been made on metallic fuel development based on U-Mo alloys[60, 61, 58]. The option of using molybdenum over zirconium has the benefits of 1) avoiding phase separation in U-Zr fuel systems. 2) increasing the thermal conductivity. Reduced Enrichment for Research and Test Reactors (RERTR) is one the oldest program supported by U.S. Department of Energy since 1978. Recently, U-Mo based alloys are of great interest in INL with the support from RERTR program[108, 94, 22, 43, 95, 134, 144]. The U-Mo alloys have demonstrated with highest thermal conductivity and highest melting point over U-Zr and U-Nb systems. However, the fundamental studies of binary diffusion systems are limited. In order to investigate diffusion kinetic and microstructural evolution of the intermetallics phases during reactor operation, in particular to understand FCCI and support mulitscale modeling of fuel performance, simple binary diffusion couples were fabricated followed by heavy ion irradiation[62]. Zirconium and molybdenum are the two major elements considered as additions to the fuel alloys. The binary diffusion couples were assembled using iron, as the surrogate to cladding constituent in structural steels, with zirconium and molybdenum[50, 113, 27, 64].

4.2   Iron-zirconium diffusion couple

Prior to decide the experiment temperature, the phase diagram of Fe-Zr is shown in Fig. 4.1, including four equilibrium phases of $FeZr_3$, $FeZr_2$, Fe_2Zr and $Fe_{23}Zr_6$. A quick summary of crystal structures for each equilibrium phase is as follows, 1)

FeZr$_3$ takes orthorhombic structure and stabilized up to 928°C; 2) FeZr$_2$ has tetragonal structure up to 962°C; 3) Fe$_2$Zr remains face-centered cubic structure up to 1700°C; and 4) Fe$_{23}$Zr$_6$ has a Th$_6$Mn$_{23}$ structure with eutectic point at 1590°C. Each equilibrium phase has quite fixed stoichiometric composition.

However, the formation of each phase in the Fe-Zr system is not completely understood. For instance, Kubaschewski, Arias and Abriata reported Fe$_{23}$Zr$_6$ as an equilibrium phase, which was not observed by Aleksseva, Korotkova and Stein et al. Early studies have suggested either Fe$_{23}$Zr$_6$ is a high temperature phase or it may be stabilized by impurities, such as oxygen. An argument has been made that both Fe$_{23}$Zr$_6$ and FeZr$_2$ are not equilibrium phases unless the presence of oxygen. Liu et al. suggested that Fe$_{23}$Zr$_6$ nucleates on the surface of FeZr$_2$ particles and has the peritectoid reaction of (αFe) + Fe$_2$Zr $\rightarrow$ Fe$_{23}$Zr$_6$. Thus, we chose to use diffusion couple technique to study the phase formation, which avoids possible contamination or oxidation during melting process. 850°C was selected as annealing temperature, and is below the eutectic point for the diffusion couples fabrication. In the following section, we will be focusing on the phase formation upon annealing and irradiation effects of the Fe-Zr diffusion couple. .
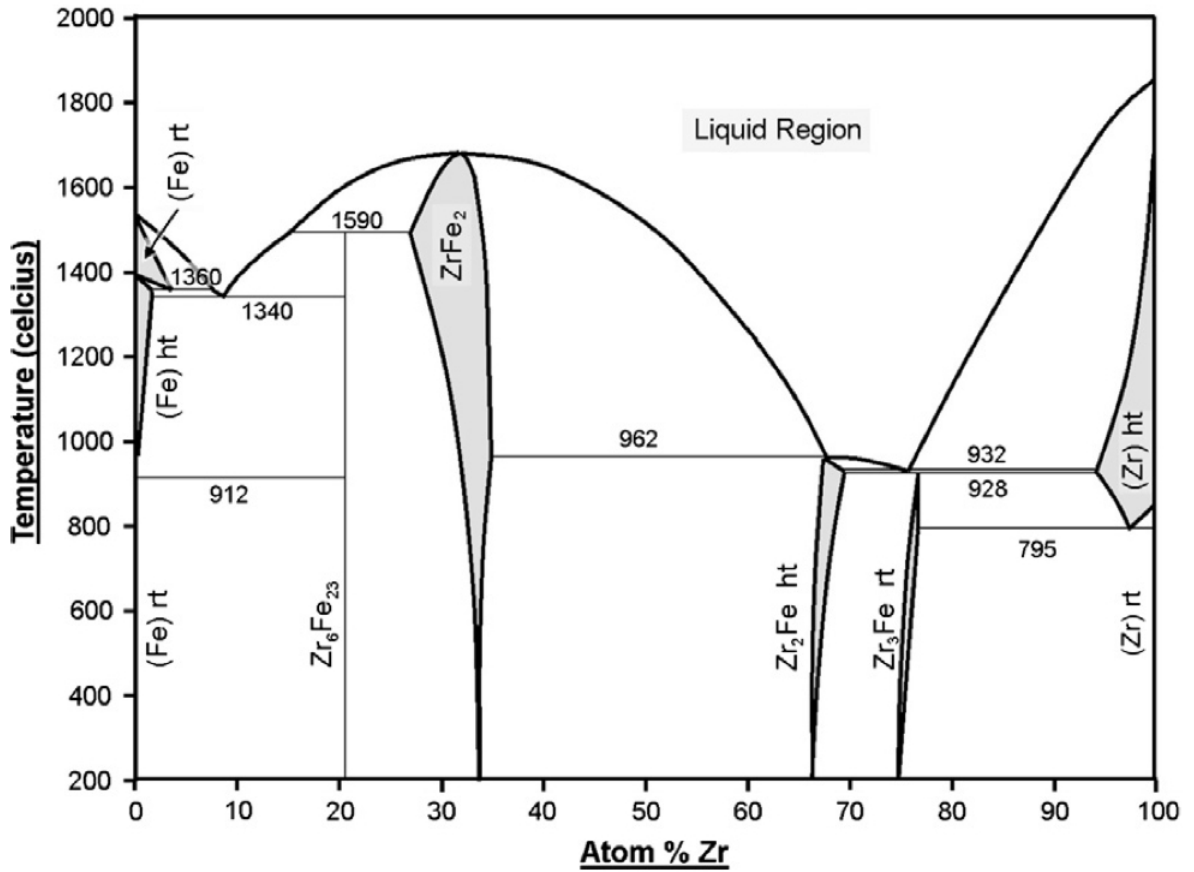
Figure 4.1:   Phase diagram of Fe-Zr

4.2.1   Phase identification and diffusion kinetics

The iron-zirconium diffusion couple was annealed at 850°C for 15 days. Complete experimental procedures are listed in the chapter 3. After annealing, the capsule was quenched in cold water and sacrificed the ampule using a hammer. The specimen was then cut in half vertically to the interface and embedded into epoxy to avoid surface oxidation. Post-polishing was conducted down to micro-meter size suspension, which reduced surface roughness created while sectioning prior to irradiation. All the characterizations were studied on the polished surface.

Scanning electron microscope (SEM) and energy dispersive x-ray spectrometry (EDS) were performed to study the phase formation at interface. Fig. 4.2a shows the backscattered SEM micrograph of Fe-Zr diffusion couples after polishing. Three noticeable contrasts were observed at the reaction zone. EDS scanning was performed and compositional profile is plotted in Fig. 4.2b. Two phases were identified as Fe_2Zr and $Fe_{23}Zr_6$. The third contrast was not clear at this point under SEM examination, further discussion will be covered through transmission electron microscope in the later section.

The diffusion length of Fe_2Zr phase is 9.8 μm and 4.1 μm for the $Fe_{23}Zr_6$ phase. It is worth noting the third phase with darker contrast next to zirconium contains small amount of iron. It might be the precursor forming the Fe_2Zr, which indicates a mixture of alpha iron and Fe_2Zr phase . The integrated interdifusion coefficients can be calculated by using Eq. 2.6, and $\tilde{D}$ of each phase are listed in Table 4.1. The interdiffusion coefficient of Fe_2Zr phase is greater than the $Fe_{23}Zr_6$ phase, which is noticeable according to the diffusion length from Fig. 4.2a. The specimen will be ion irradiated to investigate radiation effect in the next section.
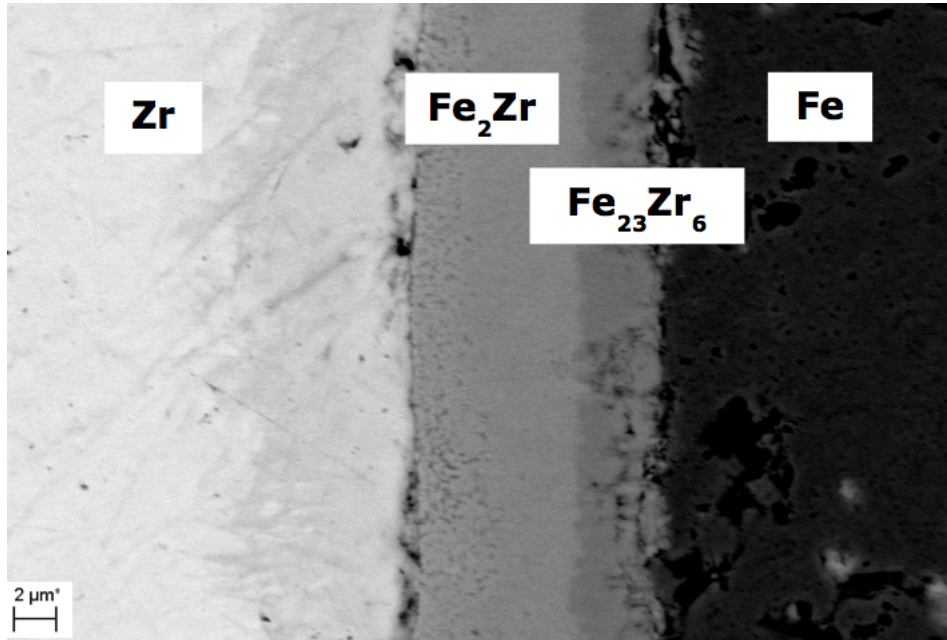
(a) BSE micrograph of Fe-Zr couple
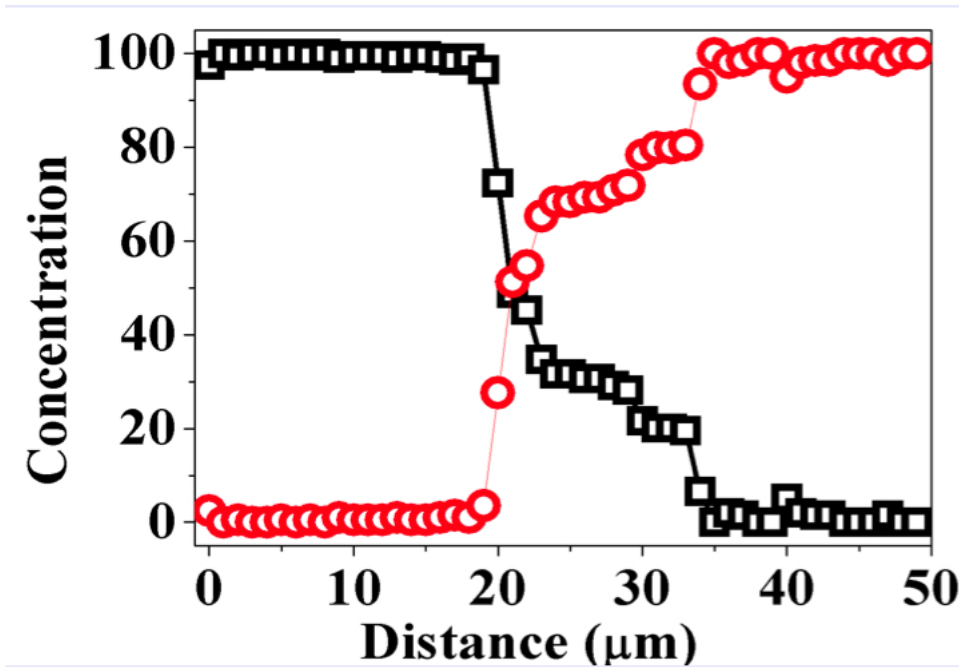
(b) Composition profiles of Fe-Zr couple

Figure 4.2: Fe-Zr diffusion couple annealed at 850°C for 15 days

Table 4.1: Extracted integrated diffusion coefficients of Fe vs Zr

$\tilde{D}$ Fe$_2$Zr (at. frac. m^2/s)	$\tilde{D}$ Fe$_{23}$Zr$_6$ (at. frac. m^2/s)
1.59 x 10^{-16}	1.01 x 10^{-16}

4.2.2 Ion irradiation and sample preparation

The Fe-Zr diffusion couple was irradiated with 3.5 MeV doubly-charged Fe ions to the fluence of 3.5 x 10^{16} Fe/cm^2, corresponding to $\sim$ 130 displacement per atom (dpa) at damage peak. The incoming ions were perpendicular to the interface. The experimental temperature was at 600°C with thermal couple welded on the sample stage. The vacuum during the irradiation was kept under 10^{-6} torr.

The depth profile of injected Fe and dpa was plotted in Figure 4.3 using SRIM calculation with full-cascade option. The ion penetration depth is $\sim$ 1.6 μm and the peak dpa is located at 1 μm. The peak injected Fe interstitials is less than 1 at% which doesn't change the chemical composition. The depth of interest will be focused within the ion projected range and cross-sectional specimen preparation will be discussed in the next paragraph.
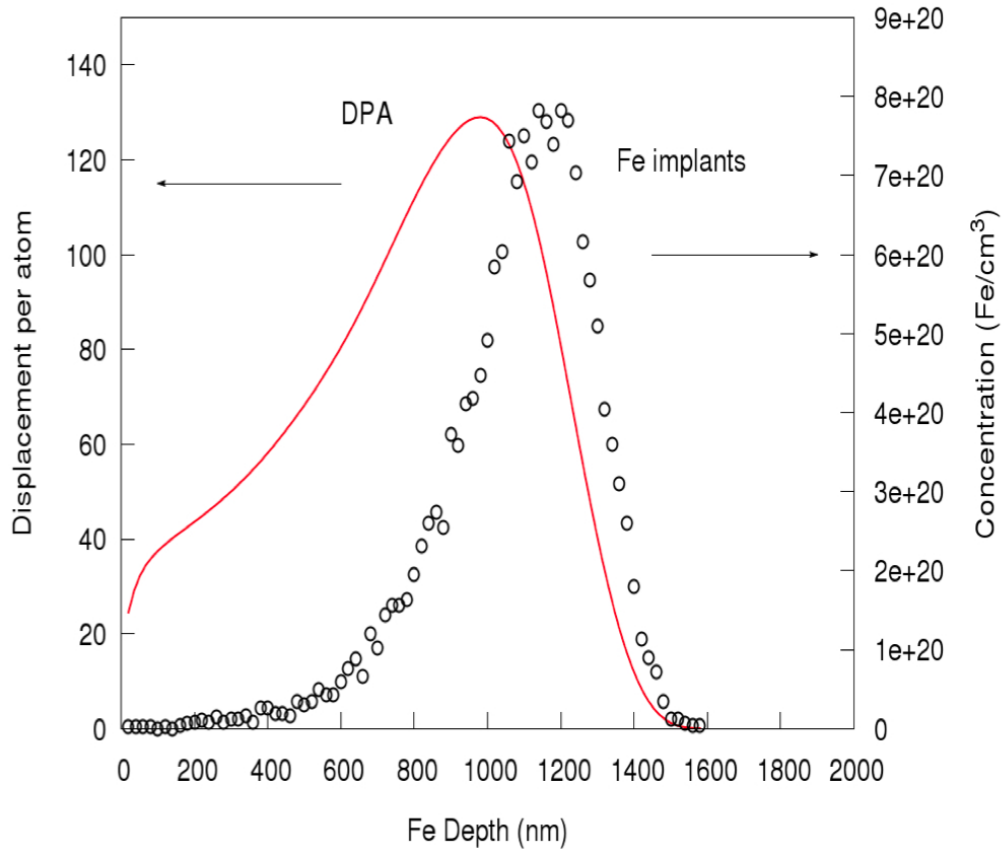
Figure 4.3: Experimental condition – 3.5 MeV Fe irradiation

The cross sectional TEM specimen was prepared by focused ion beam (FIB) with lift-out technique in a dual-beam SEM facility. The area of interest is selected across the interdiffusion zone, usually 12μm in width . Figure 4.4 shows the as-prepared TEM specimen with the average thickness of 70 nm. The top layer is platinum (Pt), which is deposited on the surface to reduce FIB damages. Based on the SRIM calculation, the depth of damage peak created by 3.5 MeV Fe ion is roughly 1 μm underneath the surface. It denoted as irradiated region, marked as dash line, throughout this dissertation. The depth beyond the irradiated region, usually 3 μm below the surface , it is selected as unirradiated region for comparison.

30
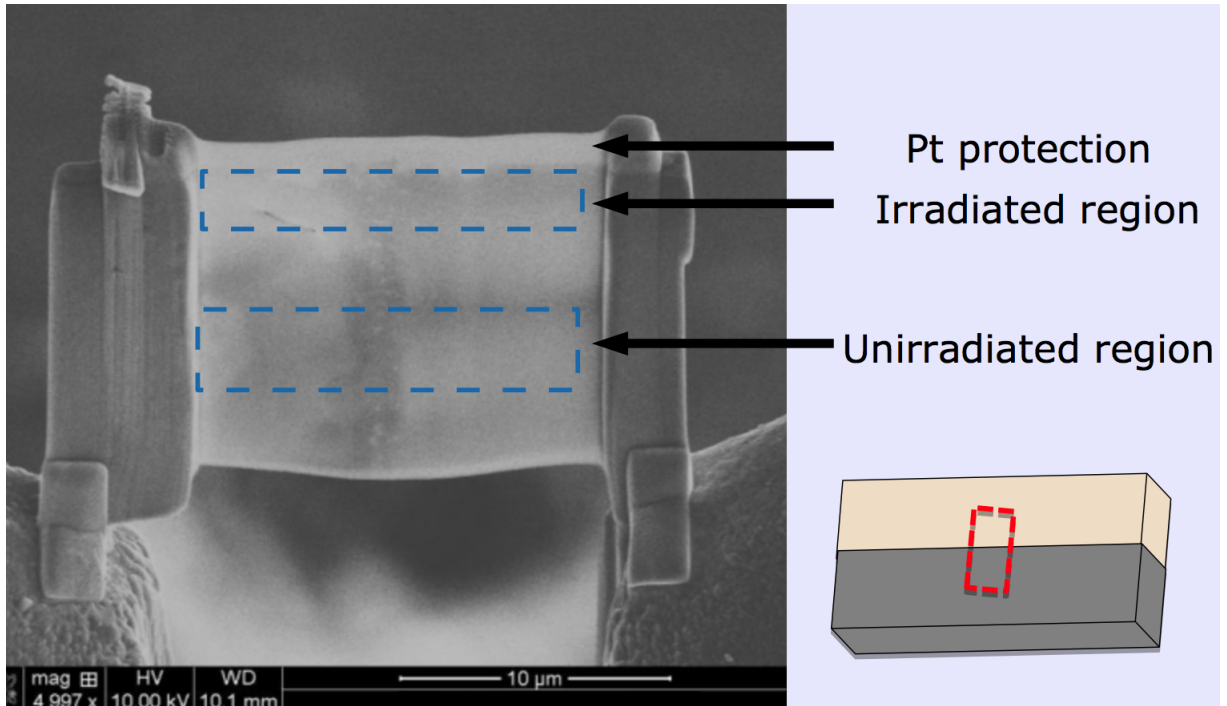
Figure 4.4: TEM sample preparation and description

4.2.3 Post-irradiation characterization

Scanning transmission electron microscope(STEM) is carried out for better atomic contrast, regarding the element distribution. The probe size is reduced down to nanometer spot under the STEM mode. Fig. 4.5 is a cross sectional STEM micrograph of Fe-Zr interface. The contrast of the traditional STEM micrograph is contributed from the atomic mass difference, which the heavier element shows the lighter contrast. The right side with darker contrast corresponds to iron side and the left side with lighter contrast corresponds to zirconium side. Irregular grains and particles were observed in the middle which suggests the existence of multiple phases.

EDS line scans were performed across irradiated region and unirradiated region.

The spectrum obtained from the unirradiated region shows the step-like profiles for both Fe and Zr distribution. This can be understood from the Gibbs' phase rule that with given pressure and temperature, no additional degree of freedom for composition changes. According to the atomic composition analysis, $FeZr_3$, $FeZr_2$ and Fe_2Zr were identified from each steps. However, the last step-height on the Fe side contains mixed phase, including αFe, $Fe_{23}Zr_6$ and $FeZr_2$. The details of the $Fe_{23}Zr_6$ formation will be discussed in later section.

For comparison of the unirradiated region, another line scan was conducted in the irradiated region, which was at the depth less than 0.5 μm below surface. The spectrum shows abnormally enhanced diffusion and no step-like distribution was observed. The Zr signals even appear at 8 μm away from the interface, also, both Fe and Zr signals contain huge fluctuations in the irradiated region. The damage cascades created by 3.5 MeV Fe ion irradiation increase the defect concentration and excessive vacancies/interstitials accelerate the atomic movement at elevated temperature and leads to radiation enhanced diffusion.
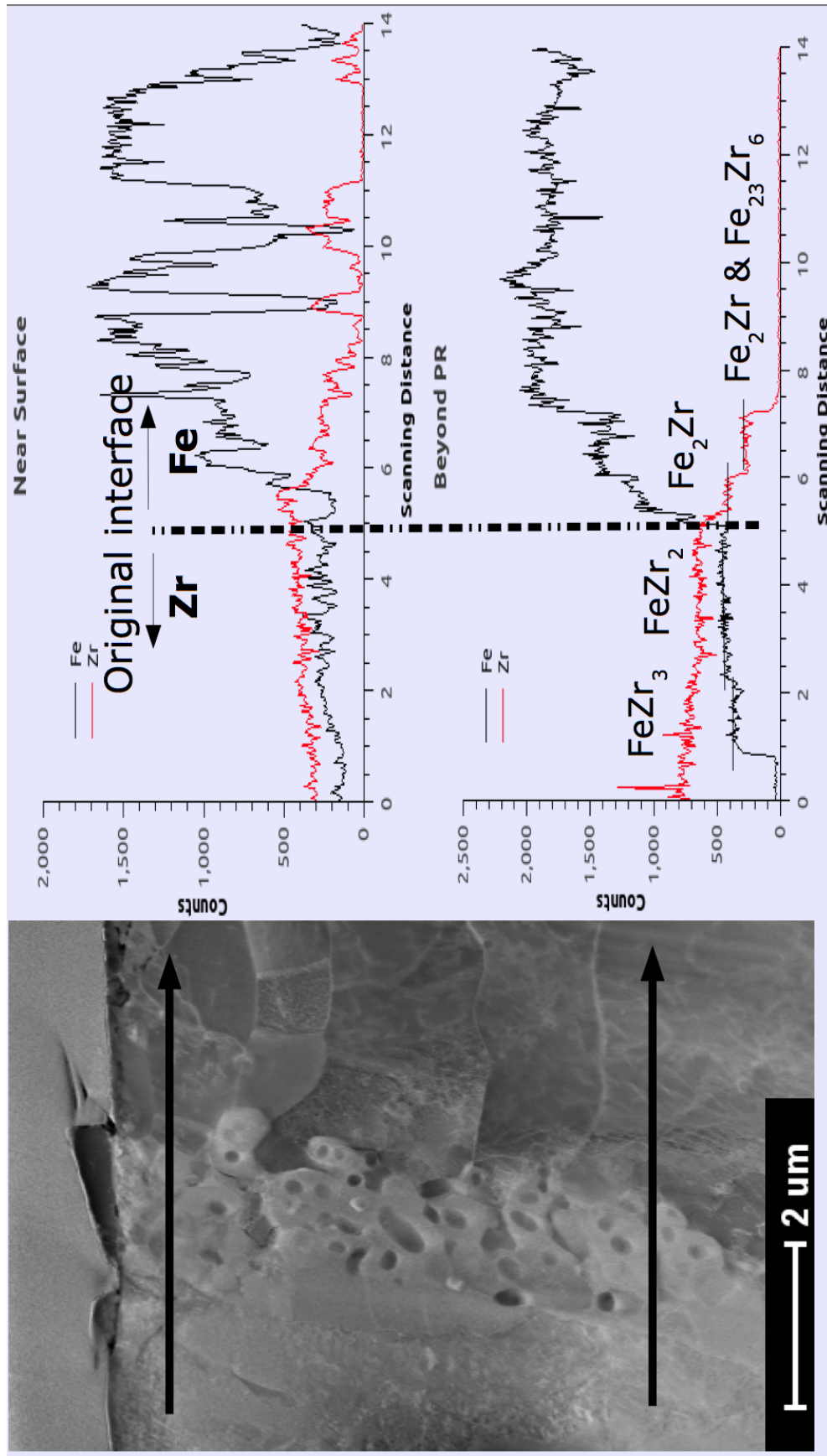
Figure 4.5: Radiation induced diffusion on Fe-Zr system STEM EDS line scan across interaction layer.

Fig. 4.6 is the BF-TEM micrograph and shows the overall microsctruce of Fe-Zr interface. The white solid line denoted to the ion-projected range and original interface is marked with blue arrow. We have observed irregular grains and particles with darker contrast along the interface, even beyond the ion projected range, which is formed during thermal treatment. According to EDS analysis, these dark particles were identified primarily to be $Fe_{23}Zr_6$ phase, while some of them were determined to be Fe_2Zr. Selected area diffraction (SAD) were performed to confirm the microstructures. Fig. 4.7 shows enlarged BF-TEM micrograph of the interaction zone and the SAD patterns of phases identified. (A) -(E) marked in the BF-TEM corresponds to where the local region of SAD is taken. The SAD patterns revealed the existence of αFe, $Fe_{23}Zr_6$ and Fe_2Zr. In addition, the SAD pattern of region (E) contains the mixture of Fe_2Zr and ZrO_2, which indicates the presence of oxygen. The SAD patterns with ring-like features suggests nano-crystal formation. The oxide precipitates in the interdiffusion zone will be discussed in the later section.

In addition, the Fe side shows some smaller grains or phases developed within the ion projected range. The average size of unirradiated Fe grain in the bulk, beyond the white solid line, is on the micro-meter range. The grains formed, however, after irradiation are on the range from 100 nm to 500 nm. The EDS, plot in Fig. 4.5, has shown that ion irradiation strongly promoted the Zr diffusion. Therefore, possible Fe/Zr phase formed due to non-equilibrium process following ion irradiation. The discrete grains/phases of newly formed Fe/Zr disappeared at the point where the noticeable Zr signal is gone in EDS plot, which indicates that the radiation induced phase formation is correlated to the Zr diffusion into Fe.
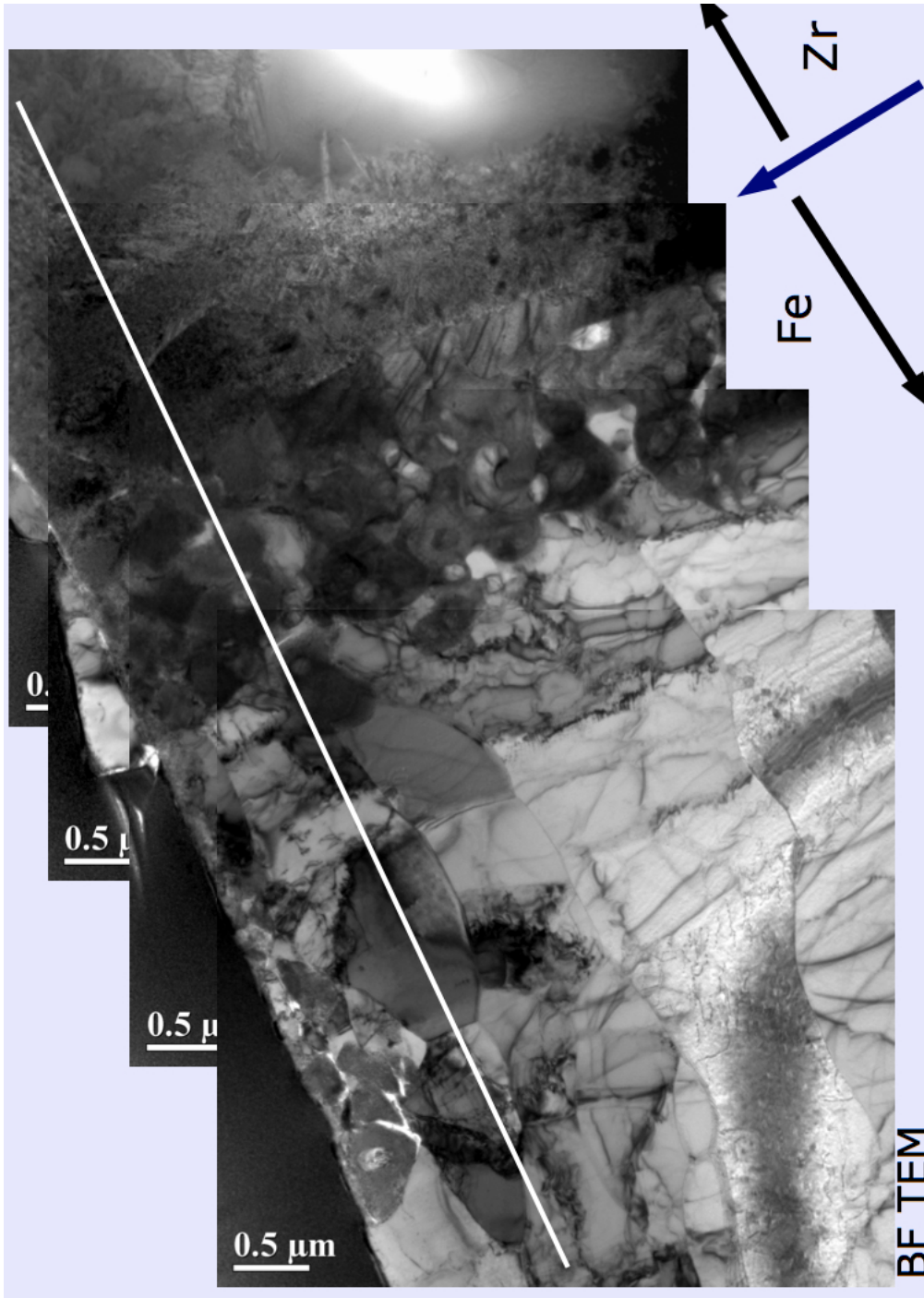
Figure 4.6: BFTEM of Fe-Zr diffusion couple
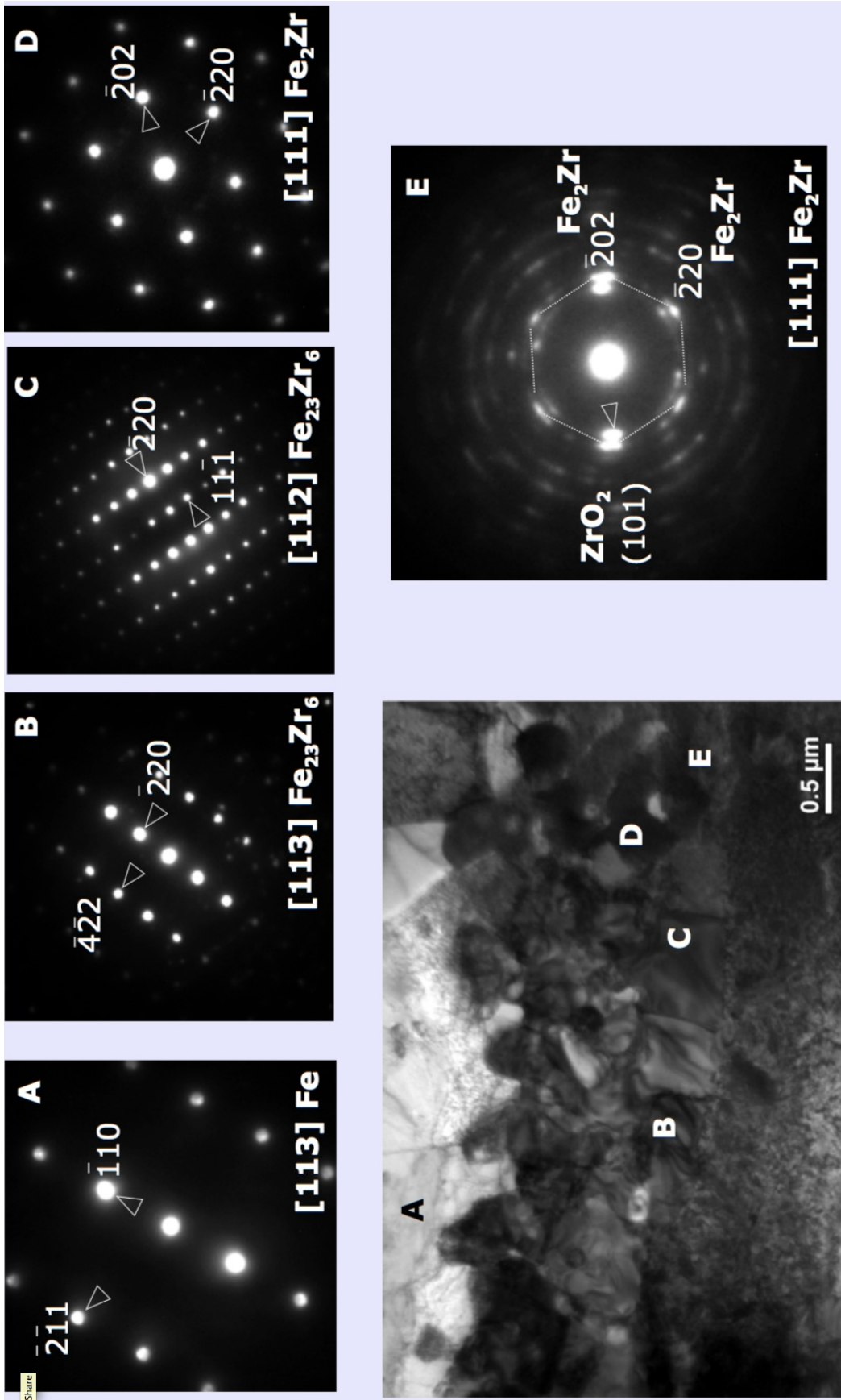
Figure 4.7: Microstructure of the intermetallic compounds SAD patterns.

Further effort was made on the irregular shapes appeared in the interaction layer. Dark particles act like a core structure within the gray phases which also incorporated in the dark matrix. The dark matrix of the STEM micrograph is the Fe side, and the other side is Zr. The core-particle structures can be seen throughout the interface. Figure 4.8 shows closed look of core-particle structures, marked as blue dash circle in STEM micrograph. EDS line scan, with beam spot size of ~ 1 nm, was performed across the two particles and surrounded matrix. Based on EDS spectrum, the composition profiles reveals that 1) the dark matrix is iron. 2) the core particles with darker contrast are O-rich Fe_2Zr. 3) the light gray phase surrounded O-rich Fe_2Zr is $Fe_{23}Zr_6$. These findings provide evidence and possible explanation to the argument of $Fe_{23}Zr_6$ formation.
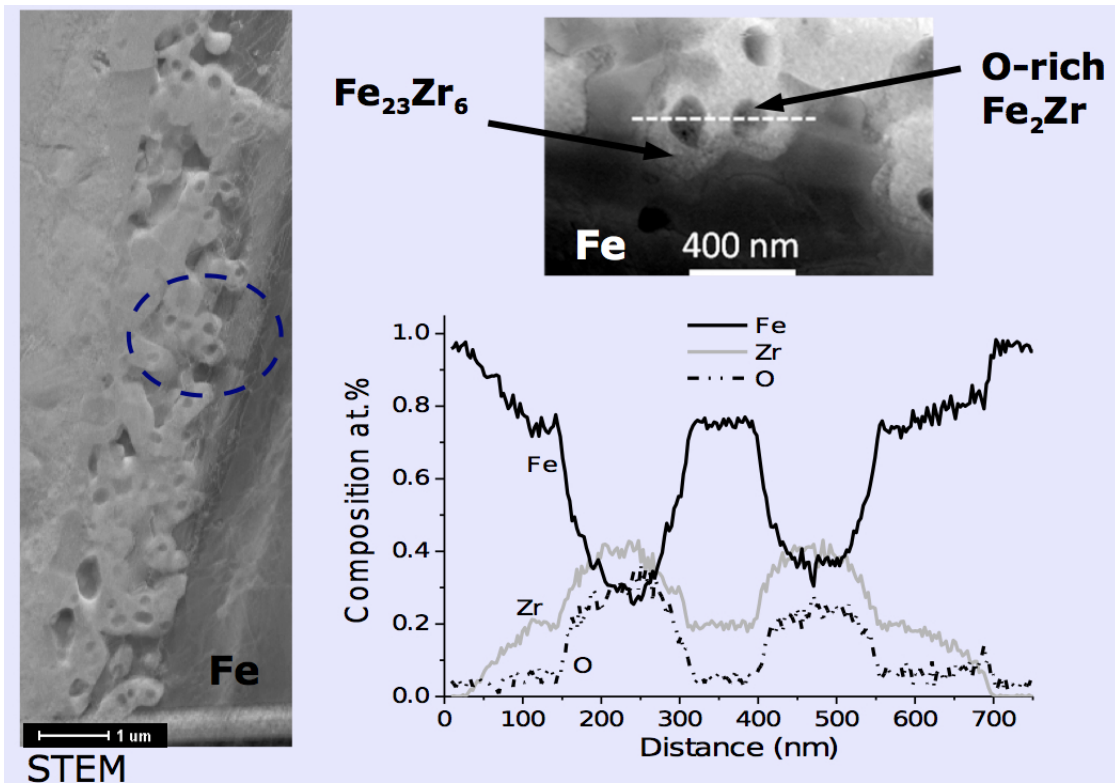
Figure 4.8: Oxygen appears in the interaction region STEM EDS line scan

37

4.2.4 $Fe_{23}Zr_6$ phase formation

The atomic composition across the two particles is plotted in Fig. 4.8. According to the EDS results, two interesting conclusions can be drawn here: 1) the presence of oxygen in the core structure, which has darker contrast. 2) the Fe is depleted from oxygen-rich core structure; also the lower the Fe composition, the higher O composition and vise versa. The zirconium composition in $Fe_{23}Zr_6$ phase is measured to be 20 at%, while the oxygen composition is 5 at%. If the oxygen is assumed to take zirconium substutional sites, the Zr composition should be 25 at% without oxygen presence. It agrees with the measurement from Liu et al. However, in the oxygen-rich phase, the Zr composition is measured to be 40 at% , not reflected the oxygen variation. Furthermore, the sum of Fe and O signals remains constant at about 60 at%, which suggests that oxygen may take the original Fe lattice site. This finding indicates that $Fe_{23}Zr_6$ is not the phase strongly absorbs oxygen. In addition, the $Fe_{23}Zr_6$ phase in this present study always surround the Zr-rich particles.A possible mechanism was proposed by Liu et al. : the $Fe_{23}Zr_6$ phase formation is through peritectoid reaction of (αFe) + $Fe_2Zr \rightarrow Fe_{23}Zr_6$. It will become difficult for inside growth of $Fe_{23}Zr_6$, while the required Fe have to diffuse from the α Fe matrix. However, the $Fe_{23}Zr_6$ transformation can be compensated via Fe diffusion from inside the Fe_2Zr phase.If the Fe depletion continues from Fe_2Zr phase, it might explain that observation by Abraham et al. finding the αZr and Fe-Zr mixture inside $Fe_{23}Zr_6$.

Previous studies have suggested that $Fe_{23}Zr_6$ is the phase that strongly absorbs oxygen, and referred to be a metastable phase. As shown in Fig. 4.8, we have found that it is Fe_2Zr to absorb oxygen, instead of $Fe_{23}Zr_6$. Figure 4.9 reveal the structure of O-rich Fe_2Zr phase. The box region marked in the STEM micrograph is further characterized by SAD analysis. The SAD pattern was indexed to be the mixture

of Fe_2Zr and ZrO_2. The ring-like diffraction pattern suggests that the core contains small grains. It agrees with the dark-field TEM micrograph, which shows nanometer size oxide particles .
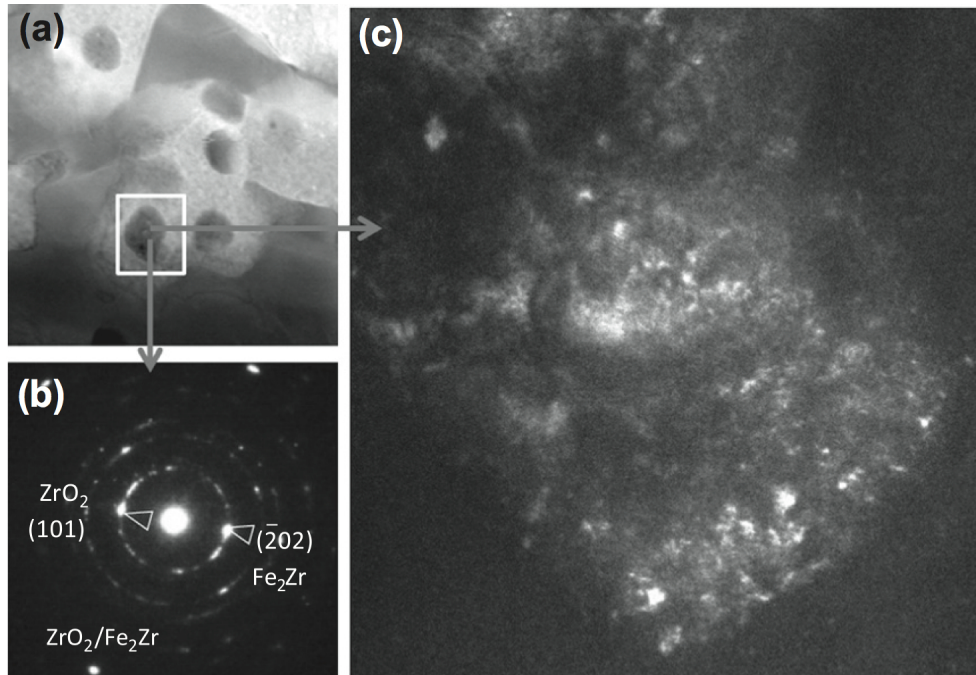
Figure 4.9: (a) STEM micrograph of one selected interaction region; (b) SAD pattern obtained from the core particle within the box specified region in (a); and (c) dark field TEM micrograph from the same region.

4.2.5 Radiation induced surface segregation

In addition to the radiation induced phase formation on the Fe side, Fig. **??** shows BF-TEM of an island-like feature at the near surface region. It appears that the precipitate formed right above the interaction layer after irradiation. The precipitate was confirmed to be αFe after SAD analysis, including multiple zone axises and a convergent beam electron diffraction (CBED) pattern. The ring-like features also

39

suggests that the surface αFe particle consists of nanometer size grains. The interface between the αFe particle and matrix is quite smooth. It is, therefore, not likely formed due to the phase segregation while annealing. The island-like features were not observed on the surface prior to irradiation. This concludes, due to the enhanced diffusion, the surface particles are driven by Fe migration towards the surface through grain boundaries and ion irradiation promotes crystal nucleation and growth. The mechanism, however, of the precipitate formation remains unclear.
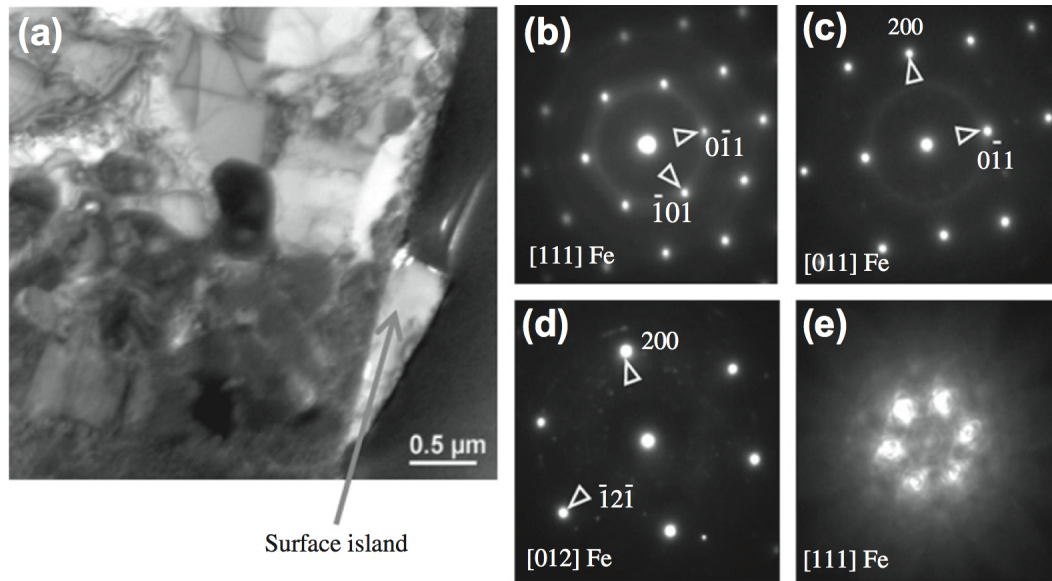
Figure 4.10: (a) Bright-field TEM micrograph obtained from the irradiated sample and (b – e) SAD patterns collected under different orientations for the surface particle marked by the arrow in (a).

4.3   Iron-molybdenum diffusion couple

Figure 4.11 shows the Fe-Mo phase diagram and suggests two equilibrium phases of Fe2Mo and Fe7Mo6 : Fe2Mo exists at the composition of 33.3 at% Mo. It has the MgZn$_2$-type hexagonal structure and belongs to Laves phase called C14; Fe$_7$Mo$_6$

also has hexagonal structure and exists at a composition range of 39 - 44 at% Mo. However, the Fe-Mo system is not completely understood regarding the nature of these two phases. For example, Fe_2Mo was first reported by Zaletaeva and Shnha confirmed its existence. It is also observed multiple times by varying Fe to Mo ratio in bulk alloy method, but Fe_2Mo was not detected by Heijwegen and Rawlings et al. in diffusion couples[76, 47, 80, 129, 105, 118, 79]. To understand the phase equilibrium and irradiation effects in the Fe-Mo system, the diffusion couple technique was used to investigate the intermetallic compounds. The advantages of this technique are: through the thermal interdiffusion process, phase formation will not limit to the equilibrated alloy;it can possibly, perhaps at right temperature and time, reveal most of the compounds from phase diagram.
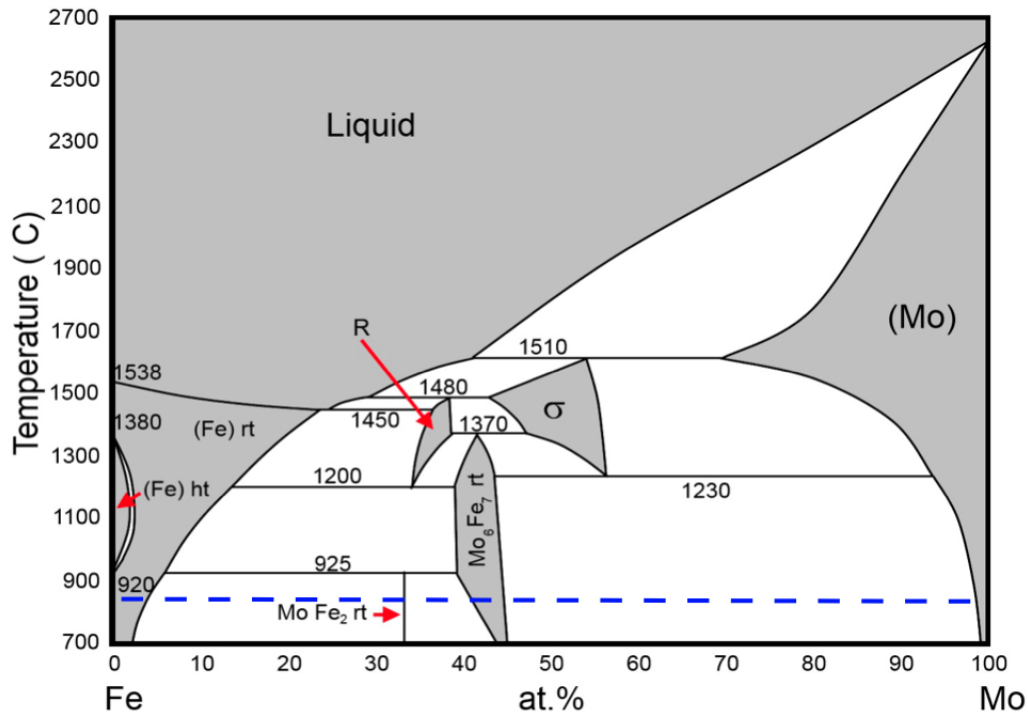
Figure 4.11: Phase diagram of Fe-Mo

4.3.1 Phase identification and diffusion kinetics

An iron-molybdenum diffusion couple was mechanically bonded via stainless steel clamp and annealed in a vacuum furnace at 850°C for 15 days. Prior to assembly, polycrystalline Fe (99.99%) and Mo (99.2%) metal disk were polished and etched in diluted nitric acid to remove possible oxidation layer. The diffusion couple was sealed inside a quartz capsule. Detailed steps can be found in the previous section of Fe-Zr. The sample was dropped into cold water by breaking up the capsule to speed up quenching.

SEM and EDS were performed on the interface prior to irradiation. Fig. 4.12a is the backscattered SEM micrographs and two phases formed at the reaction zone. According to quantified composition plotted in Fig. 4.12b, the two phases are identified to be Fe_7Mo_6 and Fe_2Mo. The diffusion length of each phase was recorded and Table 4.2 lists the integrated interdifusion coefficients $\tilde{D}$ of Fe_7Mo_6 and Fe_2Mo phases. The integrated interdiffusion coefficient of the Fe_2Mo phase is two times larger than the Fe_7Mo_6 phase, which leads to farther diffusion length of the Fe_2Mo phase in Fig. 4.12a.
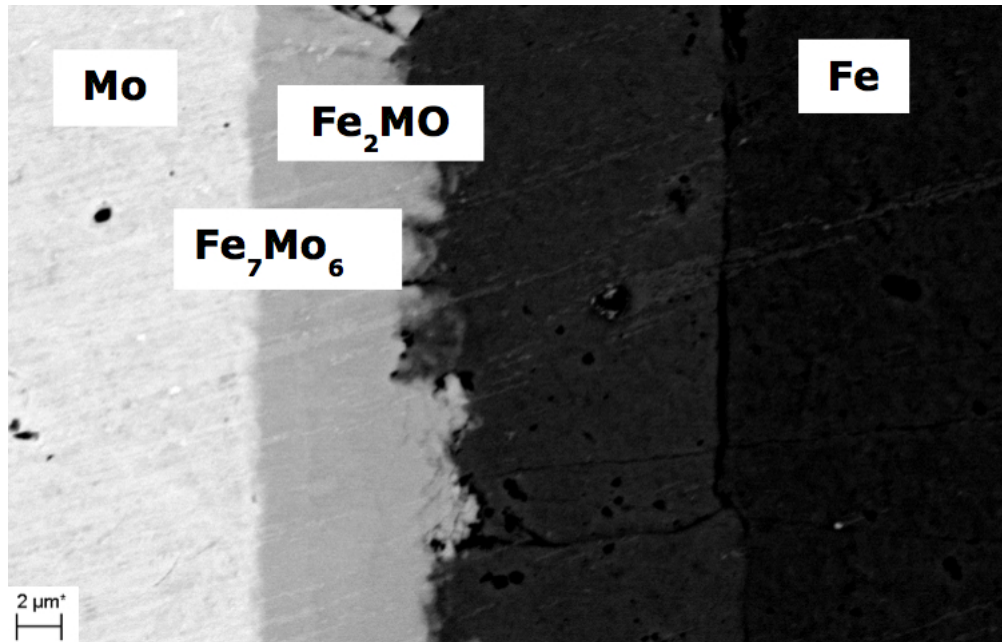
(a) BSE micrograph of Fe-Mo couple
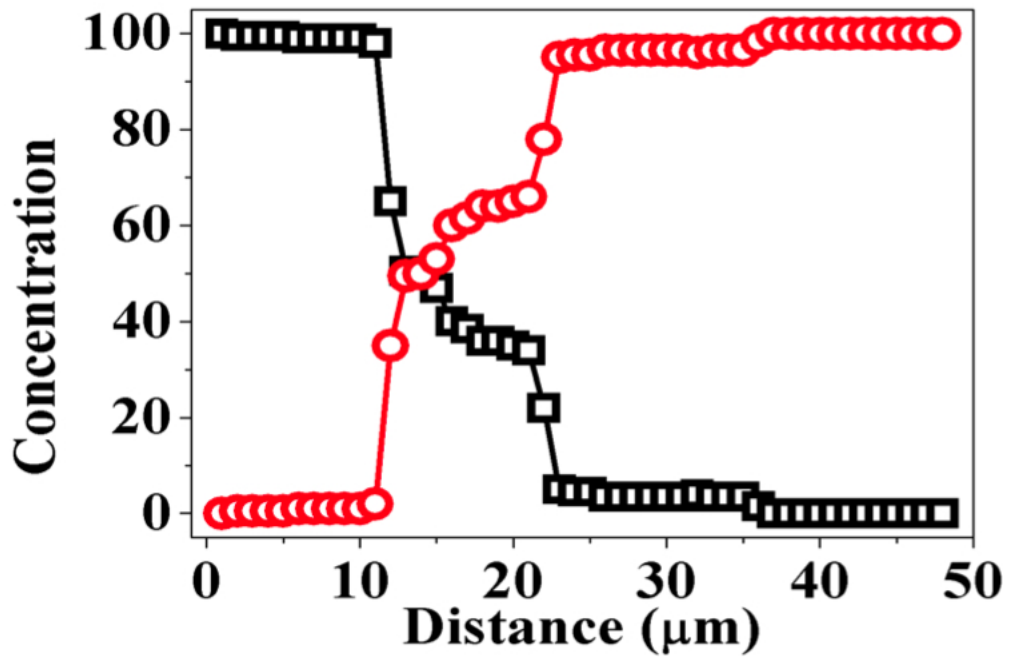
(b) Composition profiles of Fe-Mo couple

Figure 4.12: Fe-Mo diffusion couple annealed at 850°C for 15 days

Table 4.2: Extracted integrated diffusion coefficients of Fe vs Mo

Fe_7Mo_6 (at. frac. m^2/s)	Fe_2Mo (at. frac. m^2/s)
0.9 x 10^{-16}	1.94 x 10^{-16}

4.3.2   Ion irradiation and sample preparation

The Fe-Zr diffusion couple was irradiated with 3.5 MeV Fe ions to 3.5 x 10^{16} Fe/cm^2, corresponding to $\sim$ 130 displacement per atom (dpa) at damage peak, at 600°C under 10^{-6} torr. After ion irradiation, cross-sectional TEM specimens were prepared in a FEI Quanta 3D FEG dual beam SEM/FIB microscope using lift-out method. The platinum layer was deposited for few micrometers on the surface to protect the ion induced features during Ga^+ milling. Two steps thining was used to reduce the ion damage from Ga^+ bombardment: relatively high beam current is for quick material removal and lower beam current with glancing angle is for final cutting and cleaning purposes.

4.3.3   Post-irradiation characterization

TEM specimens were then characterized by two electron microscope. Selected area diffraction (SAD) and X-ray energy dispersive spectroscopy (EDS) for phase identification was taken by JEOL JEM-2010. Bright-field images, scanning TEM (STEM) and nanobeam EDS scanning was taken by FEI TECNAI G2 -ST. Both microscopes were operated with accelerating voltage of 200 kV. The STEM images were acquired by high-angle annular dark field (HAADF) detector and showed better contrast upon the atomic numbers difference.

STEM micrograph of cross-sectional Fe-Mo diffusion couple after ion irradiated is shown in Figure 4.13. The left side corresponds to Mo side with lighter contrast,

and relatively dark on the right corresponds to Fe side. The interaction zone in the middle contains two types of grains,one has the layer-like structures and the other has the rectangular shapes. The top arrow refers to the ion penetration depth which is approximately 1.3 um from the surface. EDS line scanning was performed along the solid arrow to compare the composition within ion bombardment region and beyond.

The spectrum in Figure 4.13 shows the comparison between irradiated and unirradiated regions. The spectrum for irradiated region is collected from the line (less than 0.5 um beneath the surface). The line scan shows abnormally enhanced diffusion of Mo, and the sharp interface turns to a gradient-like distribution. In contrast to the irradiated region, another line scan was performed at 4 um below the surface. The spectrum shows clear step-height distribution at the interface. Large fluctuations are observed in Fe and Mo signal appears 6 um away from the interface within the irradiated area. With an close look in Fig 4.13, the solid line in the irradiated region may scan across newly formed precipitates or large grain boundaries, which implies ion bombardment helps atomic migration through the grain boundaries.
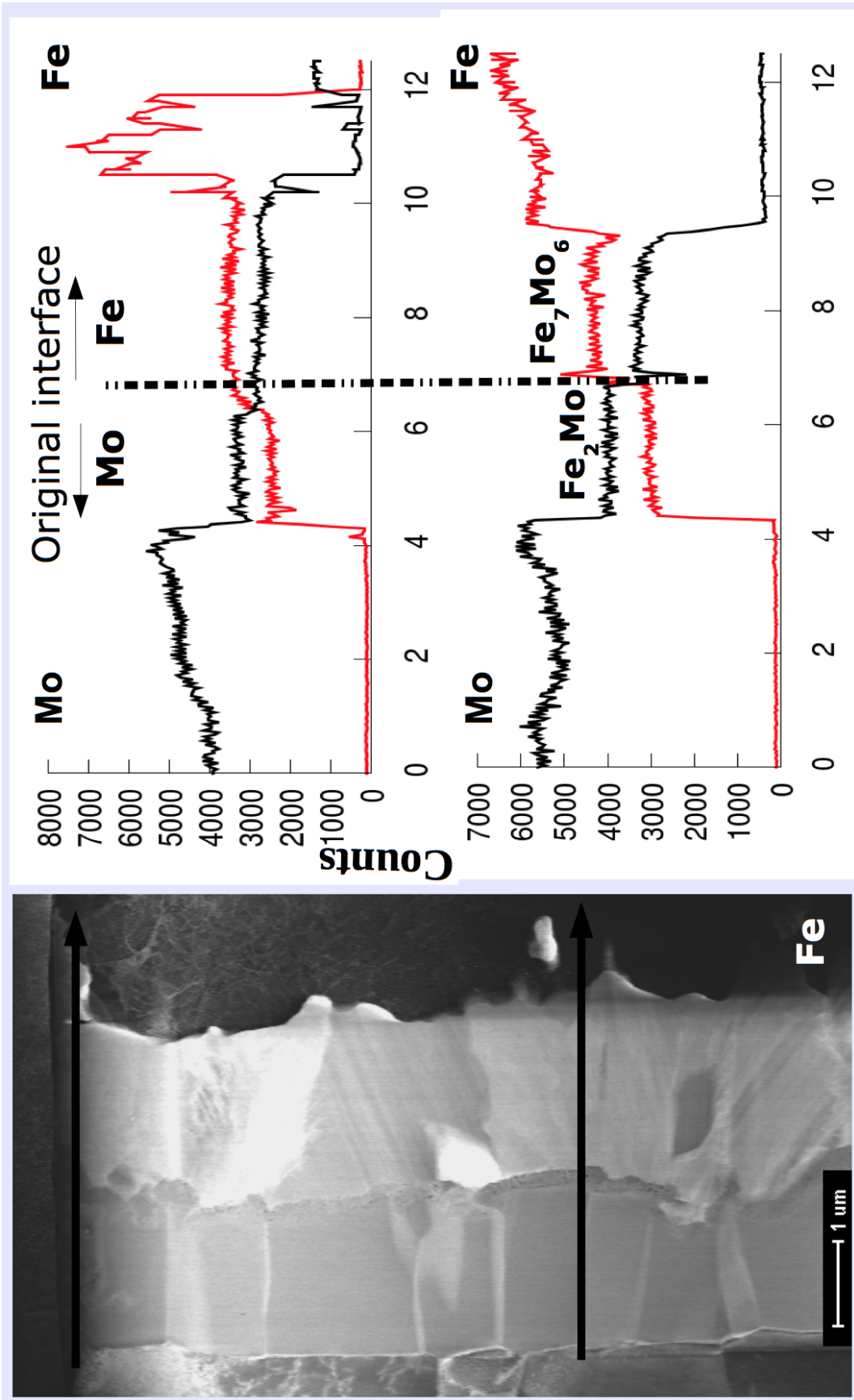
Figure 4.13: Radiation induced diffusion on Fe-Mo system STEM EDS line scan across interaction layer.

Bright-field TEM in Fig. 4.14 are stacked to show the microstructure across the interaction layer. The white solid line refers to the projected range (RP) of 3.5 MeV Fe ions and the blue arrow below corresponds to the original Fe-Mo interface. Smaller grains with dark contrast formed in the Fe side within the irradiated region, averaging 500 nm in size. We believe that the dark contrast is caused by radiation enhanced Mo diffusion and it agrees with the line scanning results. The process of new phase formation is accompanied with grain refinement. No evidence showing the grain refinement or phase formation on the Mo side. With the help of EDS analysis, two phases were identified in the interaction region. Layered structure with a dark contrast on the left is the Fe_2Mo, and Fe_7Mo_6 phase is on the right.
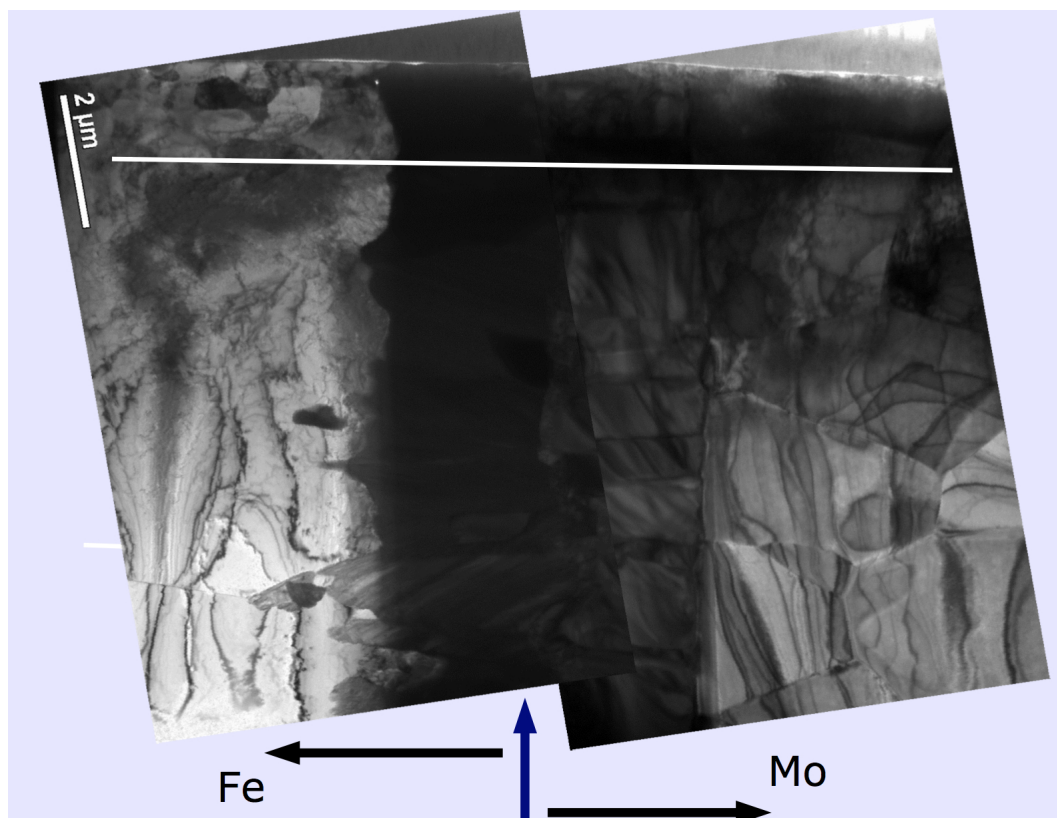
Figure 4.14: BFTEM of Fe-Mo diffusion couple

4.3.4 Crystal structures of Fe_2Mo, and Fe_7Mo_6

Efforts have been made to study crystal structure of Fe_2Mo, and Fe_7Mo_6 phases for the past two decades. Traditional alloying process, which containing various composition, were used to verify the phase diagrams. Fe_2Mo was reported as a C14, which belongs to Laves intermetallics with hexagonal closed packed crystal structure. The other phase has the rhombohedral crystal structure is referred to Fe_7Mo_6. Previous studies, done by Raghavan et. al. and Galimberti et. al., showed the TEM analysis of these two intermetallic phases in steels, and matched with theoretical data of phase diagram calculation. However, we have been observed different crystal structures for both Fe_2Mo, and Fe_7Mo_6 in the current diffusion couple.

Fig. 4.15 is the SAD patterns of the Fe_2Mo, and Fe_7Mo_6 phases. Eq. 3.4 allows us to calculate the lattice parameters and characterize the crystal structures through diffraction patterns acquired from TEM. With known Bravais lattice classification, Fe_2Mo phase, Fig 4.15a is well-indexed to be face-centered cubic (FCC) and has lattice parameter of 0.72 nm. The newly-defined crystal structure is verified through different zone axis and take the average lattice parameter due to the variation in defocusing. Fe_7Mo_6 phase is also characterized with the same method and referred to be face-centered cubic (FCC) with lattice parameter of 1.17 nm in Fig. 4.15b. These two FCC crystal structures of Fe_2Mo, and Fe_7Mo_6 phases are the first time being reported in the literatures, and more details of the irradiation effect will be discussed in the later sections.
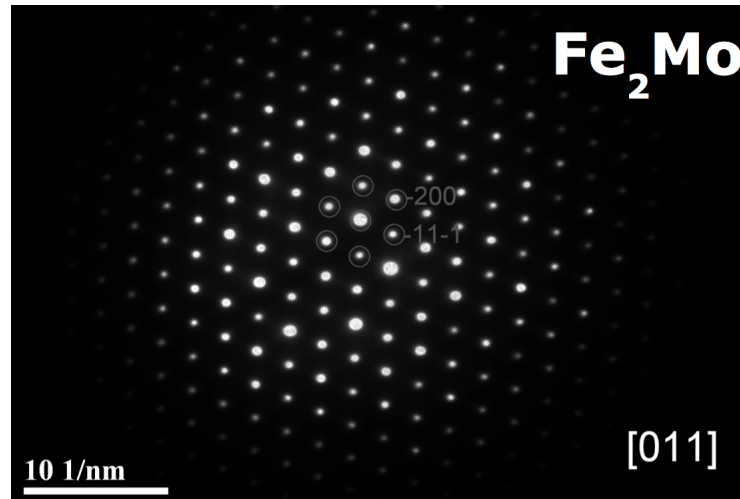
(a) SAD pattern of Fe₂Mo phase
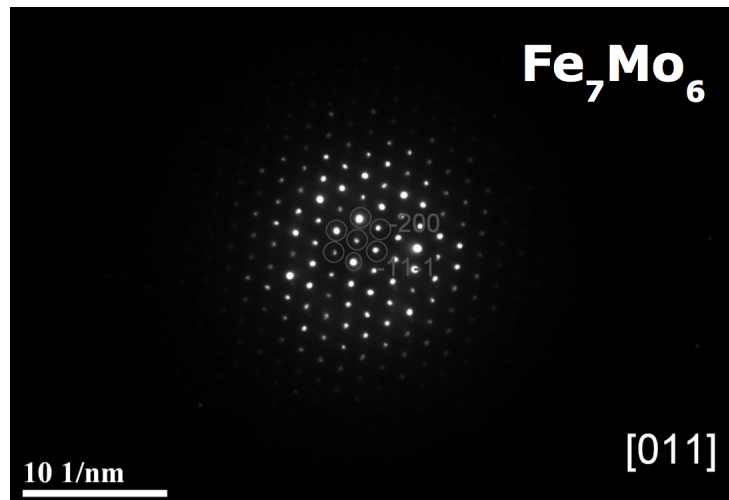
(b) SAD pattern of Fe₇Mo₆

Figure 4.15: Crystal structures of Fe$_2$Mo, and Fe$_7$Mo$_6$ phases revealed from selected area diffraction (SAD) pattern

4.3.5 Irradiation effects of Fe$_2$Mo, and Fe$_7$Mo$_6$

Fig 4.16 shows the bright-field TEM image and corresponding SAD patterns of Fe$_2$Mo, and Fe$_7$Mo$_6$ phases. The white arrow refers to the 3.5 MeV Fe ion projected range $\sim$1.1 μm. One of the advantages using the diffusion couple technique is able to

study irradiation effects on all possible phases. In previous section, Fe_7Mo_6 phase is reported as FCC crystal structure. As we examined the unirradiated region, which is well beyond ion projected range, and the irradiated region, the SAD patterns reveals the consistency of the Fe_7Mo_6 phase throughout the cross-sectional specimen. After ion irradiation, Fe_7Mo_6 phase remains its crystal structure and shows the radiation tolerant up to 100 displacement per atom (DPA). On the other side, the SAD patterns of Fe_2Mo changes significantly after irradiation compared to unirradiated region. The SAD of Fe_2Mo in Fig 4.16 indicates the FCC crystal structure has no longer retained.
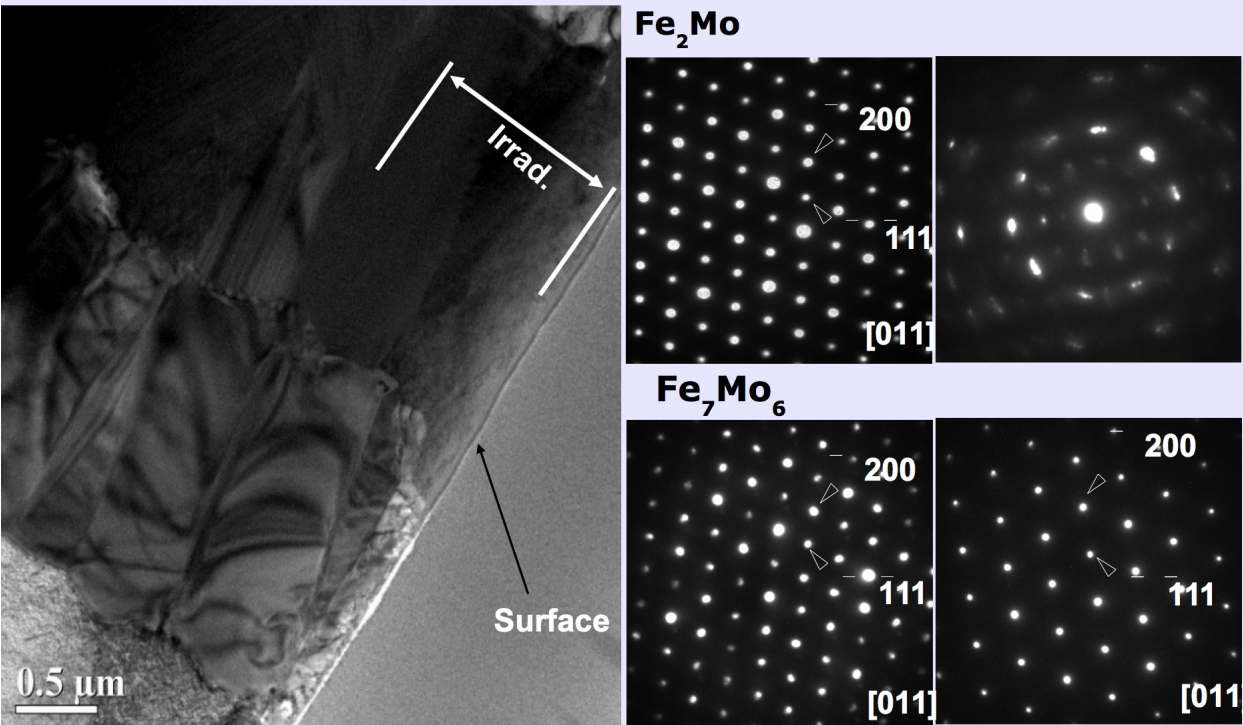
Figure 4.16:   Microstructure evolution of irradiated Fe_2Mo, and Fe_7Mo_6

4.3.6   Fe$_2$Mo phase and quasicrystal

Fig 4.16 shows unique SAD patterns of Fe$_2$Mo phase after irradiation, which indicates a transformation from FCC structure to a different symmetry. With careful examination, the unique symmetry we found belongs to one of the quasicrystal (QC) structures. The quasicyrstal, with forbidden five-fold symmetry, was first discovered by D. Shechtman in 1982. It lacks of periodicity but possess long-range order.

Fig 4.17 shows the BF TEM image of the irradiated interaction zones and corresponding SAD patterns to show the icosahedral quasicrystal (iQC) structures. We observed the two-fold (2f), three-fold (3f) and five-fold (5f) symmetry by rotating the specimen to different zone axis. It was found within the ion projected range from the Fe$_2$Mo phase. The icosahedral structure refers to a polyhedron with twenty identical triangular faces. It contains 12 atoms located at the vertices and 1 atom at the center of polyhedron. Previous iQC transformation in Fe-Mo system were only observed in the thin film specimen. Liu et al. reported the iQC from the annealed Fe-Mo thin film following ion beam mixing. It is, however, the clear evidence that iQC transformation has been first reported in bulk Fe-Mo systems.
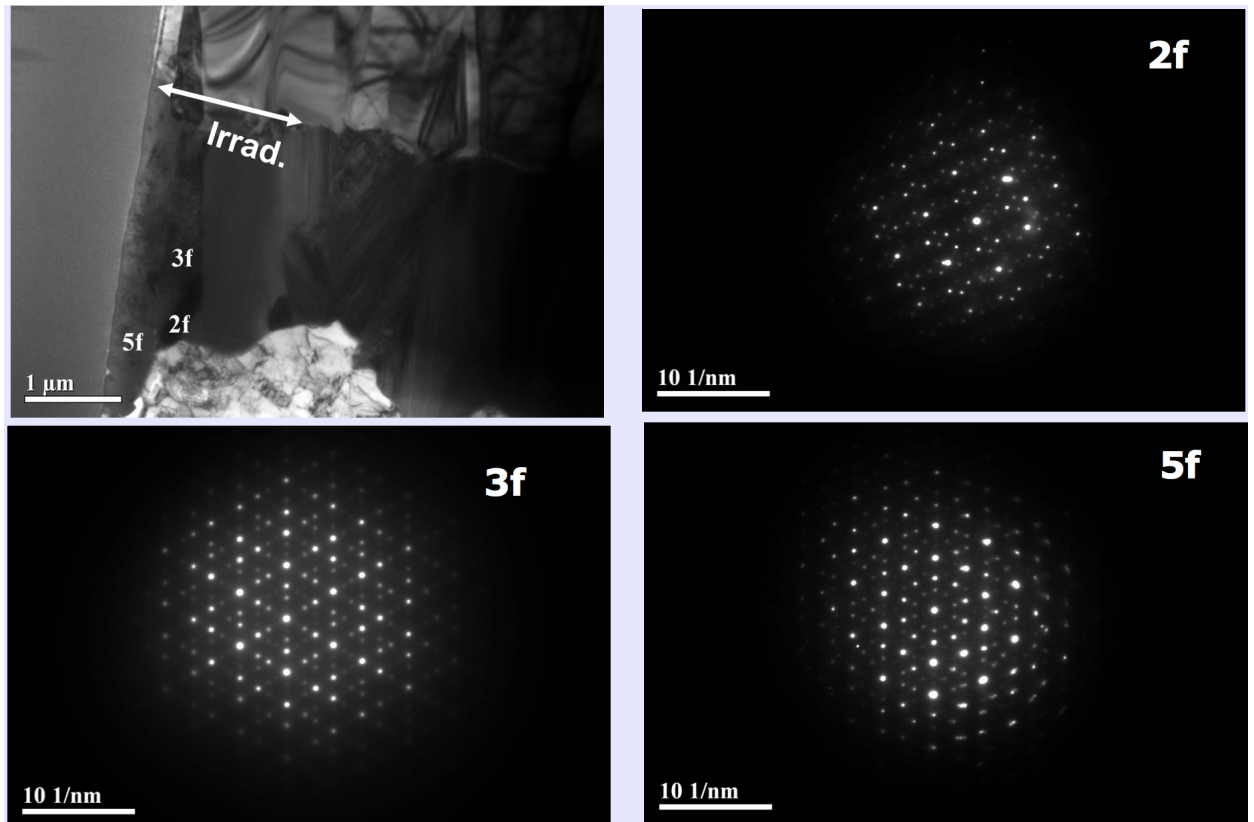
Figure 4.17: Quasicrystal transformation of irradiated Fe_2Mo

4.3.7 New iQC phase discussion

In the previous section, we have shown the transformation of Fe_2Mo phase to icosahedral quasicrystals for the first time. It has been reported by Knapp et al. and Lilienfield et al. back in 1985, the iQC is formed after 400 keV Xe irradiation. With similar Fe-Mo system, Liu et al. observed the iQC after anneal at 760°C following Ar ion irradiation. Most of experiments, however, were done in the multi-layered and amorphous structures by so-called ion beam mixing. The direct iQC transformation under ion irradiation in bulk materials, especially in Fe-Mo alloys, has never been reported. We have observed two FCC structures formed in both Fe_2Mo, and Fe_7Mo_6 phases after annealing at 850°C, and another FCC structure

is observed in the Fe-Mo diffusion couple annealed at 650°C. There is only one phase formed upon 650°C annealing which doesn't have enough thermal budget for diffusion reaction take place. The crystal structure of the intermetallic phase formed at lower temperature, in this case 650°C, shows the same FCC structure with lattice parameter of 0.74 nm. Even the composition is not stoichiometrically the same, but it reveals the consistency in microstructure evolution. It has been shown in the past that Fe_2Mo phase can be formed upon processing in the variety of steels. Fig. 4.18 is the BF-TEM micrographs and corresponding SAD patterns of the Fe_2Mo phase, which shows the HCP structure. What we believe that it is related to the presence of impurities, such as carbon, oxygen, and silicon.

(a) Fe_2Mo phase in steel

(b) SAD pattern of Fe_2Mo
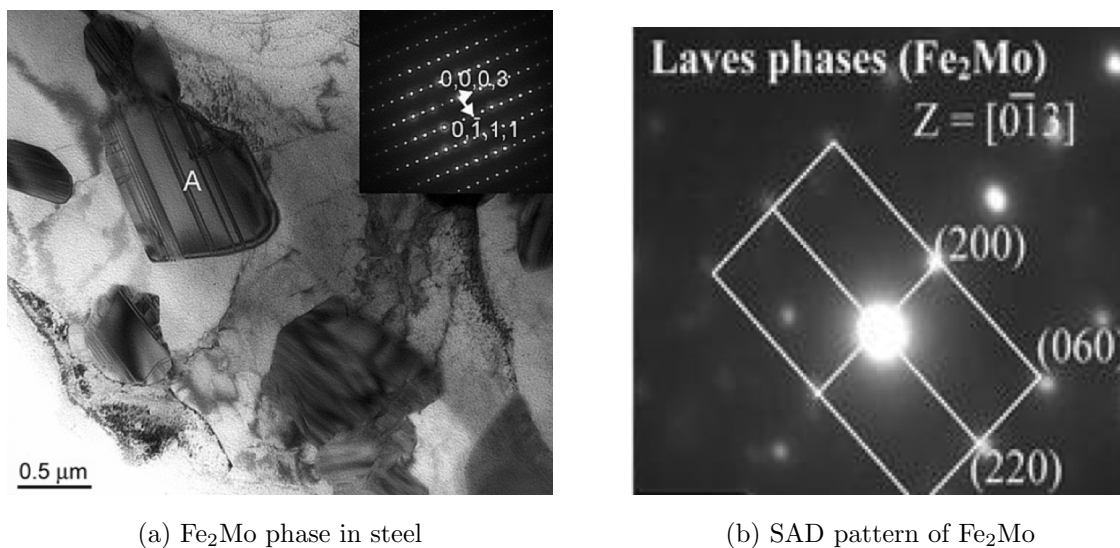
Figure 4.18: BF-TEM and corresponding SAD of Fe_2Mo phase in steels

The face-centered cubic structure is one type approximant to the icosahedral quasicrystals, which has been reported by Kuo et al. and Luo et al. The approximant refers to a crystal structure possesses similar building cluster to the corresponding

iQC. As shown in Fig. 4.15a, the SAD pattern of Fe_2Mo is taken along the [011] zone axis. If we compare the SAD patterns with the iQC along 5-fold (5f) axis, strong diffraction dots along the [011] axis shows similarity of 5f symmetry. However, the mechanism governing the approximant formation in Fe-Mo system has not been clarified. Early approaches used to verify the intermetallics of Fe-Mo phase diagram were mainly arc melting. The presence of oxygen, as impurities, during processing could be the reason that stabilized HCP crystal structure of Fe_2Mo phase. In this manner, Heijwegen and Rawlings et al. did not observe the Fe_2Mo phase using diffusion couple technique at the relatively lower temperature, comparing to the arc melting method. As for the thermodynamic stability, the entropy difference is in favor of FCC structure at elevated temperatures. After annealing, the quench process could freeze the high temperature FCC phase. Furthermore, heavy ion irradiation creates damage cascades and leads to locally thermal spike within the picoseconds range. The whole process of damage cascades formation take place in extremely short of time, which equals to rapid cooling of the Fe_2Mo crystal structure. The rapid cooling process could be the possible explanation that forming the iQC due to heavy ion irradiation. In addition, ion irradiation may take the Fe_2Mo with FCC structure far away from the equilibrium. The phase transformation following ion irradiation may end with lower energy state, in this case the iQC, reported by Lennard-Jones potential. It is of interest to conduct more systematic studies, especially theoretically simulation, for a better understanding of the formation mechanism.

4.3.8 Defect development for Fe and Mo matrix

Followed by the discussion on irradiation induced iQC transformation, Fig. 4.19 is the BF-TEM of irradiated region, including Fe and Mo matrix. Enlarged BF-TEM micrograph of irradiated Fe_7Mo_6 is shown in Fig. 4.16 (b). There is no clear

evidence of voids or dislocation observed. Furthermore, the crystal structure after irradiation remains the same according to SAD analysis in Fig. 4.19. In addition to the interaction layer, overview BF-TEM micrographs of irradiated Fe and Mo from the near surface region are shown in Fig. 4.19 (c) and (d), respectively. Larger voids and dislocation are observed in the Fe grain, which are primarily caused by irradiation, and no voids have been observed in the unirradiated region.In contrast, Mo is featured with evenly distributed but smaller voids, white arrows highlight the noticeable voids. Fig. 4.19 (d) shows the void-denuded region near the grain boundary just below the surface.
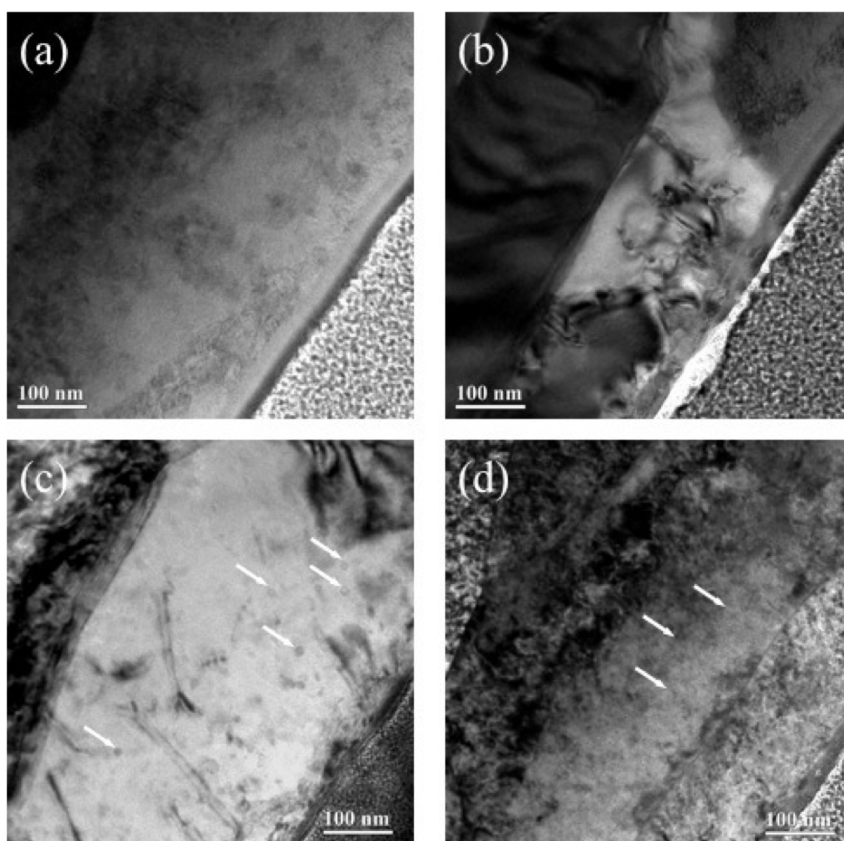
Figure 4.19: Bright-field TE micrographs of (a) Fe_2Mo and (b) Fe_7Mo_6 , and higher magnification micrographs of voids formed in (c) Fe and (d) Mo. White arrows identify position of the representative voids.

5. URANIUM-BEARING DIFFUSION SYSTEMS[*]

The current section consists of previous experimental attempt in understanding fuel-cladding chemical interaction (FCCI), especially focuses on uranium/iron and uranium/nickel. Thermally-activated diffusion couples were prepared with a series of temperatures. The goal of this set of diffusion couples is to study diffusion kinetics and composition profile at the interaction layers. The interdiffusion coefficients and activation energy will be discussed upon each phase in order to support computational and theoretical studies. Another essential point, radiation enhanced diffusion (RED) must also be concerned during normal reactor operation. It has a strong impact on predicting the fuel performance. The energetic neutrons and fission products will cause the system far from equilibrium compared to thermal-activated process. In this section, two different types of ion irradiation were carried out to study damage accumulation and provide evidence of RED. In addition, grain boundaries (GB) have been considered as an important role in the diffusion mechanism and further research of interdiffusion coefficient may include the GB effect.

Three major investigation will be presented in the following sections : 1) the uranium diffusion couple- polycrystalline iron. U/Fe assembly will be annealed at 700°C for 4days followed by helium (He) irradiation. SEM and TEM will be carried out to study the radiation effects and microstructure evolution. 2) the uranium diffusion couple- single crystalline iron and nickel. U/Fe and U/Ni diffusion couples will be characterized to study the kinetics at varies temperatures. 3) the uranium diffusion couple- thin film deposition. Multiple specimens were characterized using Rutherford Backscattering Spectrometry (RBS) to study radiation enhanced diffusion and radiation induced phase formation.

---

[*]Parts of this section are reprinted with permission from "Radiation effects on interface reactions of U/Fe, U/(Fe+Cr), and U/(Fe+Cr+Ni)" by Shao et al., 2015. Journal of Nuclear Materials, 456, 302-310, Copyright[2015] by Elsevier

5.1 Background of fuel cladding chemical interaction with Uranium-based fuel alloys

There have been a number of programs, such as the Fuel Cycle Research and Development (FCRD), the Advanced Fuel Cycle Initiative (AFCI) and the Global Nuclear Energy Partnership (GNEP), supporting the investigation on primary nuclear challenges. Major contributions have been made to achieve higher burn up by improving the fuel performance. Consequently, the increasing damage accumulation will cause excessive swelling in both fuel rods and structural materials. Once the fuel pins is in contact with the cladding, intermetallic phases with low-melting temperature and poor mechanical properties will form due to the interdiffusion[87, 121, 51, 53, 52, 147, 65]. Experimental and theoretical approaches are required to address the unknown in fuel cladding chemical interaction. FCCI has the serious impact to the reactor safety due to the degradation in structural materials and coolant can breach into the fuel pins cause reactor failure[137, 106, 142, 46].
.

To help clarify how to mitigate the FCCI, efforts have been made on two major directions : 1) study the interdiffusion products between metallic fuels and cladding materials. 2) select possible diffusion barrier elements to delay the process. The former provides direct observation of intermetallics formation. Uranium based fuel alloys, with addition of molybdenum and zirconium, were assembled against cladding materials such as, T91, HT9 farretic/martensitic steels (FMS)[68, 48, 133, 127]. The later focused on implementing potential liner materials onto the cladding surface. Vanadium, Zirconium and Chromium coatings have effectively decreased the pene-

tration depth of the fuel elements and fission products[29, 21]. Complex phases were usually observed in the previous studies due to the chemical compositions in fuel and cladding materials[86, 72, 110, 66, 11, 19, 148]. Recently, binary diffusion systems have been tested upon key components of FCCI, such as Uranium, Plutonium, Iron, Zirconium, and Nickel[59, 2, 37, 93, 125, 109, 28]. The simplified diffusion couples demonstrate better resolution in characterizing phase formation and microstructure evolution. However, detailed information of each phase formation is insufficient in developing advanced structural materials, such as iron-based alloys and nickel-based alloys against uranium metallic fuel[45, 115, 69, 128, 70, 18, 98]. Moreover, it is of also great importance to have reliable interatomic potentials based on experiments that facilitate atomic simulation. Microsctrural information and kinetic data, of each phase formed by thermally-activated diffusion couple will be beneficial for multiscale modeling in fuel design[29, 21].

5.2 Uranium diffusion couples – polycrystalline iron

In this section, poly-crystalline Uranium is assembled with poly-crystalline iron to form thermally-activated diffusion couple. Complete experimental procedures are listed in the chapter 3. Specimen was annealed for 4 days at $700°C$ to avoid eutectic transformation. Fig. 5.1 is the equilibrium phase diagram of Uranium and Iron. Two phases are reffered as UFe_2 and U_6Fe. In brief, UFe_2 has face-centered-cubic crystal structure with lattice parameter of 7.5Åand U_6Fe takes tetragonal crystal structure. More importantly, uranium transformation is not involved in the following diffusion couple experiments. Highlight of the U/Fe polycrystalline diffusion couple : we have reported the kinetic data upon annealing at $700°C$; post-irradiation analysis of each phase reveals the damage accumulation by 2 MeV helium ions; transmission electron microscope (TEM) was conducted to study helium bubble formation.
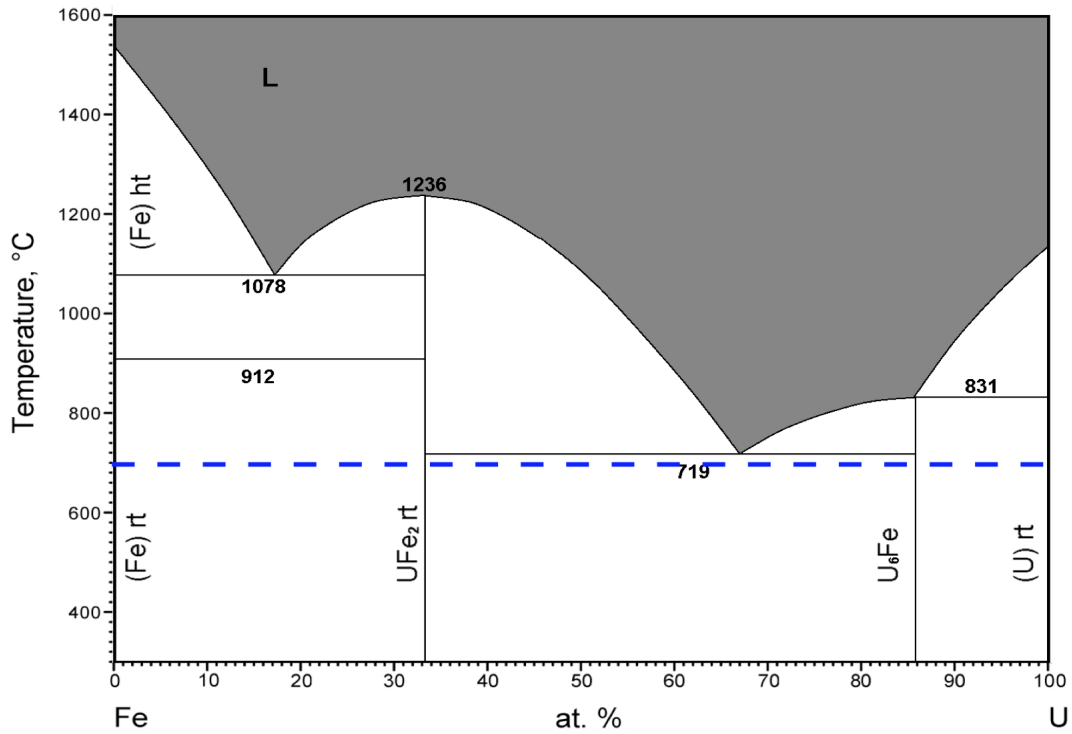
Figure 5.1: Phase diagram of U–Fe

5.2.1 Phase identification and diffusion kinetics

After annealing, U/Fe diffusion couple is cut and polished prior to scanning electron microscope (SEM) and energy dispersive x-ray spectrometry (EDS) characterization. Fig. 5.2a is a typical back-scattered electron (BSE) micrograph of as-annealed U/Fe couple. Four phases were identified, from left to right, as U, U_6Fe, UFe_2 and Fe, respectively. The EDS line-scan spectrum in Fig. 5.2b confirms the chemical composition (at%) of the two phases formed at interaction region. The thermal-kinetic data of can be extrapolated from the EDS line scan via Eq. 2.6. Phase U_6Fe has the diffusion length of 60 μm and phase UFe_2 has roughly 10 μm. The $\tilde{D}$ of each phase are listed in Table 5.1
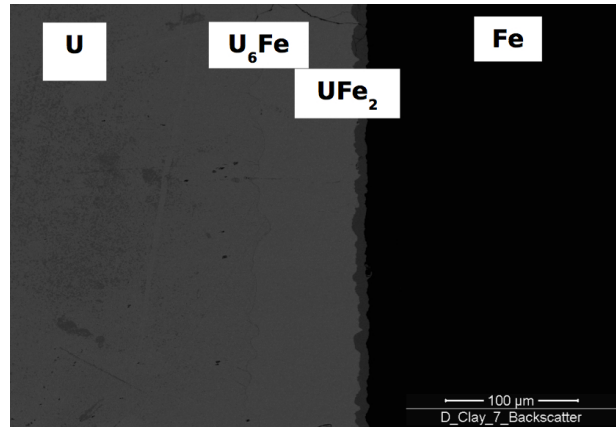
(a) BSE micrograph of U– Fe couple
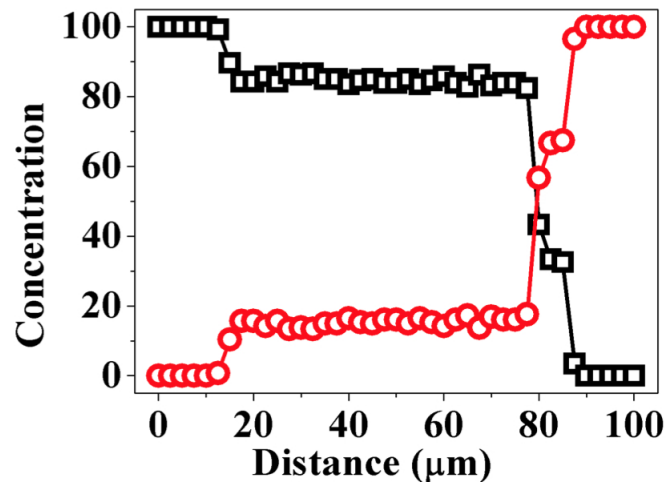
(b) Composition profiles of U – Fe couple

Figure 5.2: U – Fe diffusion couple annealed at 700°C for 4 days

Table 5.1: Extracted integrated diffusion coefficients of U vs Fe

$\tilde{D}$ U$_6$Fe (at. frac. m^2/s)	$\tilde{D}$ UFe$_2$ (at. frac. m^2/s)
3.31 x 10^{-16}	1.89 x 10^{-16}

The annealed U/Fe diffusion couple was irradiated with 2MeV He ions to 1 displacement per atom (dpa) at 450 °C. The vacuum was kept under 10^{-6} torr and the temperature was monitored within 1% variation throughout the irradiation. The depth profile of injected He was plotted in Fig. 5.3 using SRIM calculation with full-cascade option. Peak helium concentration is located at $\sim 3.2\ \mu$m below surface. Cross-sectional TEM specimen was prepared using focused ion beam (FIB) lift-out method.
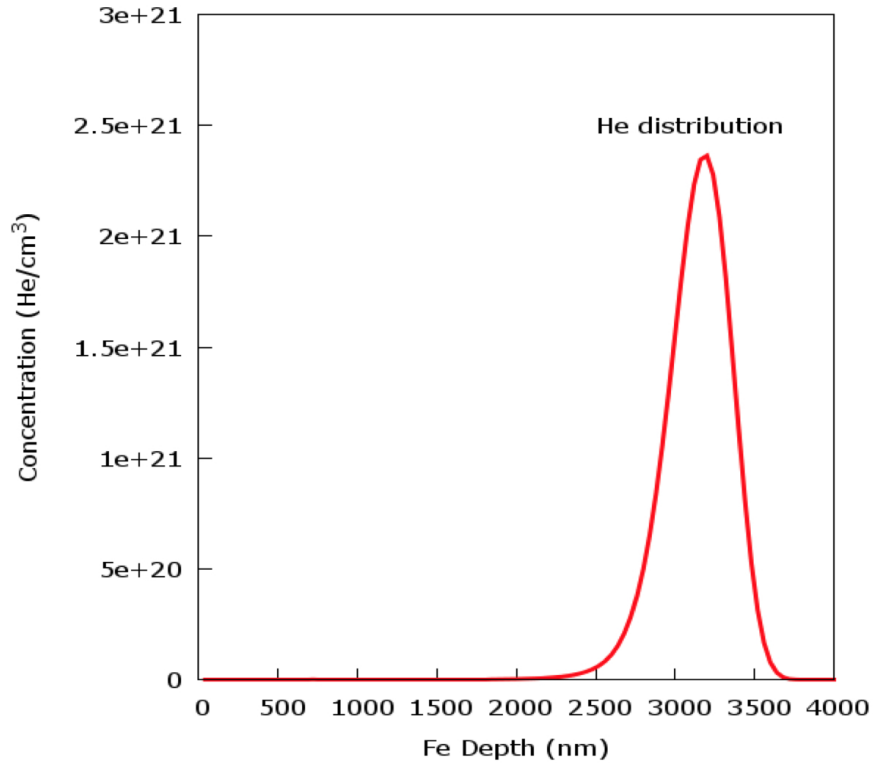
Figure 5.3: Experimental condition – 2 MeV He distribution

5.2.3   Post-irradiation characterization

Fig. 5.4 is the scanning transmission electron (STEM) micrograph of the cross-sectional U/Fe diffusion couple. The overall morphology at the interaction layer shows ununiformity which suggests complex phase may form during annealing. The findings from Fig. 5.4 are summerized as follows. Firstly, a band of black dots was observed across the specimen at roughly 3 μm below the surface. The black dots in the STEM indicate the empty volume in the specimen and we believe that is cause by injected helium accumulation. There seems to be some variation of helium bubble size and density in each phase and detail will be discussed in later sections.

Secondly, EDS analysis reveals the chemical composition of the intermetallics formed at the interdiffusion region. According to quantified composition, the interdiffusion region consists a mixture of U_6Fe, UFe_2 and UO_2. The diffusion length of UFe_2 was measured as 12 μm compared to the SEM results. And yet UO_2 phase was formed during diffusion couple assembly with possible oxidation on the uranium disk. The unexpected oxidation became a diffusion barrier which explains why ununiform phase formed at the interaction layer. In addition, a band of helium bubbles was observed at the depth roughly 3 μm below surface, which matches with the SRIM calculation. However, the bubble size varies along with different phase formed throughout the interdiffusion zone.
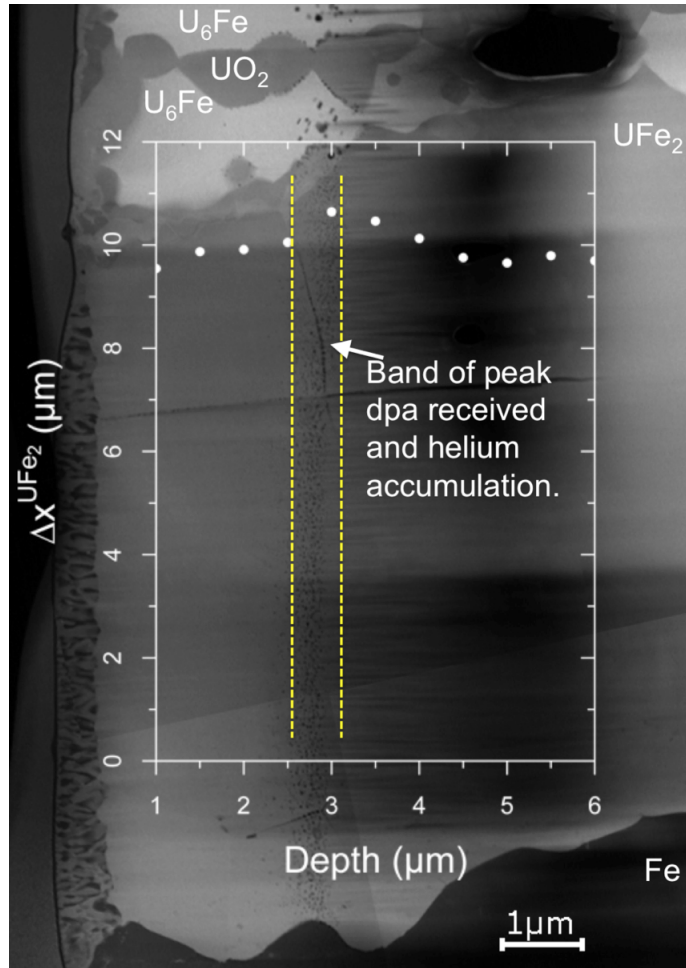
Figure 5.4: Helium accumulation in DU–Fe diffusion couple.

Fig. 5.5 shows a STEM micrograph with lower magnification and yellow-dash line is denoted to the helium peak accumulation. The U_6Fe phase seems to contain relatively large size of helium bubbles and the island-like UO_2 phase can be seen along the interface. Further crystal structure characterization was carried out by using selected area diffraction (SAD) patterns. Five areas of interest were marked as A- E, and corresponding SAD patterns were indexed below. The dark matrix on the left is iron, which has relatively lower atomic number. The phase next to iron

is well-indexed as UFe_2 with FCC crystal structure. Oxide materials usually have darker contrast in the STEM micrograph and SAD pattern of area D is referred as UO_2 phase. U_6Fe phase were indexed from the area C and E,which is surrounding the island-like UO_2 phase.
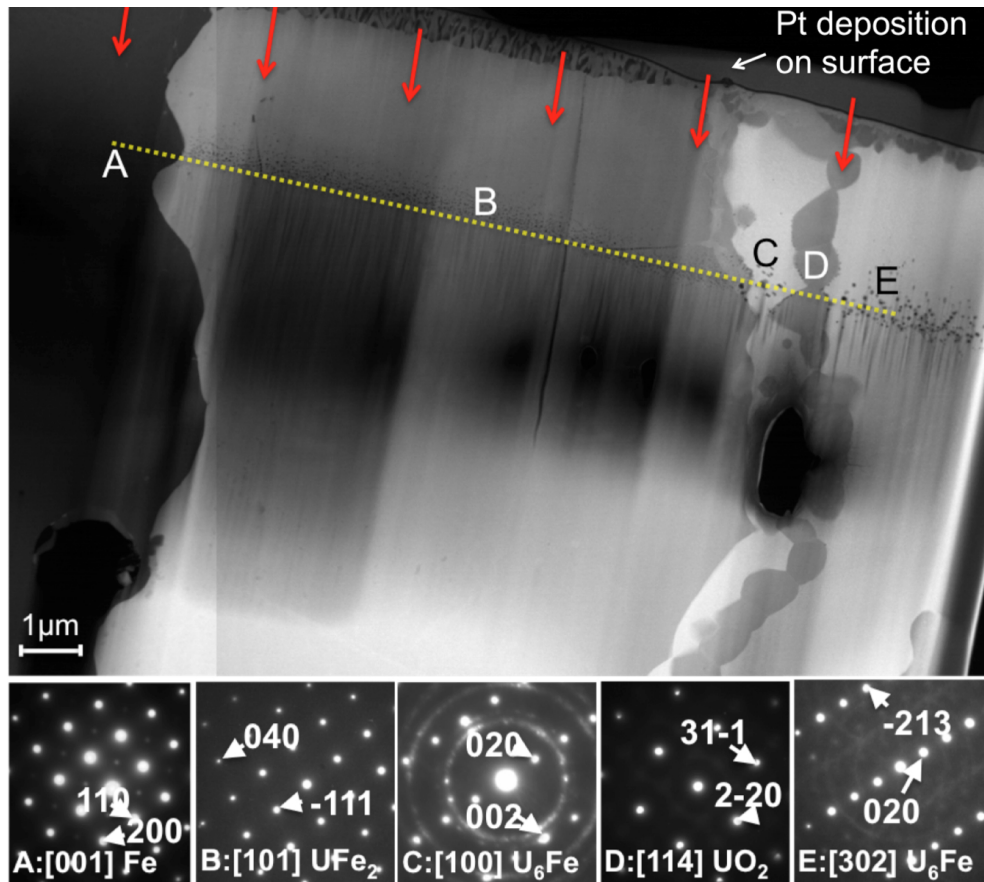
Figure 5.5: Microstructure of the intermetallic compounds – SAD patterns.

Post-irradiation BF-TEM micrographs from each phase are shown in Fig. 5.6. Pure uranium phase is not covered in this section due to the width limit of FIB preparation. A long the depth of helium accumulation, it is subjected to investigate helium bubbles developed in each phase. Region A was taken from the U_6Fe phase.

The area is not quite electron transparent due to the higher uranium content. The diameter of the helium bubbles in the U_6Fe phase is ranging from 50 to 80 nm. Region B represents the UO_2 phase and contains smallest helium bubbles with averaging 20 nm in diameter. The helium bubbles appear to have a wide size distribution in the UFe_2 phase. As shown in region C, the diameter of helium bubbles ranges from 20nm to 80nm. Also, small helium bubbles tend to move to each other and form medium size bubbles. Same happens to the medium helium bubbles. Additionally, helium bubbles are observed to decorate at grain boundaries in the UFe_2 phase. In contrast to the UFe_2 phase, relatively larger helium bubbles were observed, which indicates helium is more mobile, in the U_6Fe phase. On the other hand, the bubbles in the UO_2 phase are the smallest in diameter but with highest density. Region D shows the helium bubbles distribution in the pure iron area.

To sum up, we have demonstrated an effective way to study FCCI with combined radiation effect. With the diffusion couple technique, U/Fe phase diagram is verified. Interdiffusion coefficients of U_6Fe and UFe_2 are extracted after 700°C annealing. The radiation effect, such as swelling behavior, is studied for each phase formed at the interaction layer. Oxygen should be avoided throughout the sample preparation to minimize the surface oxidation, which alter the diffusion length and block the path. Next session will be focus on single crystalline iron with three sets of elevated temperatures. The kinetics and activation energy will be discussed.
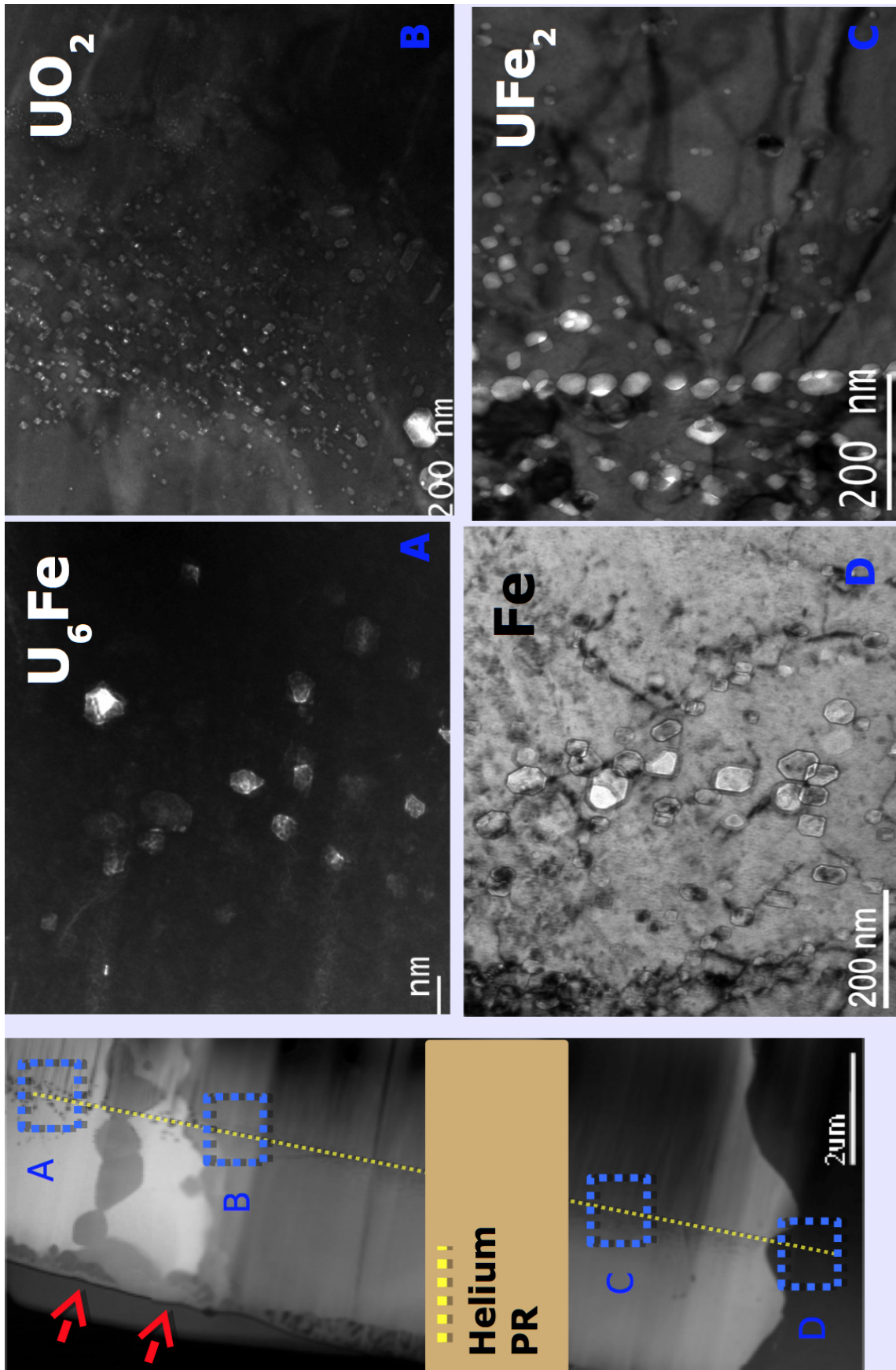
Figure 5.6: Microstructure evolution in DU–Fe diffusion couple.

5.3   Uranium diffusion couples – single crystalline iron

In this section, single crystalline iron will be assembled with poly-crystalline uranium to form diffusion couples. The temperatures selected for annealing is marked as red window in Fig. 5.7. Similarly, eutectic temperature is avoided and no uranium transformation is involved. Complete experimental procedures are listed in the chapter 3. The U/Fe diffusion couples were annealed at 575°C, 600°C, and 625°C for 7 days, 6days, and 5days, respectively.
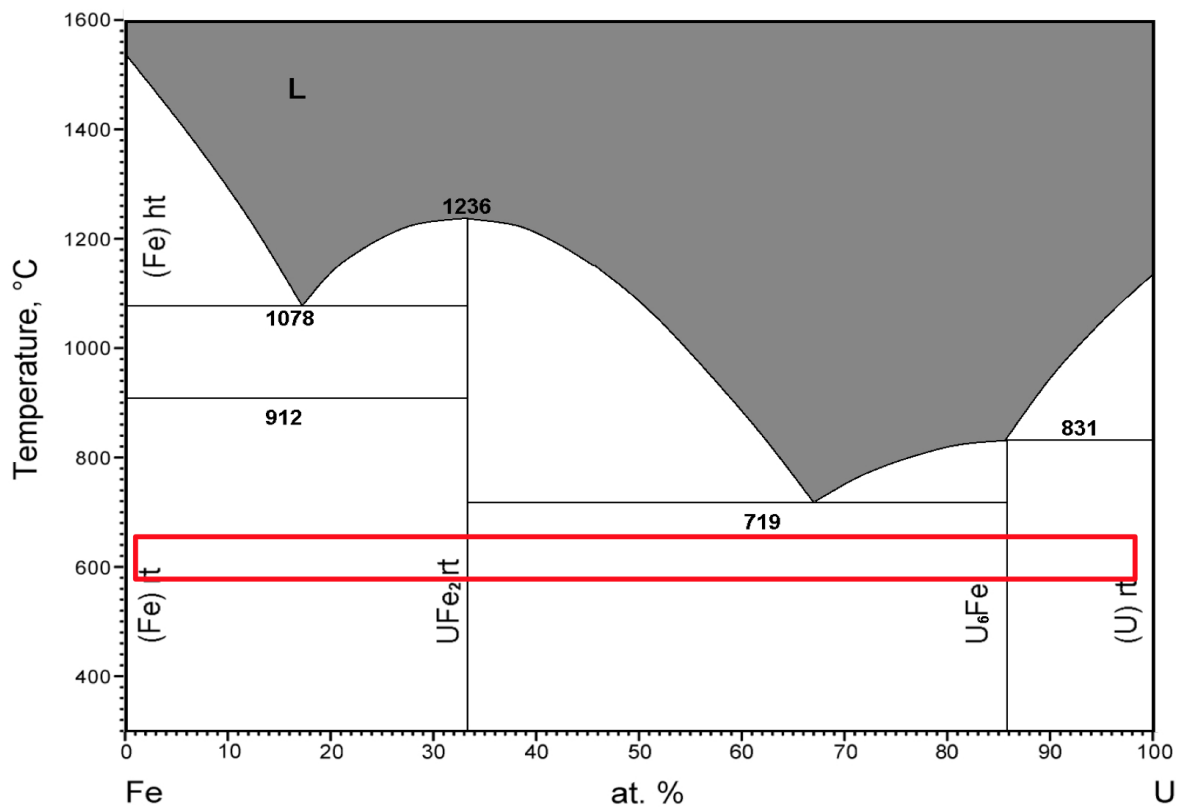
Figure 5.7: Phase diagram of U–Fe.

5.3.1   Thermal-kinetics of as-annealed U/Fe diffusion couple

After annealing, each diffusion couples were cut in half and polished for further SEM characterization. EDS line scans were carried out on U_6Fe and UFe_2 phases upon each annealing temperatures. Two equilibrium phases were present at each annealing temperature and matched the stoichiometry from the U-Fe phase diagram. Next, the width of each phase formed at the interaction layer will be measured. The integrated interdifusion coefficients were calculated by using Eq. 2.6, and $\tilde{D}$ of each phase are listed in Table 5.2. More importantly, Eq. 2.7 is used to extrapolated the activation energy of each phase, which is essential for modeling to describe the barrier of atomic movement. The activation energy Q of each phase in the U/Fe diffusion couples is listed in Table 5.3

Table 5.2: Extracted integrated diffusion coefficients of U vs Fe

Temperature (°C)	$\tilde{D}$ U_6Fe (at. frac. m^2/s)	$\tilde{D}$ UFe_2 (at. frac. m^2/s)
575	2.71 x 10^{-18}	9.9 x 10^{-20}
600	2.34 x 10^{-17}	1.35 x 10^{-18}
625	1.45 x 10^{-16}	9.33 x 10^{-18}

Table 5.3: Activation energy of U_6Fe and UFe_2

Q U_6Fe (KJ/mol)	Q UFe_2 (KJ/mol)
416.5	449.5

In comparison, Fig. 5.8 plotted the interdiffusion coefficient of U/single-crystalline iron couples against U/poly-crystalline iron couples. Sohn et al. [63, 49]reported the interdiffusion coefficients between uranium and poly-crystalline iron, similar technique was used but annealed at 580°C, 615°C, and 650°C[50]. The red and black dash line are replotted from previous study and represent the U_6Fe and UFe_2 phase, respectively. In the same way, solid lines were acquired in this study and denoted to U_6Fe and UFe_2 phase, respectively.

The interdiffusion coefficients in poly-crystalline specimens are an order of magnitude higher than those in single-crystalline specimens. Grain boundaries (GB) provide additional path for diffusion in the poly-crystalline materials. While this is the case, the uranium diffuses faster in the poly-crystalline iron even with shorter annealing period , which means less thermal budget. According to Table. 5.3, U_6Fe phase has lower activation energy which indicates it diffuses faster. As a result, the U_6Fe phase formed wider at the interaction layer. Also, the interdiffusion coefficients of U_6Fe and UFe_2 phase show the same trend in both single crystalline and poly-crystalline couples.
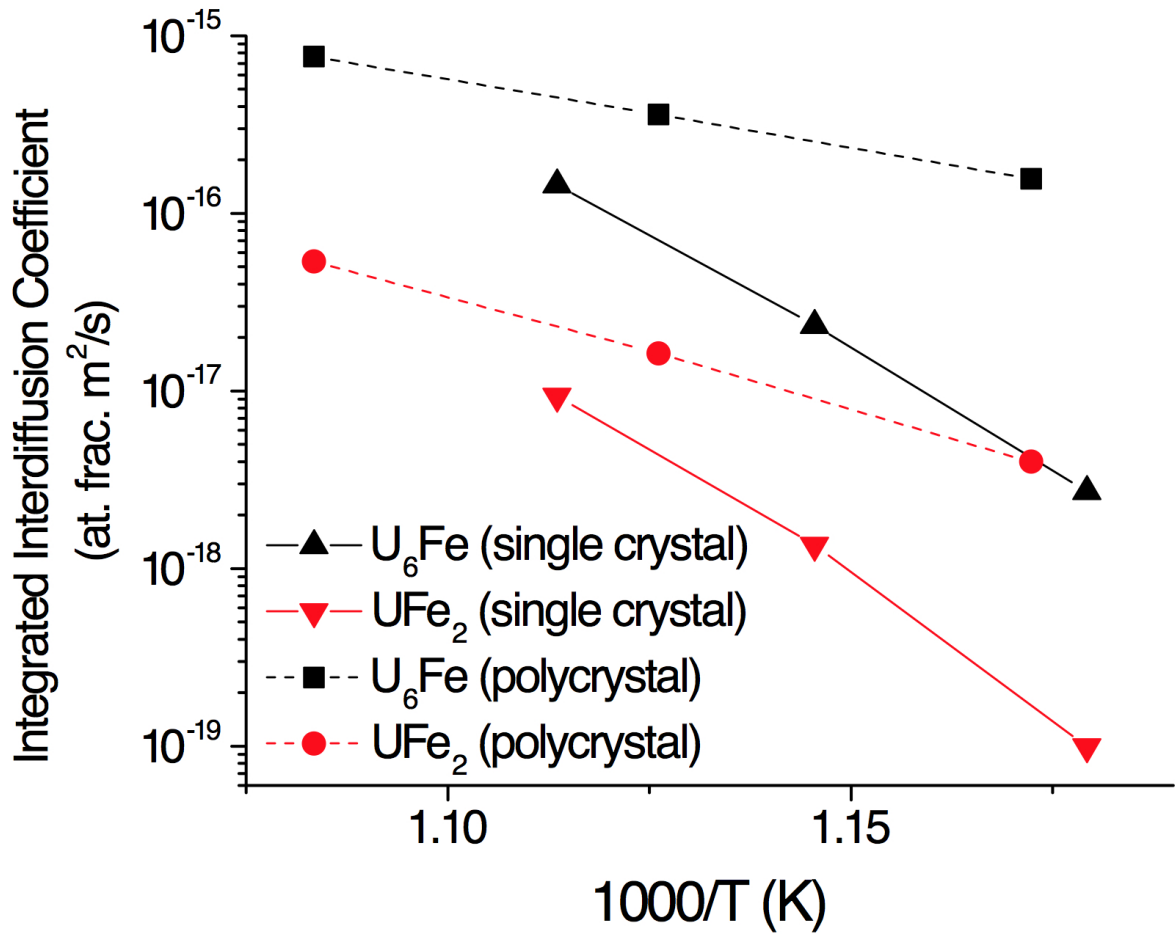
Figure 5.8: Integrated interdiffusion coefficient : single crystalline vs poly-crystalline.

5.3.2 Radiation enhanced diffusion in U/Fe single-crystalline diffusion couple

In addition to kinetics study, He implantation was performed to investigate radiation effects upon diffusion. In this section, U/Fe single crystalline diffusion couple was annealed at 625°C for 5 days. After annealing, specimen were cut in half to avoid surface oxidation/contamination. Prior to irradiation, sectioned specimen were polished down to micrometer suspension to remove surface roughness. The inset of FIg. 5.9a is the typical backscattered SEM(BS-SEM) micrograph from as-annealed U/Fe diffusion couple . BS-SEM micrograph indicates that two phases were formed at the

interdiffusion region. EDS line scans were carried out across the bulk materials and the interface. According to Fig. 5.9a, two phases were identified as U_6Fe and UFe_2. The width of the U_6Fe phase is measured to be $\sim 20\mu m$ at the interaction layer and the UFe_2 phase has diffused $\sim 3\mu m$.

The U/Fe diffusion couple were then irradiated with 2 MeV He ions at 450°C to 1 displacement per atom. The vacuum was kept under 10^{-6} torr during irradiation. The temperature was controlled less than 1% variation.The incoming He ions were perpendicular to the interface. Post-irradiation analysis were performed using SEM and EDS in comparison with as-annealed samples. The inset of Fig. 5.9b is the BS-SEM micrograph of post-irradiated specimen. The EDS line scan were plotted in Fig. 5.9b and the profiles shows enhanced diffusion in both phases after irradiation. The width of U_6Fe phase increased to $\sim 27\mu m$, while the UFe_2 only increased to $4\mu m$. The helium irradiation cause the U_6Fe and UFe_2 phase diffused 35% and 25% more, respectively. This section has provided the evidence that radiation enhanced diffusion can be studied by using diffusion couple technique. The enhanced diffusion length can offer insights to support computational modeling through various temperatures and He energy.

(a) As-annealed U – SCFe couple

(b) 2 MeV He irradiated U – SCFe
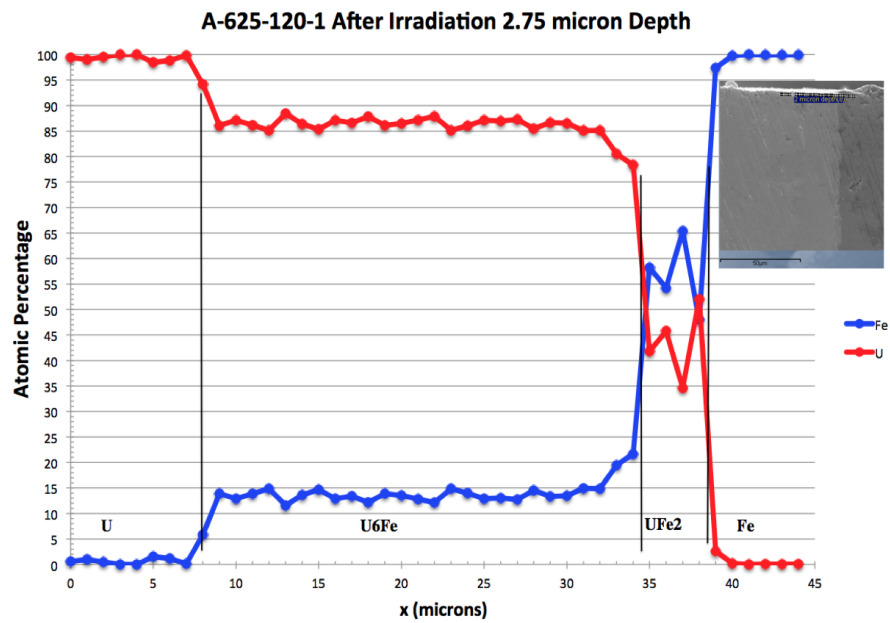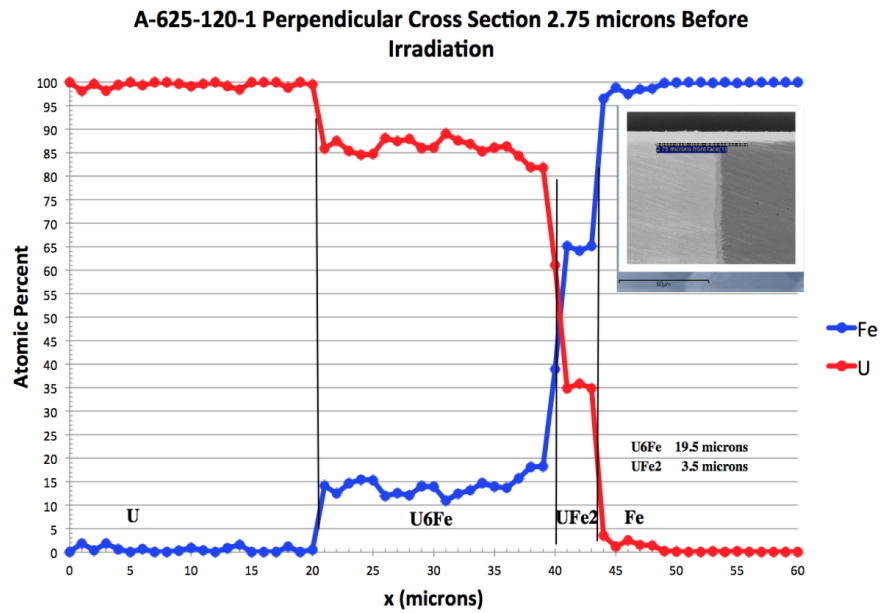
Figure 5.9: Corresponding EDS profiles of U (red) and SCFe (blue) distributions at 625°C for 5 days

5.4 Uranium diffusion couples – single crystalline nickel

Nickel plays a significant role in cladding materials, especially the austenitic steel used for current boiling water reactor (BWR). In the presence of nickel, high temperature operation and better corrosion resistance can also be achieved for the advanced reactor application. Fig. 5.10 is the uranium/nickel phase diagram, and there are seven equilibrium phases including UNi_5, $U_{0.22}Ni_{0.78}$, $U_{0.23}Ni_{0.77}$, UNi_2, $U_{11}Ni_{16}$, U_7Ni_9 and U_6Ni. Kimmel et al. [73] has investigated growth kinetics using nickel plated uranium and only three phases were observed after annealing at 600°C for four days. Steinegger et al. [1] also reported six intermetallic phase formed using vacuum cast. Nickel has also been considered as the diffusion barrier in-between fuel and cladding materials. However, the fundamentals of nickel or nickel-based alloys upon FCCI are quite limited. This section will be focused on the interdiffusion between uranium and single-crystalline nickel. Single-crystalline nickel were assembled with uranium, then annealed at 675°C, 700°C, and 725°C for 15 days, 13 days and 11 days, respectively. Fig. 5.10 is the uranium/nickel phase diagram, and eutectic temperature was avoided in these U/Ni diffusion couples.
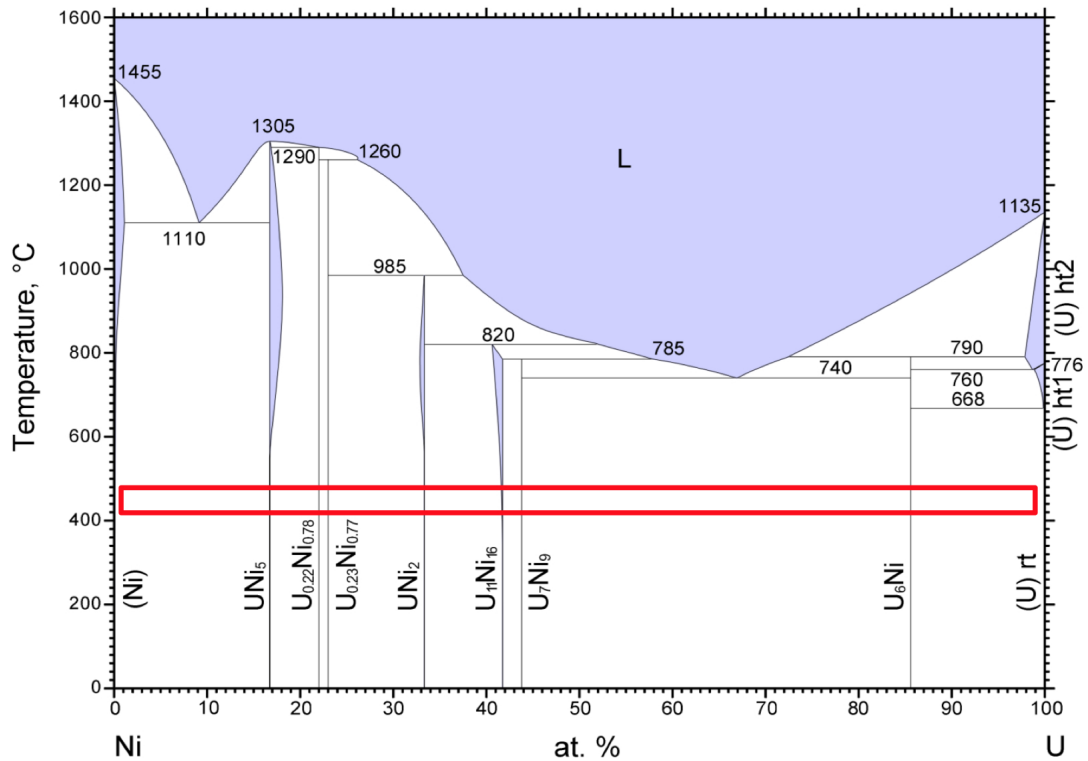
Figure 5.10: Phase diagram of U–Ni.

Scanning electron microscope (SEM) and energy dispersive X-ray spectrometry (EDS) were carried out to investigate the intermetallic phase formation. Fig. 5.11a is the typical BSE micrograph of U/Ni diffusion couple annealed at 725°C for 11 days. There seems to be 6 phases formed at the interaction layer. The average width of each phase is measured by using built-in function of the post-image process. Fig. 5.11b shows the enhanced contrast of the original BSE micrograph. Hence, 7 phases are revealed and measured. The UNi_5 phase has the largest diffusion length, whereas the $U_{11}Ni_{16}$ phase diffused least. Furthermore, EDS line scans were performed across the interaction layer upon three U/Ni diffusion couples. Multiple scans were taken to have better statistics and average EDS profiles were plotted in the following section.
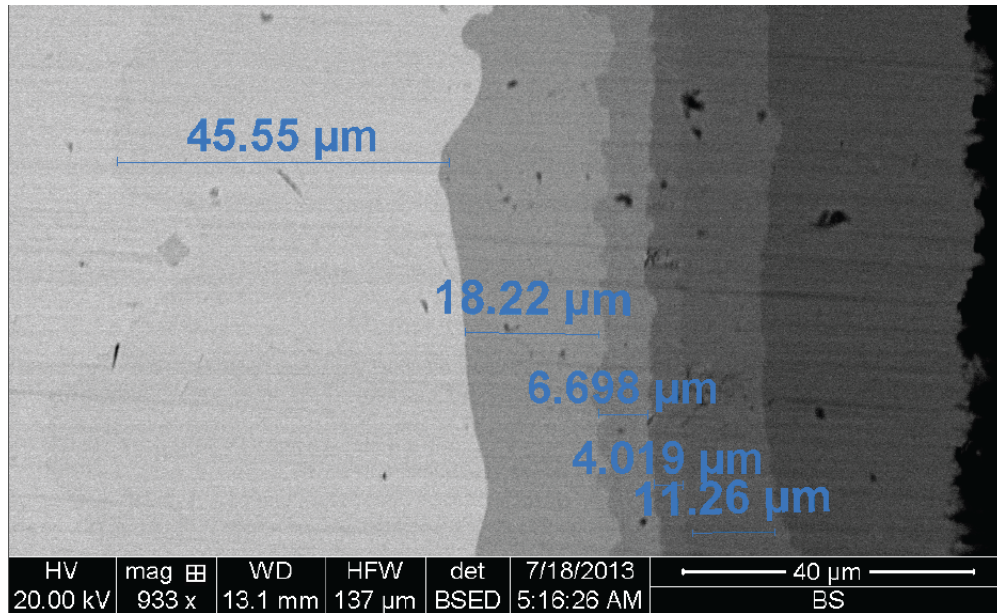
(a) BSE micrograph of U – Ni couple
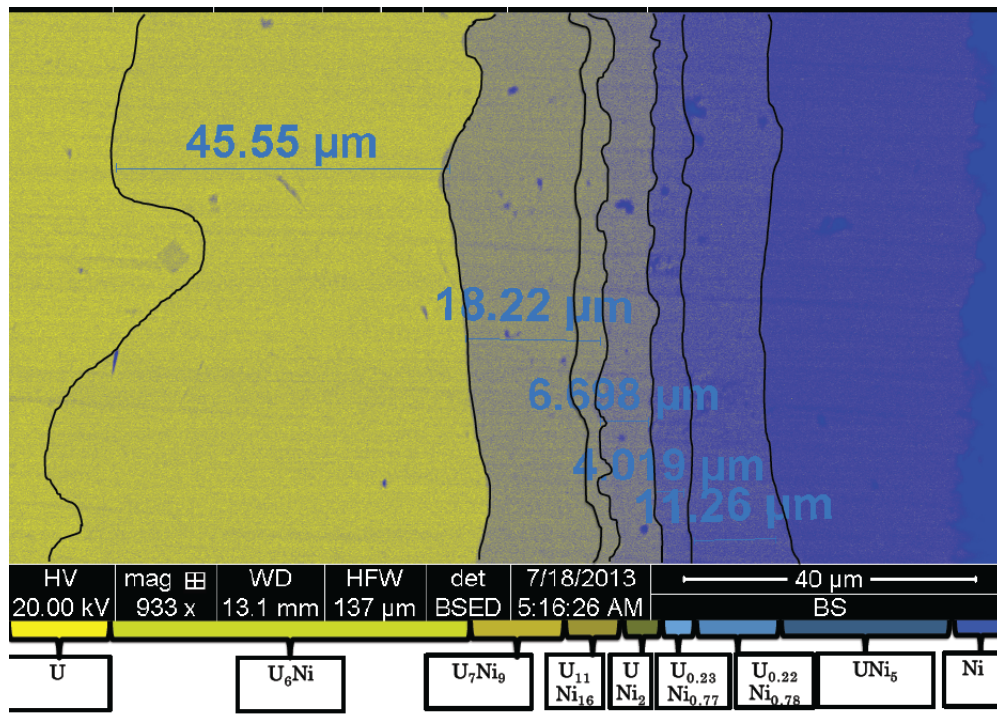
(b) Enhanced contrast BSE micrograph of U – Ni couple

Figure 5.11: U – Ni diffusion couple annealed at 725°C for 11 days

To date, there has been no systematic study of U/Ni intermetallics formation. In this section, we have demonstrated seven U/Ni phases formed by using diffusion couple technique at elevated temperatures, 725°C for 11 days in Fig. 5.11b. In the next session, diffusion couples annealed at 675°C, 700°C, and 725°C will be examined upon intermetallic phase formation and diffusion kinetics. EDS line scans were conducted across the interaction layer for all three U/Ni diffusion couples. Fig. 5.12 shows the composition profiles of each annealing temperature, and the resolution of EDS line scan is 100 nm.

The EDS profile provides the chemical composition (in at%) and diffusion length of each phase. As shown in Fig. 5.12, the step-height spectra indicate that all seven intermetallics were formed throughout three elevated temperatures. Ui_5N phase formed the widest intermetallics upon all the other 6 phases, which is measured to be over 40 μm . As the annealing temperature increased, the U_7Nii_9 phase started to grow faster where the UNi_5 phase is sacrificed. The overall thickness of the interaction layer didn't change but each phase. The details of the phase formation will be discussed in later section on interdiffusion coefficient and activation energy.
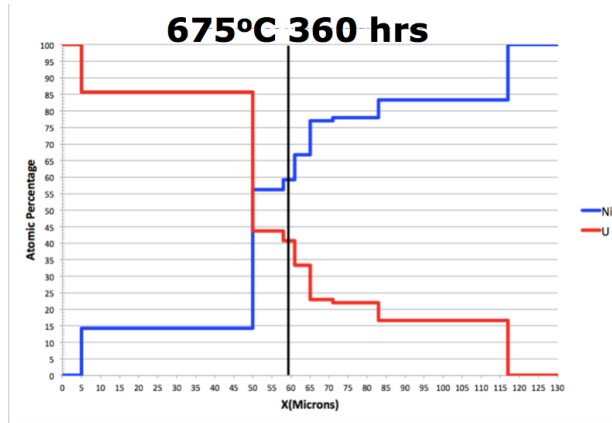
(a) U – SCNi diffusion couple annealed at 675°C
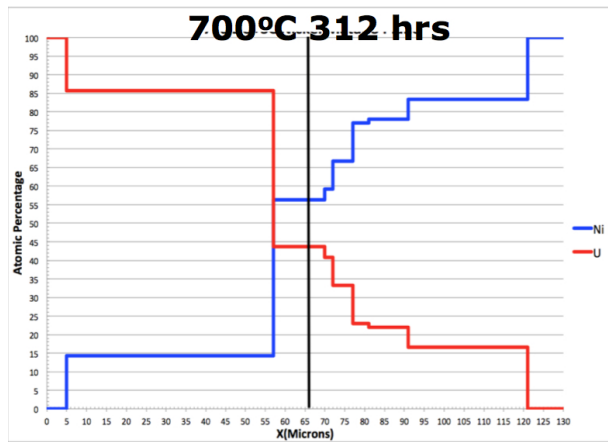
(b) U – SCNi diffusion couple annealed at 700°C
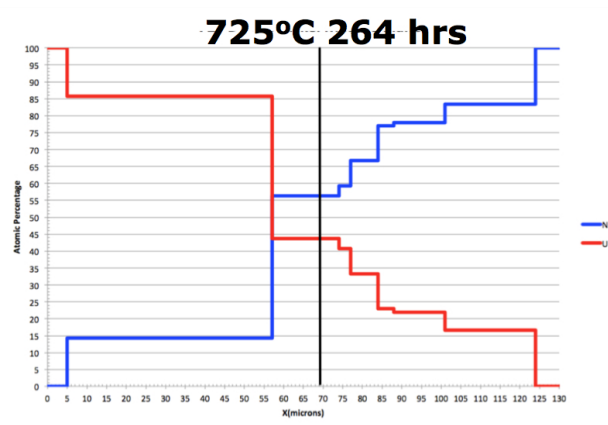
(c) U – SCNi diffusion couple annealed at 725°C

Figure 5.12: Corresponding EDS profiles of U (red) and SCNi (blue) distributions

According to the BS-SEM micrograph and EDS profiles, the diffusion length of each phase were identified. The interdiffusion coefficients of each U/Ni intermetallics were calculated based on Eq. 2.6, and $\tilde{D}$ of each phase are plotted in Fig. 5.13. As a result, by using Eq. 2.7 the activation energy Q of each phase were extracted in Table 5.3. It has a good agreement in trend with Kimmel et al, who previously reported Q of U_6Ni, U_7Ni_9 and UNi_5 phase.

The UNi_5 phase possesses the lowest activation energy, which indicates it diffuses faster compared to other phases. It can be seen that the UNi_5 phase formed a relative wide layer at lower annealing temperature. On the other hand, the U_6Ni phase has second smallest activation energy, however, the widest diffusion length was observed throughout three temperatures. It is worth noting that the diffusion length between the U_7Nii_9 phase and the UNi_5 phase. These two phases have a competing effect during layer growth. As Fig. 5.12 shown, with increasing temperature to 725°C the U_6Ni phase grew thicker while the UNi_5 phase started to shirk. All the phases interact with each other, as well as the growth process. For instance, $U_{0.22}Ni_{0.78}$ phase next to UNi_5 phase also grew thicker at 725°C. Detailed mechanism of the competing effect in each phase is not clear yet, but we have reported the growth kinetics of 7 U/Ni intermetallics for the first time.
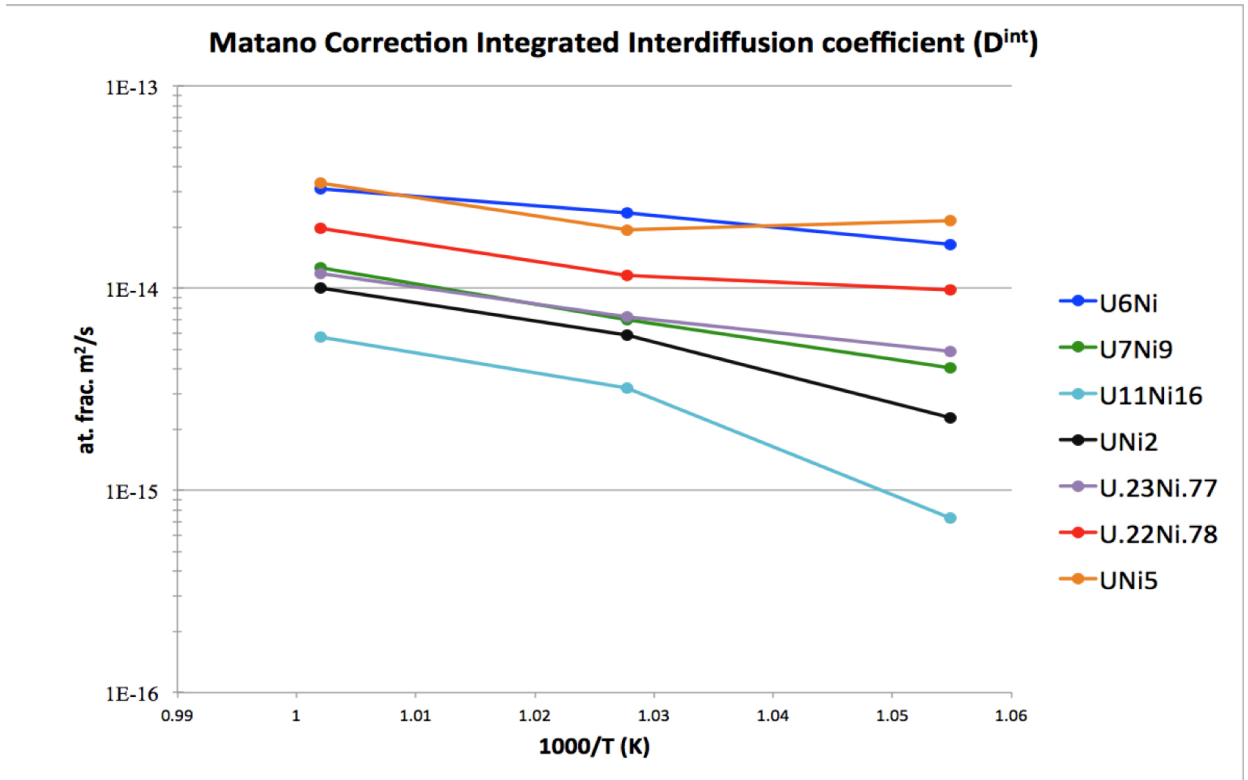
Figure 5.13: Interdiffusion coefficient of U–SCNi couple.

Table 5.4: Activation energy of U/Ni intermetallics

Phase	Q (KJ/mol)
UNi_5	67.1
$U_{0.22}Ni_{0.78}$	110.4
$U_{0.23}Ni_{0.77}$	138.9
UNi_2	232.9
$U_{11}Ni_{16}$	325.2
U_7Ni_9	179.1
U_6Ni	99.2

5.5   Uranium diffusion couples – thin film deposition

In contrast to the solid-solid diffusion technique in previous sections, thin-film deposition was employed to investigate radiation enhanced FCCI. There are several disadvantages of using traditional bulk diffusion couple assembly, especially uranium is involved. Severe surface oxidation, as shown in the previous U/Ni couples, usually leads to poor bonding and rough interaction regions. The oxides formed at the interface would most likely block the diffusion which cause inhomogeneous interaction. Large interface variation was observed due to the poor bonding and crack formation, which is difficult to study the radiation effects consistently. Therefore, physical vapor deposition was employed to achieve highly uniform metal thin-film. The thin-film is independent to the substrate roughness and contains no cavities compared to mechanically bonded diffusion couples. The deposition process was carried out following argon ion etching which effectively reduced the surface oxidation. Detailed deposition procedures are listed in the chapter 3.

Three sets of metal thin-film were deposited onto uranium substrate with alloy composition of Fe(99.9%) , Fe-20wt%Cr and Fe-20wt% Cr-20wt%Ni. The tin-film diffusion couples were then irradiated with 3.5 MeV Fe ions to study radiation enhanced diffusion on FCCI. Fig. 5.14 is the damage profile and injected Fe ions distribution calculated using SRIM code. The SRIM calculation is based on the specimen orientation, which consists the 480nm thin-film and uranium substrate. The interface between thin-film and substrate is denoted to Fe/U. The thin-film diffusion couples were then irradiated to the fluence of 9 x 10^{15} / cm^2. The damage created in the thin-film reaches $\sim$ 10 dpa and $\sim$ 20 dpa in the uranium substrate. Considering the loss of thin-film during irradiation, only a layer of $\sim$ 1.4nm were removed based on sputtering yield calculated by SRIM code. The direct compositional redistribution

can be ignored due to less than ~ 0.05 atomic density change.

In order to investigate radiation effect, two specimens of the same alloy composition were loaded each time. The Fe ion irradiation were carried out at 450°C and 550°C. The control specimen was placed next to the irradiated area but masked, which only thermally-activated diffusion was induced. Diffusion kinetics were characterized by using Rutherford backscattering spectrometry (RBS) with 2 Mev He ion beam to compare before and after ion irradiation. Then, the RBS spectra were fitted with SIMNRA code to extract the composition.
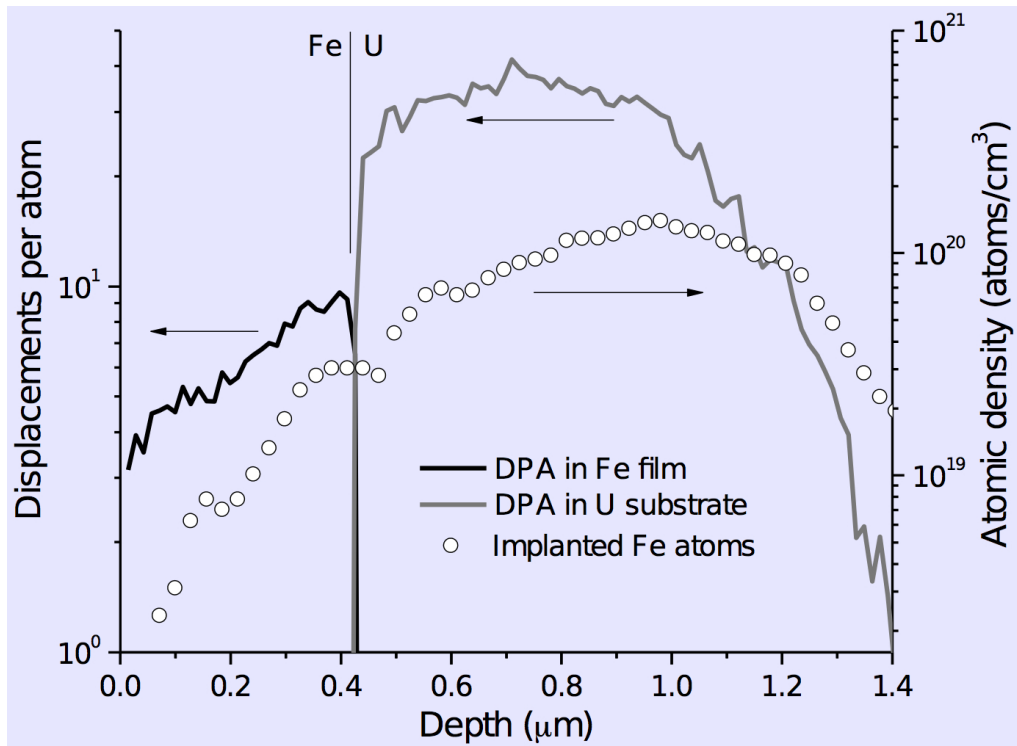
Figure 5.14: Experimental condition – 3.5 MeV Fe distribution.

5.5.1 Rutherford backscattering spectra of thin-film couples with radiation effect

Fig. 5.15 is a typical random spectra of the thin-film diffusion couples. The black is the virgin spectra, which is as-deposited. The green is the control specimen which was only annealed at the irradiation temperature. The red is the spectra with irradiation at elevated temperature. The individual contribution of the Fe (56), Cr (52) and Ni (59) will not be separable due to close atomic masses.

For instance, the front of the virgin spectra at channel number 400 is contributed by alloy thin-film, consist of Fe, Cr and Ni signals. As for uranium substrate, the yield front is shifted to lower channel number due the energy loss of the incoming He ions. Without the presence of the thin-film, the pure uranium yield front should appear close the channel number 500. Consequently, any yield front larger than channel number 400 indicates the uranium diffuses toward the surface. According to Fig. 5.15, enhanced uranium diffusion was observed for each irradiated specimens (red line). However, in both b-2 and c-2, significant fraction of uranium diffused to the surface at 550°C lead to sharp peak at channel number 500. In that case, no diffusion kinetics were extracted for U/(Fe+Cr) and U/(Fe+Cr+Ni) couples at the temperature.
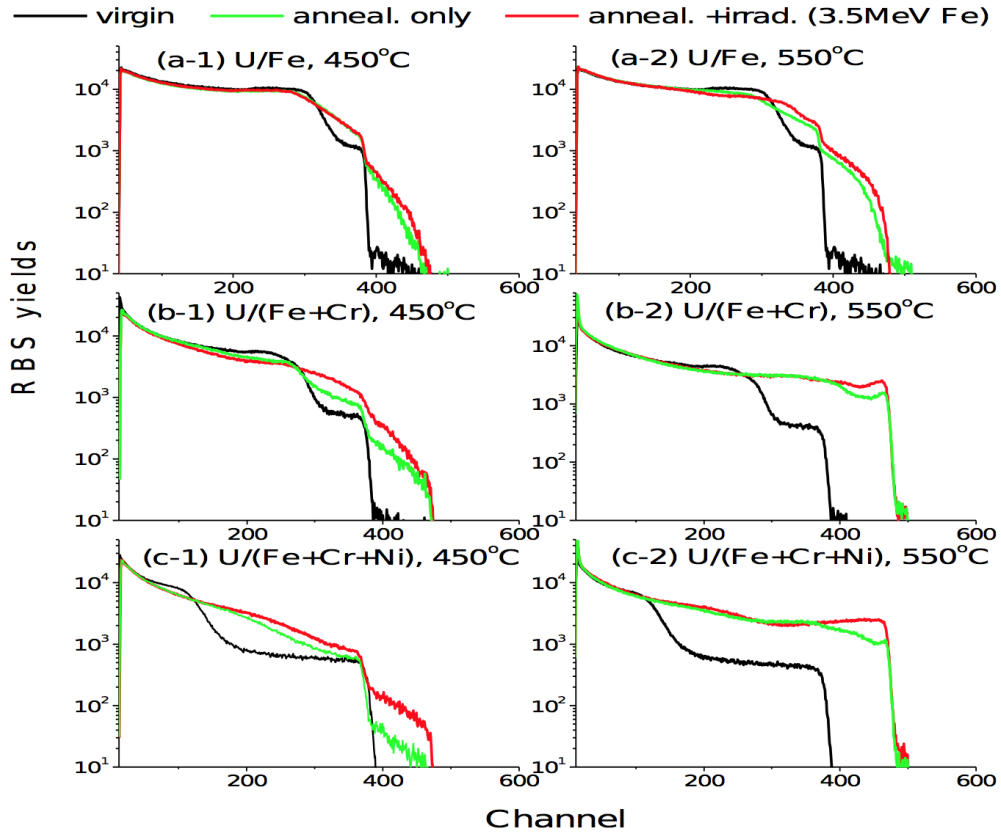
Figure 5.15: RBS spectra of U/Fe , U/(Fe+Cr), and U/(Fe+Cr+Ni)

SIMNRA code was employed to extract the diffusion profiles. 20 layers were generated to fit the RBS spectra, in which the deepest layer referred to uranium substrate. The fitting process started from the surface layer since uranium and alloy are well-separated. Then by changing the uranium concentration incrementally towards the deeper layer. Fig. 5.16 is the demonstration of the accuracy using SIMNRA code. The inset is the extracted uranium concentration upon 20 layers fitting. The red point indicates the 10% shift in the uranium concentration. Noticeable changes are marked as two arrows in the red fitting spectra which illustrates high sensitivity to the uranium concentration.
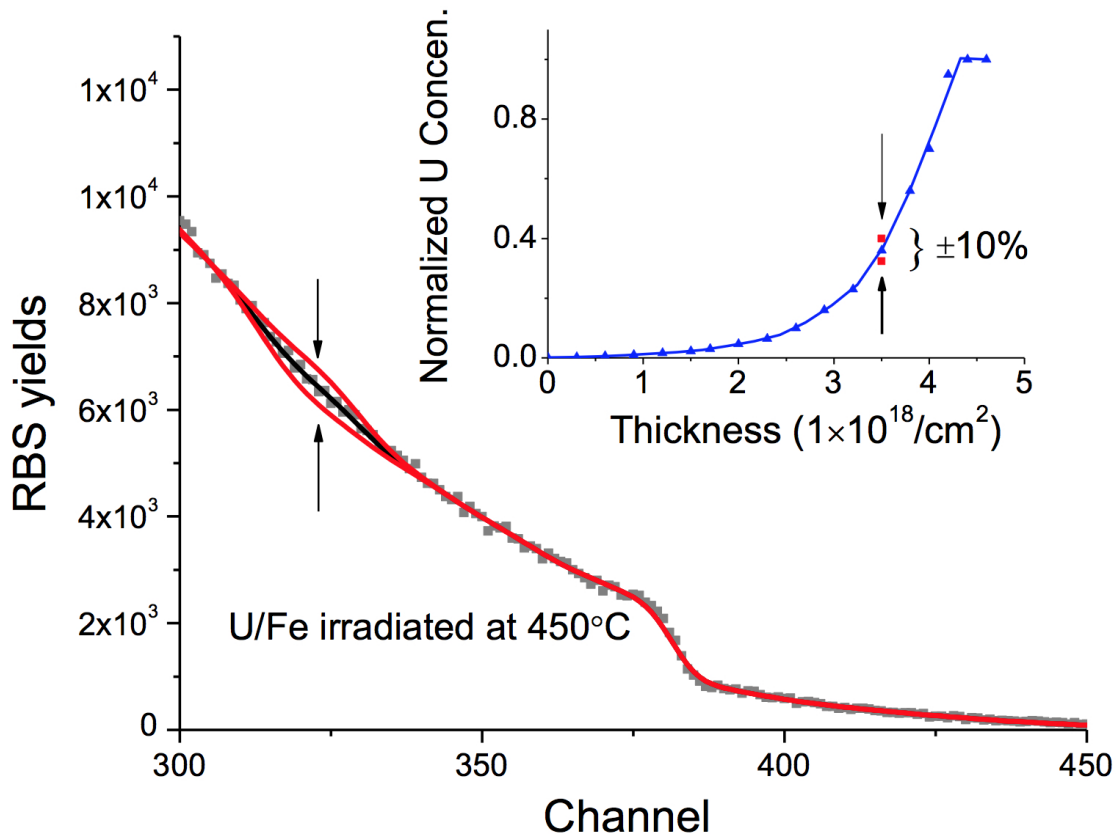
Figure 5.16: Sensitivity testing for the RBS spectra fitting in SIMNRA

5.5.2 RBS spectra and SIMNRA fitting analysis of U/Fe couples

Fig. 5.17 shows RBS spectra from the U/Fe thin-film diffusion couples. Experimental spectra were plotted as gray squares and overlap with SIMNRA fitting in black solid lines. The virgin U/Fe spectrum was taken and fitted, along with spectra from control and irradiated specimens at 450°C and 550°C, respectively. With the SIMNRA fitting, corresponding U/Fe concentration can be extracted. Fig. 5.18 shows the extracted composition profiles from exterior surface toward the uranium substrate. Uranium concentration is plotted in log scale to compare between control and irradiated specimen at 450°C. Small but noticeable enhancement can be

observed. The smooth concentration gradient between uranium and iron suggests no intermetallics formation.

The interdiffusion became greater at 550°C with wider concentration gradient of uranium and iron. The radiation enhanced diffusion is stronger from the uranium profile plotted in log scale. More importantly, the irradiation induced intermetallic phase formation is observed. The composition profile of the irradiated U/Fe started to form a transition regime with step-like distribution, whereas the control specimen shows smooth concentration gradient. The possible intermetallic formed at the arrow is likely to be U_6Fe phase.
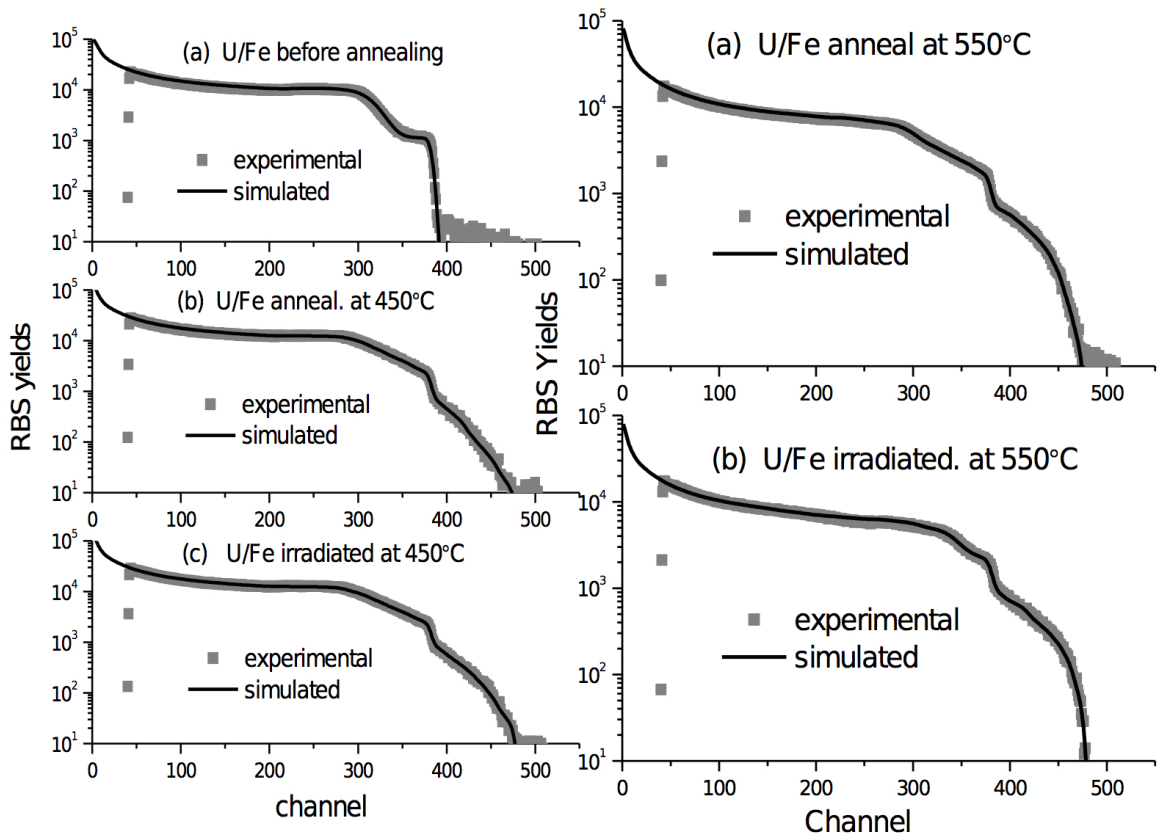
Figure 5.17: Simulated spectra for U/Fe couple
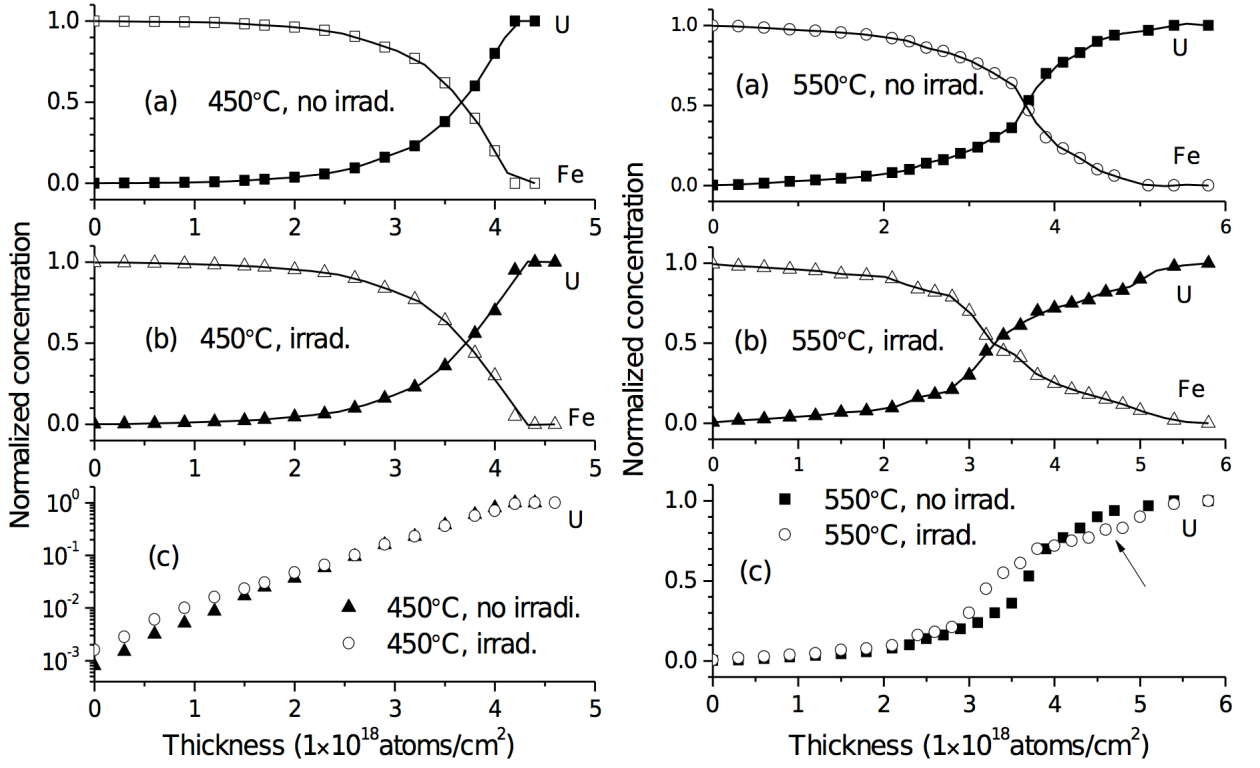
Figure 5.18: Extracted concentration from simulated spectra – U/Fe couple

5.5.3 Extracted interdiffusion coefficient from RBS spectra – U/Fe couple

In order to calculate the interdiffusion coefficient of the U/Fe couple, modified steps from the Equation 2.5 and 2.6 are listed as follows. First , Motano plane is determined using the Equation. 5.1,

$$\int_{C_U^{-\infty}}^{C_U^{+\infty}} (x - x_0) dC_U = 0 \tag{5.1}$$

where C_U is referred to uranium concentration at position x. The uranium concentration is 0 at the film surface and 1 at the uranium substrate. Second, the interdiffusion coefficient based on uranium concentration is calculated using Equation. 5.2.

$$\tilde{D}(C_U^*) = -\frac{1}{2t}\frac{\int_{C_U^{-\infty}}^{C_U^{+\infty}}(x-x_0)dC_U}{(dC_U/dx)_{C_U^*}} \tag{5.2}$$

The C_U^* is the corresponding uranium concentration where the interdiffusion coefficient is obtained. The fluctuation of dC_U / dx is minimized by using build-in Spline method of commercial software.

Fig. 5.19 shows the extracted uranium interdiffusion coefficient from U/Fe control specimens and irradiated specimens. It has been shown that the diffusivities decrease when uranium concentration increase. With the irradiation, the diffusivity shows approximately 25% increase at 450°C and 40% at 550°C compared to the diffusivities of control specimens. The activation energy can be calculated by using Equation. 2.7 and $\sim$ 0.2eV is obtained for 450°C regime. Above 0.4 uranium concentration at 550°C, the interdiffusion coefficient deviated from the straight line trend and lead to higher diffusivity. And yet, possible phase formation at that region and Equation. 5.2 became invalid due to the flux is no longer proportional to the concentration gradient.
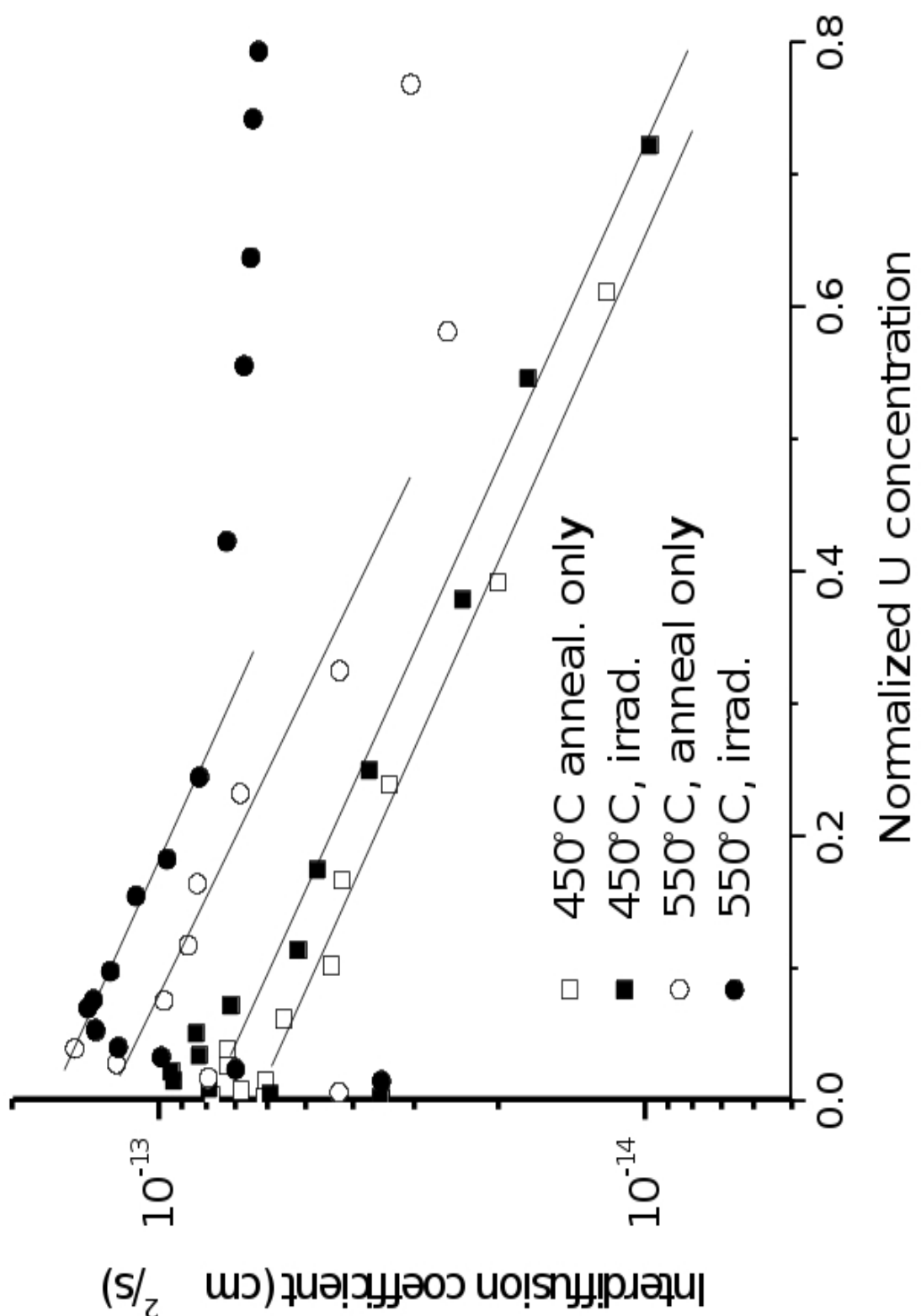
Figure 5.19: The interdiffusion coefficient from U/Fe couple at 450°C and 550°C, extracted from RBS fitting

5.5.4   RBS spectra and SIMNRA fitting analysis of U/(Fe+Cr+Ni) couples

All the experimental spectra and SIMNRA fitting spectra only include 450°C data due to excessive uranium diffused toward surface at 550°C. For the U/(Fe+Cr) diffusion couples, longer diffusion tail were observed after irradiation. In addition, both control and irradiated specimens showed step-like profile, which indicates possible phase formation. Due to close atomic masses between iron and chromium, it is difficult to identify which phase formed. Uranium and chromium does not form binary compound while two equilibrium U/Fe phases exist in the phase diagram. With the Cr addition, it promotes the U/Fe phase formation without irradiation. No diffusivities analysis since the Equation. 5.2 is not valid. In contrast to the U/(Fe+Cr) diffusion couples, no step-like profiles were observed in the U/(Fe+Cr+Ni) diffusion couples. However, the radiation enhanced diffusion still present upon the uranium profiles in log scale.

The diffusivity is strongly dependent to two factors, one is diffusion length and the other is diffusion frequency. The diffusion length is unlikely to be changed since it is related to the vacancy binding energy. On the other hand, the diffusion frequency is determined with either the probability of finding a nearby vacancy or the energy barrier needed to take a vacancy site. The damage cascades created by ion irradiation will induce supersaturated point defects. The net vacancies increased and the system is far from equilibrium which can overcome the energy barrier easily. Also, the defect recombination promotes atomic movement, including the phase formation.
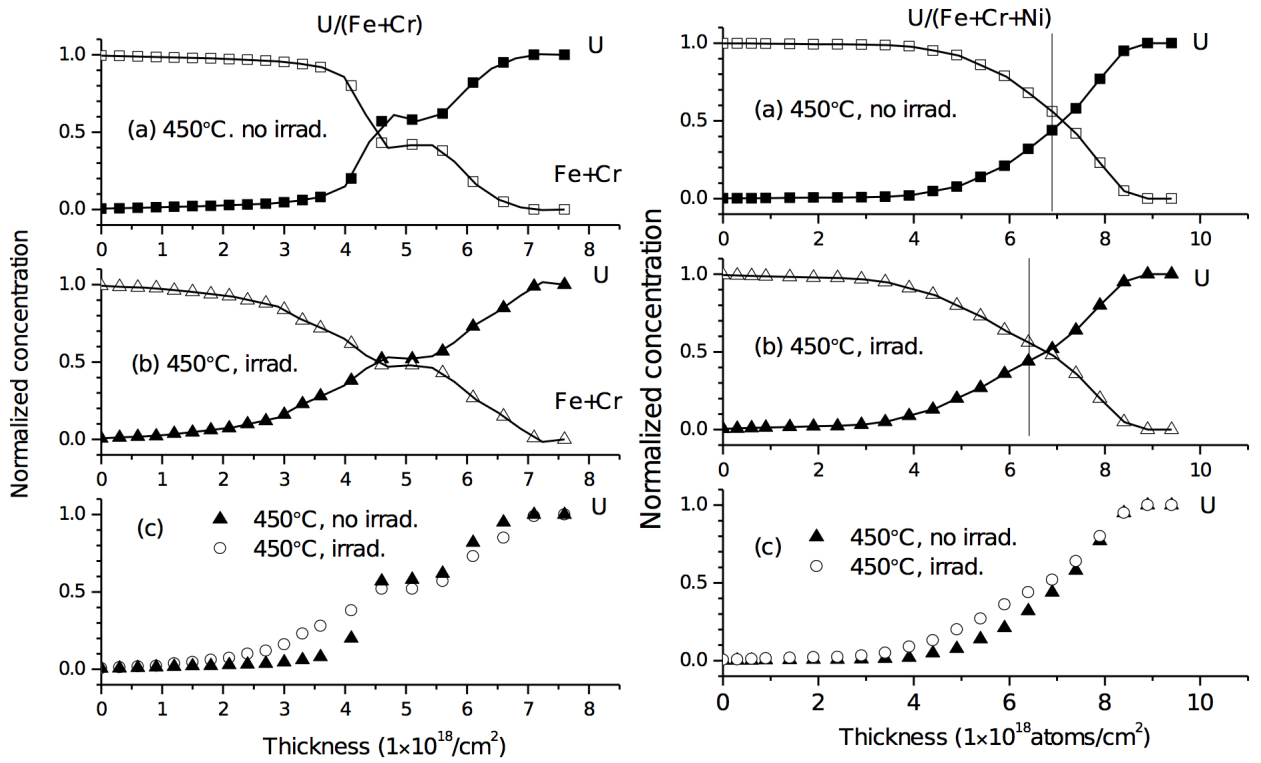
Figure 5.20: Extracted concentration from simulated spectra – U/(Fe+Cr) and U/(Fe+Cr+Ni) couple

6. SUMMARY

The purpose of the current section is to highlight the major findings of this dissertation. Through the diffusion couple technique, a wide range of intermetallics can be investigated for fundamental studies. Coupling with ion irradiation, radiation effect can be discussed on each phase, which provides useful information on developing new materials or solving the existing issues. The complexity of the advanced alloys can be simplified into binary system, not limited to microsctructural characterizations but mechanical properties measurement can be applied as well when needed.

In addition, fuel cladding chemical interaction is essential to simulate the fuel performance. Microstructure evolution under irradiation provides detailed insight to study the atomic potential far from the equilibrium. Understanding the interdiffusion between fuel constituent and cladding component will help predict the reactor lifetime. Furthermore, radiation effect has strong impacts to retard the diffusion process compared to steady-state FCCI and promote undesired phase formation which can cause poor mechanical properties. Also, diffusion coefficient, activation energy and crystal structures are required to support fuel element redistribution modeling.

Throughout this dissertation, we have demonstrated a novel methodology to study fundamentals of phase formation and diffusion kinetics. More importantly, radiation effects of FCCI is also studied. The summary is broken into two portions. The first is related to uranium-free diffusion systems, and the second is related to uranium-bearing systems.

6.1 Uranium-free diffusion systems

Zirconium and molybdenum, major components in the metallic fuel fabrication, have been studied using diffusion couple technique. Binary systems were assembled

with iron, a surrogate to the cladding materials. Both Fe/Zr and Fe/Mo systems were annealed at 850°C for 15 days to study thermally-activated diffusion. Four equilibrium phases were identified as $FeZr_3$, $FeZr_2$, Fe_2Zr and $Fe_{23}Zr_6$ in Fe/Zr diffusion couple. Surprisingly, with the presence of oxygen in the mixture of Fe_2Zr and $Fe_{23}Zr_6$ phases, we were able to clarify the formation mechanism of $Fe_{23}Zr_6$. Our findings indicated that the $Fe_{23}Zr_6$ phase first form at the interface of iron matrix and the Fe_2Zr phase. Then, iron depleted from Fe_2Zr phase towards the $Fe_{23}Zr_6$ phase and formed Zr-rich core. The oxygen was likely to take the empty iron lattice site based on the EDS profile. On the other hand, two phases formed in the Fe/Mo diffusion couple. These two intermetallics are stoichiometrically the same to the equilibrium phase reported in the phase diagram, but take different crystal structures. The Fe_7Mo_6 and Fe_2Mo phases were both identified as Face-centered Cubic (FCC) in this study, instead of hexagonal structures. Based on the findings via the diffusion couples technique, it can be argued that traditional alloying method may introduce impurities and stabilize the crystal structures.

Considering radiation effect, both Fe/Zr and Fe/Mo diffusion couples were irradiated with 3.5 MeV Fe ion. As a result, the Fe/Zr systems show significant radiation enhanced diffusion. It is also observed that new nano-meter size grains formed after irradiation in the Fe matrix, which may be Fe-Zr intermetallics due to additional Zr presence. There are no signs of phase transformation of all equilibrium Fe/Zr compounds. Similarly, radiation enhanced diffusion and radiation induced phase formation are observed in the Fe/Mo diffusion couple. The Fe_2Mo phase transformed to icosahedral quasicrystal which is the first time reported in the bulk materials. It turned out the FCC crystal structure is the approximant of the iQC. This discovery has huge impact to the fundamental transformation of iQC. With the simple binary system, iron and molybdenum can be modeled using known atomic potential.

6.2 Uranium-bearing diffusion systems

The depleted uranium has been tested to form multi-component solid-solid diffusion couples. Iron was then selected and formed diffusion couple to study fuel cladding chemical interaction. First, poly-crystalline iron were assembled with DU and annealed at 700°C for 4 days. Two equilibrium phases were identified as UFe_2 and U_6Fe and interdiffusion coefficient were calculated for each phase. The U/Fe diffusion couple were then irradiated with 2 MeV helium at 450°C. Transmission electron microscope was carried out to study the helium accumulation of the U/Fe intermetallics. The UFe_2 shows 3.9% swelling, three times higher than in U_6Fe phase. Second, depleted uranium was bonded against single-crystalline iron to study diffusion kinetics. Specimens were annealed at three elevated temperatures. The interdiffusion coefficients were extracted for each phase and furthermore activation energies were obtained. We also compared the diffusion kinetics of the single-crystalline iron with poly-crystalline iron, which diffused an order of magnitude faster due to the grain boundaries. The interdiffuson between uranium and nickel is also studied. The U/Ni diffusion couples were annealed at three elevated temperatures. Seven equilibrium phases, UNi_5, $U_{0.22}Ni_{0.78}$, $U_{0.23}Ni_{0.77}$, UNi_2, $U_{11}Ni_{16}$, U_7Ni_9 and U_6Ni, were observed consistently in all temperatures for the first time. Systematic diffusion kinetics were studied and activation energies of each phase were obtained.

Thin-film deposition was also employed to study diffusion kinetics.Several advantages list as follows, 1) the deposition is independent to the substrate roughness. 2) no cavities due to the homogeneous growth, atom by atom. 3) the ion etching prior to the deposition can significantly reduce oxidation. Radiation enhanced diffusion is observed using Rutherford backscattering spectrometry (RBS), which is a fast and non-destructible technique. RBS spectra were then fitted to the SIMNRA code and

chemical composition upon diffusion was extracted. Diffusion kinetics and activation energies were calculated using normalized uranium concentration.

To sum up, the thermally-activated diffusion couples can be utilized for different research purposes. Here we have shown a series of multi-component systems to study FCCI. As a result, diffusion coefficients, activation energies, and crystal structures can be a huge assets to the computational modeling. With on single diffusion couple, phase diagrams can be verified along with the radiation effect of each phase. In addition, simple binary diffusion systems are the fundamentals to the complex system, such as metallic fuel alloys against advanced steels.

REFERENCES

[1] AAS, S., AND STEINEGGER, A. Interdiffusion of uranium and nickel. *Amer. Soc. Metals 61* (Jan 1957), 703.

[2] ALDERMAN, C., AND PITNER, A. Transient testing of long-lifetime mixed-oxide liquid-metal reactor fuel. *Transactions of the American Nuclear Society 56* (1988), 382–383. cited By (since 1996)4.

[3] BAKER, H. Alloy phase diagrams. *ASM Handbook* (1992). cited By (since 1996)878.

[4] BAKER, R., BARD, F., AND ETHRIDGE, J. *Proceedings of LMR: A Decade of LMR Progress and Promise* (1990), 185. cited By (since 1996)1.

[5] BAKER, R., BARD, F., LEGGETT, R., AND PITNER, A. Status of fuel, blanket, and absorber testing in the fast flux test facility. *Journal of Nuclear Materials 204*, C (1993), 109–118. cited By (since 1996)12.

[6] BARNES, R. Swelling and inert gas diffusion in irradiated uranium. *Proceedings of the 2nd United Nations International Conference on Peaceful Uses of Atomic Energy, Communique 5, No. 500* (1958). cited By (since 1996)1.

[7] BARNES, R. A theory of swelling and gas release for reactor materials. *Journal of Nuclear Materials 11*, 2 (1964), 135–148. cited By (since 1996)19.

[8] BATTÉ, G., AND HOFMAN, G. Run-beyond-cladding breach (rbcb) test results for the integral fast reactor (ifr) metallic fuels program. *International Fast Reactor Safety Meeting IV* (1990), 207. cited By (since 1996)1.

[9] BAUER, T., AND HOLLAND, J. Integral fast reactor metallic fuel program in pile measurement of the thermal conductivity of irradiated metallic fuel.

Transactions of the American Nuclear Society 65 (1992), 278. cited By (since 1996)1.

[10] BAUER, T. H., AND HOLLAND, J. W. In-pile measurement of the thermal conductivity of irradiated metallic fuel. *Nuclear Technology 110*, 3 (1995), 407–421. cited By (since 1996)9.

[11] BAUER, T. H., WRIGHT, A. E., ROBINSON, W. R., HOLLAND, J. W., AND RHODES, E. A. Behavior of modern metallic fuel in treat transient overpower tests. *Nuclear Technology 92*, 3 (1990), 325–352. cited By (since 1996)13.

[12] BECK, W., AND FOUSEK, R. Fission gas release and thermal conductivity measurements on u-5 wt fs irradiated in cp-5. *Trans. Am. Nucl. Soc. 12* (1969). cited By (since 1996)2.

[13] BECK, W., FOUSEK, R., AND KITTEL, J. The irradiation behavior of high-burnup uranium-plutonium alloy prototype fuel elements. *Argonne National Lab. III* (1968). cited By (since 1996)2.

[14] BELLAMY, R. The swelling of alpha-uranium under neutron irradiation with 0.7burn-up. *Institute of Metallurgy Symposium on Uranium and Graphite* (1962). cited By (since 1996)1.

[15] BETTEN, P. In-core measurements of uranium - 5 wt.conductivity. *Trans. Am. Nucl. Soc. 50* (1985), 239. cited By (since 1996)3.

[16] BILLONE, M., AND GRAYHACK, W. Fuel creep model for life-metal. *Argonne National Laboratory Memorandum* (1987). cited By (since 1996)1.

[17] BLAKE, L. Achieving high burn-up in fast reactors. *Journal of Nuclear Energy. Parts A/B. Reactor Science and Technology 14*, 1-4 (1961), 31–48. cited By (since 1996)3.

[18] BOZZOLO, G., HOFMAN, G., YACOUT, A., AND MOSCA, H. Lanthanides migration and immobilization in u-zr nuclear fuels. *J. Nucl. Matls. 425* (2011), 188–192. cited By (since 1996)1.

[19] BOZZOLO, G., YACOUT, A., HOFMAN, G., MOSCA, H., AND WRIGHT, A. Investigation of the effects of alloying additions to u-zr fuel via atomistic simulation. *Transactions of the American Nuclear Society 106* (2012), 1378–1380. cited By (since 1996)1.

[20] BRIGGS, B., AND FRISKE, W. Development of niobium diffusion barriers for aluminum-clad uranium alloy fuel elements. *Atomics International 50* (1963). cited By (since 1996)1.

[21] CAMPBELL, D., AND HUNTINGTON, H. Thermomigration and electromigration in zirconium. *Physical Review 179*, 3 (1969), 601–611. cited By (since 1996)14.

[22] CARMACK, W., PORTER, D., CHANG, Y., HAYES, S., MEYER, M., BURKES, D., LEE, C., MIZUNO, T., DELAGE, F., AND SOMERS, J. Metallic fuels for advanced reactors. *Journal of Nuclear Materials 392*, 2 (2009), 139–150. cited By (since 1996)29.

[23] CHANG, Y. Technical rationale for metal fuel in fast reactors. *Nucl. Eng. Technol. 39*, 3 (2007). cited By (since 1996)21.

[24] CHANG, Y. I. Integral fast reactor. *Nuclear Technology 88*, 2 (1989), 129–138. cited By (since 1996)147.

[25] CHICHESTER, H., MARIANI, R., HAYES, S., KENNEDY, J., WRIGHT, A., KIM, Y., YACOUT, A., AND HOFMAN, G. Advanced metallic fuel for ultra-

high burnup: Irradiation tests in atr. vol. 106, pp. 1349–1351. cited By (since 1996)0.

[26] Cohen, A., Tsai, H., and Neimark, L. Fuel/cladding compatibility in u-19pu-10zr/ht9-clad fuel at elevated temperatures. *Journal of Nuclear Materials 204*, C (1993), 244–251. cited By (since 1996)33.

[27] Cole, J., Keiser Jr., D., and Kennedy, J. *Proceedings of Global2007* (2007), 1375. cited By (since 1996)1.

[28] Crawford, D., Porter, D., and Hayes, S. Fuels for sodium-cooled fast reactors: Us perspective. *Journal of Nuclear Materials 371*, 1-3 (2007), 202–231. cited By (since 1996)68.

[29] D'Amico, J., and Huntington, H. Electromigration and thermomigration in gamma irradiation. *Journal of Physics and Chemistry of Solids 30* (1969), 1607. cited By (since 1996)1.

[30] Davis, J. Asm handbook properties and selection: Nonferrous alloys and special-purpose materials. *ASM International* (1992). cited By (since 1996)1.

[31] De Volpi, A., Fink, C., Marsh, G., Rhodes, E., and Stanford, G. Fast-neutron hodoscope at treat: Methods for quantitative determination of fuel dispersal. *Nuclear Technology 56*, 1 (1982), 141–188. cited By (since 1996)3.

[32] DiNovi, R. Effect of burnup, swelling and irradiation temperature on thermal diffusivity and conductivity of uranium-fissium alloy. *Argonne National Lab. III* (1972). cited By (since 1996)1.

[33] Enderby, J. Plastic flow and swelling of gas bubbles in uranium. *Dept. of Atomic Energy. Industrial Group HQ, Risley, Lancs, England* (1956). cited By

(since 1996)1.

[34] Fedorov, G., Smirnov, E., Zhomov, F., Gusev, V., and Paraev, S. Diffusion of uranium in refractory bcc metals. *Soviet Atomic Energy 31*, 5 (1972), 1280–1282. cited By (since 1996)5.

[35] Fistedis, S. The experimental breeder reactor-ii inherent safety demonstration. cited By (since 1996)5.

[36] Frost, B., Mardon, P., and Russell, L. Research on the fabrication, properties, and irradiation behavior of plutonium fuels for the u.k. reactor programme. *Proceedings of the American Nuclear Society Meeting on Plutonium As a Power Reactor Fuel* (1962), 41. cited By (since 1996)1.

[37] Golden, G., Planchon, H., Sackett, J., and Singer, R. Evolution of thermal-hydraulics testing in ebr-ii. *Nuclear Engineering and Design 101*, 1 (1987), 3–12. cited By (since 1996)10.

[38] Greenwood, G. The effects of neutron irradiation on -uranium and some fissile alloys of cubic crystal structure. *Journal of Nuclear Materials 6*, 1 (1962), 26–34. cited By (since 1996)3.

[39] Haas, M., Cerchione, J., Dunworth, R., Fryer, R., Wilkes, C., and Derbidge, M. Fabrication of driver-fuel elements for ebr-ii. *ANL 79-38*, 1979. cited By (since 1996)1.

[40] Hayes, S. U.s. test plans for actinide transmutation fuel development. *American Nuclear Society Winter Meeting* (2002). cited By (since 1996)1.

[41] Hehenkamp, T. Electro-and thermotransport in metals and alloys. *AIME Symposium* (1977), 68. cited By (since 1996)1.

[42] HILTON, B. The afc-1æ and afc-1f irradiation tests of metallic and nitride fuels for actinide transmutation. *American Nuclear Society meeting on Advanced Nuclear Energy Systems* (2003). cited By (since 1996)1.

[43] HILTON, B., PORTER, D., STEVEN, L., AND HAYES. Postirradiation examination of afci metallic transmutation fuels at 8 at. *Presented at the Summer 2006 American Nuclear Conference* (2006). cited By (since 1996)1.

[44] HOFMAN, G. Irradiation behavior of experimental mark-ii experimental breeder reactor ii driver fuel. *Nuclear Technology 47*, 1 (1980), 7–22. cited By (since 1996)12.

[45] HOFMAN, G., HINS, A., PORTER, D., LEIBOWITZ, L., AND WOOD, E. Chemical interaction of metallic fuel with austenitic and ferritic stainless steel cladding. *Proceedings of the International Conference on Reliable Fuels for Liquid Metal Reactors* (1986), 12. cited By (since 1996)1.

[46] HOFMAN, G. L., PAHL, R., LAHM, C., AND PORTER, D. Swelling behavior of u-pu-zr fuel. *Metallurgical transactions. A, Physical metallurgy and materials science 21 A*, 3 (1990), 517–528. cited By (since 1996)29.

[47] HORAK, J., KITTEL, J., AND DUNWORTH, R. The effects of irradiation on uranium-plutonium-fissium fuel alloys. *Argonne National Laboratory 6429* (1962). cited By (since 1996)1.

[48] HUANG, K., HEINRICH, H., KEISER JR., D., AND SOHN, Y. Fuel-matrix chemical interaction between u-7wt. *Defect and Diffusion Forum 333* (2013), 199–206. cited By (since 1996)1.

[49] HUANG, K., KAMMERER, C., KEISER, D., AND SOHN, Y. Diffusion barrier selection from refractory metals (zr, mo and nb) via interdiffusion investigation

for u-mo rertr fuel alloy. *Journal of Phase Equilibria and Diffusion 35*, 2 (2014), 146–156. cited By (since 1996)0.

[50] HUANG, K., KEISER JR., D., AND SOHN, Y. Interdiffusion, intrinsic diffusion, atomic mobility, and vacancy wind effect in (bcc) uranium-molybdenum alloy. *Metallurgical and Materials Transactions A: Physical Metallurgy and Materials Science 44*, 2 (2013), 738–746. cited By (since 1996)3.

[51] HUANG, K., PARK, Y., EWH, A., SENCER, B., KENNEDY, J., COFFEY, K., AND SOHN, Y. Interdiffusion and reaction between uranium and iron. *Journal of Nuclear Materials 424*, 1-3 (2012), 82–88. cited By (since 1996)4.

[52] HUANG, K., PARK, Y., KEISER, D., AND SOHN, Y. Interdiffusion between zr diffusion barrier and u-mo alloy. *Journal of Phase Equilibria and Diffusion 33*, 6 (2012), 443–449. cited By (since 1996)6.

[53] HUANG, K., PARK, Y., KEISER JR., D., AND SOHN, Y. Interdiffusion between potential diffusion barrier mo and u-mo metallic fuel alloy for rertr applications. *Journal of Phase Equilibria and Diffusion 34*, 4 (2013), 307–312. cited By (since 1996)1.

[54] IVANOV, O., AND BAGROV, G. Isothermal cross sections at 600, 575, and 500-c, ploythermal sections, and the phase diagram of the triple system uranium-molybdenum-zirconium. *Struct. Alloys Certain Syst. Cont. Uranium Thorium* (1963), 154. cited By (since 1996)2.

[55] IVANOV, O., AND BAGROV, G. Isothermal cross sections of the triple system uranium-molybdenum- zirconium at 1000 °c-625 °c. *Struct. Alloys Certain Syst. Cont. Uranium Thorium* (1963), 131–153. cited By (since 1996)3.

[56] Jelinek, H., Carson, N., and Shuck, A. Manufacture of ebr-ii core i. *Fuel ANL-6274* (1961). cited By (since 1996)1.

[57] Keiser, D. The development of fuel cladding interaction zones in irradiated u-zr and u-pu-zr fuel elements with stainless steel cladding. *Nuclear Reactors, Nuclear Fusion and Fusion Engineering, Nova Science Publishers* (2009), 163–194. cited By (since 1996)4.

[58] Keiser, D., and Dayananda, M. Interdiffusion between u-zr fuel vs selected cladding steels. *Metallurgical and Materials Transactions A 25*, 8 (1994), 1649–1653. cited By (since 1996)16.

[59] Keiser D.D., J., and Petri, M. *Proc. 15th Ann. Conf. of the Can. Nucl. Soc.* (1994), 5C. cited By (since 1996)2.

[60] Keiser Jr., D., and Cole, J. Fuel-cladding compatibility in metallic nuclear fuels. *TMS Letters 2*, 3 (2005), 79–80. cited By (since 1996)10.

[61] Keiser Jr., D., and Dayananda, M. Interdiffusion between u-zr fuel and selected fe-ni-cr alloys. *Journal of Nuclear Materials 200*, 2 (1993), 229–243. cited By (since 1996)20.

[62] Keiser Jr., D., Hayes, S., Meyer, M., and Clark, C. High-density, low-enriched uranium fuel for nuclear research reactors. *JOM 55*, 9 (2003), 55–58. cited By (since 1996)13.

[63] Keiser Jr., D., Jue, J.-F., Yao, B., Perez, E., Sohn, Y., and Clark, C. Microstructural characterization of u-7mo/al-si alloy matrix dispersion fuel plates fabricated at 500 °c. *Journal of Nuclear Materials 412*, 1 (2011), 90–99. cited By (since 1996)14.

[64] KEISER JR., D., KENNEDY, J., HILTON, B., AND HAYES, S. The development of metallic nuclear fuels for transmutation applications: Materials challenges. *JOM 60*, 1 (2008), 29–32. cited By (since 1996)12.

[65] KEISER JR., D., AND PETRI, M. Interdiffusion behavior in u-pu-zr fuel versus stainless steel couples. *Journal of Nuclear Materials 240*, 1 (1996), 51–61. cited By (since 1996)33.

[66] KIM, T., AND WRIGHT, A. Development of advanced ultra-high burnup sfr metallic fuel concept - impacts on core characteristics and fuel cycle performance. *Transactions of the American Nuclear Society 106* (2012), 1362–1363. cited By (since 1996)1.

[67] KIM, Y., CHOO, Y., RYU, H., YACOUT, A., AND HOFMAN, G. Fcmi and cladding creep modeling for ultra high burnup metallic fuel designs. vol. 103, pp. 289–290. cited By (since 1996)3.

[68] KIM, Y., HAYES, S., HOFMAN, G., AND YACOUT, A. Modeling of constituent redistribution in u-pu-zr metallic fuel. *Journal of Nuclear Materials 359*, 1-2 (2006), 17–28. cited By (since 1996)21.

[69] KIM, Y., HOFMAN, G., HAYES, S., AND SOHN, Y. Constituent redistribution in u-pu-zr fuel during irradiation. *Journal of Nuclear Materials 327*, 1 (2004), 27–36. cited By (since 1996)23.

[70] KIM, Y., HOFMAN, G., RYU, H., AND HAYES, S. Irradiation-enhanced interdiffusion in the diffusion zone of u-mo dispersion fuel in al. *Journal of Phase Equilibria and Diffusion 27*, 6 (2006), 614–621. cited By (since 1996)9.

[71] KIM, Y., HOFMAN, G., AND YACOUT, A. Migration of minor actinides and lanthanides in fast reactor metallic fuel. *Journal of Nuclear Materials 392*, 2

(2009), 164–170. cited By (since 1996)24.

[72] Kim, Y., Wiencek, T., O'Hare, E., Hofman, G., and Fortner, J. Immobilization of fission product lanthanides in metallic fast reactor fuel. vol. 105, pp. 391–392. cited By (since 1996)1.

[73] Kimmel, G., Bar-Or, A., and Rosen, A. Interdiffusion between nickel and uranium. *Tidsskr. Kjemi Bergvesen Met 10* (Jan 1968).

[74] Kittel, J. Layer formation by interdiffusion between some reactor construction metals. *Report No. ANL-4937* (1949). cited By (since 1996)2.

[75] Kittel, J., Frost, B., Mustelier, J., Bagley, K., Crittenden, G., and Van Dievoet, J. History of fast reactor fuel development. *Journal of Nuclear Materials 204*, C (1993), 1–13. cited By (since 1996)40.

[76] Kobayashi, T., Kinoshita, M., Hattori, S., Ogawa, T., Tsuboi, Y., Ishida, M., Ogawa, S., and Saito, H. Development of the sesame metallic fuel performance code. *Nuclear Technology 89*, 2 (1990), 183–193. cited By (since 1996)10.

[77] Komar Varela, C., Mirandou, M., Aricó, S., Balart, S., and Gribaudo, L. Interdiffusion between u(mo,pt) or u(mo,zr) and al or al a356 alloy. *Journal of Nuclear Materials 395*, 1-3 (2009), 162–168. cited By (since 1996)12.

[78] Kramer, J., Liu, Y., Billone, M., and Tsai, H. Modeling the behavior of metallic fast reactor fuels during extended transients. *Journal of Nuclear Materials 204*, C (1993), 203–211. cited By (since 1996)12.

[79] Kulcinski, G., Leggett, R., Hann, C., and Mastel, B. Fission gas induced swelling in uranium at high temperatures and pressures. *Journal of Nuclear Materials 30*, 3 (1969), 303–313. cited By (since 1996)2.

[80] Lahm, C., Koenig, J., Pahl, R., Porter, D., and Crawford, D. Experience with advanced driver fuels in ebr-ii. *Journal of Nuclear Materials 204*, C (1993), 119–123. cited By (since 1996)14.

[81] Lambert, J., Lehto, W., Sackett, J., Hill, D., Planchon, H., and Lindsay, R. Ebr-ii test programs. *International Fast Reactor Safety Meeting III* (1990), 181. cited By (since 1996)3.

[82] Leenaers, A., Van Den Berghe, S., Koonen, E., Jarousse, C., Huet, F., Trotabas, M., Boyard, M., Guillot, S., Sannen, L., and Verwerft, M. Post-irradiation examination of uranium-7 wtdispersion fuel. *Journal of Nuclear Materials 335*, 1 (2004), 39–47. cited By (since 1996)82.

[83] Leenaers, A., Van Den Berghe, S., Van Renterghem, W., Charollais, F., Lemoine, P., Jarousse, C., Röhrmoser, A., and Petry, W. Irradiation behavior of ground u(mo) fuel with and without si added to the matrix. *Journal of Nuclear Materials 412*, 1 (2011), 41–52. cited By (since 1996)22.

[84] Leggett, R., Bierlein, T., and Mastel, B. Basic swelling studies, radiation effects. *American Institute of Metallurgical Engineering Symposium* (1967), 303. cited By (since 1996)1.

[85] Leggett, R., Hann, C., Mastel, B., and Mereka, K. Swelling of irradiated fissionable materials. cited By (since 1996)1.

[86] Leggett, R., and Walters, L. Status of lmr fuel development in the united states of america. *Journal of Nuclear Materials 204*, C (1993), 23–32. cited By (since 1996)35.

[87] Lehmann, J., Paoli, P., and Azam, N. Etude du gonflement d'alliages d'uranium sous irradiation. *Journal of Nuclear Materials 27*, 3 (1968), 285–309. cited By (since 1996)1.

[88] Lengauer, W. The temperature gradient diffusion couple technique: An application of solid-solid phase reactions for phase diagram imaging. *Journal of Solid State Chemistry 91*, 2 (1991), 279–285. cited By (since 1996)6.

[89] Liu, X., Lu, T., Xing, Z., and Qian, D. Effects of different irradiation conditions on swelling performance of u10mo-al dispersion fuel. *Xiyou Jinshu Cailiao Yu Gongcheng/Rare Metal Materials and Engineering 40*, 6 (2011), 1125–1128. cited By (since 1996)5.

[90] Liu, Y., Tsai, H., Billone, M., Holland, J., and Kramer, J. Behavior of ebr-ii mk-v-type fuel elements in simulated loss-of-flow tests. *Journal of Nuclear Materials 204*, C (1993), 194–202. cited By (since 1996)11.

[91] Makin, M., Chatwin, W., Evans, J., Hudson, B., and Hyam, E. The study of irradiation damage in uranium by electron microscopy. *Institute of Metallurgy Symposium on Uranium and Graphite* (1962). cited By (since 1996)1.

[92] Mariani, R., Chichester, H., Hayes, S., and Kennedy, J. Advanced metallic fuel for ultra-high burnup: Irradiation tests in atr. *Transactions of the American Nuclear Society 106* (2012), 1349–1351. cited By (since 1996)1.

[93] Mariani, R., Porter, D., Hayes, S., and Kennedy, J. Chemical stabilization of metallic nuclear fuels. *Transactions of the American Nuclear Society, Embedded Topical on Nuclear Fuel and Structural Materials* (2012), 1098–1101. cited By (since 1996)1.

[94] MARIANI, R., PORTER, D., O'HOLLERAN, T., HAYES, S., AND KENNEDY, J. Lanthanides in metallic nuclear fuels: Their behavior and methods for their control. *Journal of Nuclear Materials 419*, 1-3 (2011), 263–271. cited By (since 1996)8.

[95] MAZAUDIER, F., PROYE, C., AND HODAJ, F. Further insight into mechanisms of solid-state interactions in umo/al system. *Journal of Nuclear Materials 377*, 3 (2008), 476–485. cited By (since 1996)38.

[96] MEHRER, H. Diffusion in solids. cited By (since 1996)191.

[97] MERTEN, U., BOKROS, J., GUGGISBERG, D., AND HATCHER, A. Thermal migration of hydrogen in zirconium-uranium-hydrogen alloys. *Journal of Nuclear Materials 10*, 3 (1963), 201–208. cited By (since 1996)3.

[98] MEYER, M., HOFMAN, G., HAYES, S., CLARK, C., WIENCEK, T., SNELGROVE, J., STRAIN, R., AND KIM, K.-H. Low-temperature irradiation behavior of uranium-molybdenum alloy dispersion fuel. *Journal of Nuclear Materials 304*, 2-3 (2002), 221–236. cited By (since 1996)77.

[99] MILES, K. Metal fuel safety performance. *Proceedings of the International Topical Meeting in Safety of Next Generation Fast Reactors* (1988), 119–124. cited By (since 1996)3.

[100] MURPHY, W., BECK, W., BROWN, S., KOPOWSKI, B., AND NEIMARK, L. Post irradiation examination of u-pu-zr fuel elements irradiated in ebr-ii to 4.5 at *Argonne National Lab 7602* (1969). cited By (since 1996)1.

[101] MUSTELIER, J. Quelques resultes d'irradiation sur les combustibles evisages par rapsodie. *Symposium on the Effects of Irradiation on Solids and Materials for Reactors* (1962), 163. cited By (since 1996)3.

[102] NICOLET, M.-A. Diffusion barriers in thin films. *Thin Solid Films 52*, 3 (1978), 415–443. cited By (since 1996)247.

[103] O'BOYLE, D., AND DWIGHT, A. The uranium-plutonium-zirconium ternary alloy system. *Nucl. Mater. 17* (1970). cited By (since 1996)3.

[104] OGATA, T. Irradiation behavior and thermodynamic properties of metallic fuel. *J. Nucl. Sci. Technol., Suppl 3* (2003), 675–681.

[105] OGATA, T., KURATA, M., NAKAMURA, K., ITOH, A., AND AKABORI, M. Reactions between u-zr alloys and fe at 923 k. *Journal of Nuclear Materials 250*, 2-3 (1997), 171–175. cited By (since 1996)17.

[106] OHTA, H., OGATA, T., YOKOO, T., OUGIER, M., GLATZ, J.-P., FONTAINE, B., AND BRETON, L. Low-burnup irradiation behavior of fast reactor metal fuels containing minor actinides. *Nuclear Technology 165*, 1 (2009), 96–110. cited By (since 1996)10.

[107] PAHL, R. A proposed correlation for u-19pu-10zr/d9 fcci. *Argonne National Laboratory Memorandum* (19th March 1990). cited By (since 1996)1.

[108] PAHL, R., PORTER, D., CRAWFORD, D., AND WALTERS, L. Irradiation behavior of metallic fast reactor fuels. *Journal of Nuclear Materials 188*, C (1992), 3–9. cited By (since 1996)28.

[109] PAHL, R., PORTER, D., LAHM, C., AND HOFMAN, G. Experimental studies of u-pu-zr fast reactor fuel pins in ebr-ii. *Metallurgical Transactions A 21 A* (1990), 1863. cited By (since 1996)1.

[110] PAHL, R., WISNER, R., BILLONE, M., AND HOFMAN, G. Steady-state irradiation testing of u-pu-zr fuel¿18 *Proc. Int. Fast Reactor Safety Mtg. 4* (1990). cited By (since 1996)15.

[111] Pavlinov, L., Nakonechnikov, A., and Bykov, V. Diffusion of uranium in molybdenum. *Soviet Atomic Energy 19* (1965), 1495. cited By (since 1996)1.

[112] Perez, E., Keiser, D., Yao, B., and Sohn, Y. Interdiffusion in diffusion couples: U-mo v. al and al-si, rertr 2009. *31st International Meeting on Reduced Enrichment for Research and Test Reactors* (2009). cited By (since 1996)2.

[113] Perez, E., Keiser Jr., D., and Sohn, Y. Phase constituents and microstructure of interaction layer formed in u-mo alloys vs al diffusion couples annealed at 873 k (600 °c). *Metallurgical and Materials Transactions A: Physical Metallurgy and Materials Science 42*, 10 (2011), 3071–3083. cited By (since 1996)13.

[114] Perez, E., Yao, B., Keiser Jr., D., and Sohn, Y. Microstructural analysis of as-processed u-10 wt.plate in aa6061 matrix with zr diffusion barrier. *Journal of Nuclear Materials 402*, 1 (2010), 8–14. cited By (since 1996)16.

[115] Petri, M., Hins, A., Sanecki, J., and Dayananda, M. Uranium-plutonium interdiffusion at 750 °c. *Journal of Nuclear Materials 211*, 1 (1994), 1–10. cited By (since 1996)8.

[116] Pitner, A., and Baker, R. Metal fuel test program in the fftf. *Journal of Nuclear Materials 204*, C (1993), 124–130. cited By (since 1996)14.

[117] Porter, D. Fuel test plan. *Argonne National Laboratory, General Electric, and Westinghouse-Hanford Co* (1994). cited By (since 1996)1.

[118] Porter, D., Lahm, C., and Pahl, R. Fuel constituent redistribution during the early stages of u-pu-zr irradiation. *Metallurgical transactions. A, Physical metallurgy and materials science 21 A*, 7 (1990), 1871–1876. cited By (since 1996)19.

[119] PUGH, S. Swelling in alpha uranium due to irradiation. *The Metal Plutonium* (1961). cited By (since 1996)1.

[120] RHODES, E. A., BAUER, T. H., STANFORD, G. S., REGIS, J. P., AND DICKERMAN, C. E. Fuel motion in overpower tests of metallic integral fast reactor fuel. *Nuclear Technology 98*, 1 (1992), 91–99. cited By (since 1996)3.

[121] RYU, H., PARK, J., KIM, C., KIM, Y., AND HOFMAN, G. Diffusion reaction behaviors of u-mo/al dispersion fuel. *Journal of Phase Equilibria and Diffusion 27*, 6 (2006), 651–658. cited By (since 1996)17.

[122] SACKETT, J., LEHTO, W., AND SOLBRIG, C. The role of ebr-ii and treat in establishing liquid metal reactor safety. *Proceedings, LMR: A Decade of LMR Progress and Promise* (1990), 61. cited By (since 1996)2.

[123] SEIDEL, B., BARTÉ, G., LAHM, C., FRYER, R., KOENIG, J., AND HOFMAN, G. Off-normal performance of ebr-ii driver fuel. *Proceedings International Conf. Reliable Fuels for Liquid Metal Reactors* (1986), 6–48. cited By (since 1996)3.

[124] SEIDEL, B., AND EINZIGER, R. In-reactor cladding breach of ebr-ii driver fuel elements. *Argonne National Lab III* (1977). cited By (since 1996)3.

[125] SEIDEL, B., PORTER, D., WALTERS, L., AND HOFMAN, G. Experience with ebr-ii driver fuel. *Proceedings of the International Conference Reliable Fuels for Liquid Metal Reactors* (1986), 2–106. cited By (since 1996)3.

[126] SHEWMON, P. The redistribution of a second phase during annealing in a temperature gradient. *Trans. Met. Soc. AIME 212* (1958), 642. cited By (since 1996)1.

[127] SMITH, M., HILL, R., AND WILLIAMSON, M. Low conversion ratio fuel studies. *Argonne National Laboratory Report, ANL-AFCI-163* (2006). cited By (since 1996)1.

[128] SNELGROVE, J., HOFMAN, G., MEYER, M., TRYBUS, C., AND WIENCEK, T. Development of very-high-density low-enriched-uranium fuels. *Nuclear Engineering and Design 178*, 1 (1997), 119–126. cited By (since 1996)84.

[129] SOFU, T., KRAMER, J., AND CAHALAN, J. Sassys/sas4a-fpin2 liquid-metal reactor transient analysis code system for mechanical analysis of metallic fuel elements. *Nuclear Technology 113*, 3 (1996), 268–278. cited By (since 1996)6.

[130] SOHN, Y., AND KEISER, D. How fundamentals of phase equilibria and diffusion contribute to the rertr program. *Journal of Phase Equilibria and Diffusion 35*, 1 (2014), 1. cited By (since 1996)0.

[131] STRAIN, R., BOTTCHER, J., UKAI, S., AND ARII, Y. Fuel-sodium reaction product and its influence on breached mixed-oxide fuel pins. *Journal of Nuclear Materials 204*, C (1993), 252–260. cited By (since 1996)8.

[132] TILL, C., AND CHANG, Y. The integral fast reactor. *Advances in Nuclear Science and Technology 20* (1988). cited By (since 1996)8.

[133] TRACY, D., HENSLEE, S., DODDS, N., AND LONGUA, K. Improvements in the fabrication of metallic fuels. *Transactions of the American Nuclear Society 60* (1989), 314. cited By (since 1996)4.

[134] TRYBUS, C., SANECKI, J., AND HENSLEE, S. Casting of metallic fuel containing minor actinide additions. *Journal of Nuclear Materials 204*, C (1993), 50–55. cited By (since 1996)25.

[135] TSAI, H. Fuel/cladding compatibility in irradiated metallic fuel pins at elevated temperatures. *International Fast Reactor Safety Meeting II* (1990), 257. cited By (since 1996)1.

[136] TSAI, H. Behavior of low-burnup metallic fuels for the integral fast reactor at elevated temperatures in ex-reactor tests. *Conference on Fast Reactors and Related Fuel Cycles III 1* (1991), 18–21. cited By (since 1996)1.

[137] TSAI, H., NEIMARK, L., ASAGA, T., AND SHIKAKURA, S. Behavior of mixed-oxide fuel elements during an overpower transient. *Journal of Nuclear Materials 204*, C (1993), 217–227. cited By (since 1996)8.

[138] VAN LOO, F., VAN BEAK, J., BASTIN, C., AND METSELAAR, R. The role of thermodynamics and kinetics in multiphase ternary diffusion. *TMS (The Metallurgical Society) Paper Selection* (1984). cited By (since 1996)1.

[139] WACHS, D., KEISER, D., MEYER, M., BURKES, D., CLARK, C., MOORE, G., JUE, J.-F., TOTEV, T., HOFMAN, G., WIENCEK, T., KIM, Y., AND SNELGROVE, J. High density fuel development for research reactors. *Global 2007-Advanced Nuclear Fuel Cycles and Systems* (2007). cited By (since 1996)3.

[140] WADE, D., AND CHANG, Y. Integral fast reactor concept: Physics of operation and safety. *Nuclear Science and Engineering 100*, 4 (1988), 507–524. cited By (since 1996)46.

[141] WALTER, C., GOLDEN, G., AND OLSON, N. U-pu-zr metal alloy: A potential fuel for lmfbr's. *Argonne National Laboratory Report ANL-76-28* (1975). cited By (since 1996)1.

[142] WALTER, C., OLSON, N., AND HOFMAN, G. Ebr-ii driver-fuel qualification and performance. *Nucl Metall 1* (1973), 181–202. cited By (since 1996)2.

[143] WALTERS, L. Thirty years of fuels and materials information from ebr-ii. *Journal of Nuclear Materials 270*, 1 (1999), 39–48. cited By (since 1996)29.

[144] WALTERS, L. C., SEIDEL, B., AND KITTEL, J. Performance of metallic fuels and blankets in liquid-metal fast breeder reactors. *Nuclear Technology 65*, 2 (1984), 179–231. cited By (since 1996)30.

[145] WRIGHT, A., DUTT, D., AND HARRISON, L. *Proceedings of International Conference on Fast Reactor Safety IV 129* (1990). cited By (since 1996)1.

[146] WRIGHT, A., HAYES, S., BAUER, T., CHICHESTER, H., HOFMAN, G., KENNEDY, J., KIM, T., KIM, Y., MARIANI, R., POINTER, W., YACOUT, A., AND YUN, D. Development of advanced ultra-high burnup sfr metallic fuel concept - project overview. vol. 106, pp. 1102–1105. cited By (since 1996)2.

[147] YAO, B., PEREZ, E., KEISER JR., D., JUE, J.-F., CLARK, C., WOOLSTEN-HULME, N., AND SOHN, Y. Microstructure characterization of as-fabricated and 475 °c annealed u-7 wt. *Journal of Alloys and Compounds 509*, 39 (2011), 9487–9496. cited By (since 1996)12.

[148] YUN, D., YACOUT, A., AND WRIGHT, A. Thermomechanical modeling of u-pu-zr metallic fuel. *Transactions of the American Nuclear Society 106* (2012), 1205–1206. cited By (since 1996)1.